Analysis of retinal image quality for peripheral vision in humans and pigeons *(Columba livia)*

Yaiza García-Sánchez

School of Optometry and Vision Sciences

Cardiff University

A thesis submitted for the degree of

Doctor of Philosophy

June 2012

Abstract

Retinal image quality for peripheral as well as central visual field locations has been investigated in humans and an animal model *(Columba livia)* with wide-angle, panoramic vision because of its laterally oriented eyes. The goal was to determine whether the retinal image is maintained at a higher quality away from the fovea in pigeons as compared to humans. In this thesis, the HSWFS (Hartmann Shack Wavefront Sensor) has been implemented with the correspondent validation and application for measuring ocular aberrations in the human and avian eye.
Using a modified HSWFS, the refractive error and total amount of ocular aberrations were measured for 20 pigeons along the horizontal meridian and for another 8 pigeons in the vertical meridian at three positions along the horizontal meridian. The HOA(High order aberrations) of 10 humans were measured at peripheral locations ($\pm 35^\circ$) in the upper visual field and along the horizontal meridian. The anaesthetized animal's head position was controlled by a stereotaxic head holder capable of horizontal and vertical rotation. Measured eccentricities were($\pm 60^\circ$) from the fovea in the horizontal meridian and $+35^\circ$ and -25 $^\circ$ along each of the three vertical meridians.

In pigeons, the LOA (astigmatism) on the horizontal meridian increase slightly from the center towards the far periphery but are relatively constant for $\pm 20^\circ$ around the fovea, whereas defocus remains almost constant. Vertical meridian measurements are consistent with the previously reported myopia in the lower visual field. Compared with measurements in human subjects, the overall values of RMS are much lower in the pigeon at all corresponding eccentricities. Off-axis vision is generally dominated by defocus and astigmatism. In pigeons, however, defocus along the horizontal meridian does not change dramatically whereas, along the vertical meridian, the presence of a lower field myopia is confirmed. Astigmatism of the eye for increasing eccentricity (horizontally and vertically) is consistently lower then expected theoretically and when compared with humans. This demonstrates that the visual optics of the pigeon are more fully corrected for peripheral vision than in humans.

Acknowledgments

I would like to gratefully acknowledge everyone who helped me out during this difficult and long process. I am aware that I will forget many names, but I will try my best not to....

I would like to thank my supervisors for their patience and encouragement along the way. I would like to acknowledge Prof. Wolfgang Drexler for his financial support and advice and, in particular, for giving me this opportunity. There will be not enough words to thank Dr. Jonathan T Erichsen for having this idea and for working hard with me to make it real; I was very fortunate to have such a good supervisor throughout my PhD studies. I am also very grateful to Chris Dillingham for without his help and collaboration and wide expertise on birds, this job would have been impossible to accomplish. Finally, I would like to show my appreciation to Prof. Chris Dainty for his efforts and his valuable input on the final phases of this work, which greatly helped me produce the final version of this thesis.

My family was always available and ready to help. Without them, this would have been an impossible mission. So, thanks to my mum and dad, and special thanks to my little brother, Manu. They have been suffering through all my tantrums and mood swings, but they have always been supportive, cheering me up whenever it was needed, with kind words or even a bit of MATLAB coding.

On another plane of reality, all those years in Cardiff I had the support of many friends. Some of them were "suffering" with me at Cardiff University School of Optometry and Vision Sciences while dealing with their jobs in parallel. I would like to thank Sue Hobbs and Steve Morgan for their incredibly support during this long process. Thanks also to those who shared my office, including Claudia Hoffmann, Sara Rey, James Fergusson, Dr. Aneesh Alex and Vedran Kajic. I would like to thank the whole Biomedical Imaging Group at Cardiff for all the help they provided but especially to Dr. Cristiano Torti, who guided me and showed me some tips and tricks when I started. For being more than colleagues i.e. real friends, I would like to thank from other research groups Dr. Magdalena

Nowak, Dr. Tetyana Zayats, Dr. Miguel Jarrin and Dr. Kinga Handzel, for making this experience easier and funnier. Thanks to Dr. Alison Binns for always being ready to help, to listen and to smile even on the worst days....
Some international colleagues are also worthy of acknowledgement. All my gratitude to Dr. Maciej Nowakowski at the National University of Ireland (NUI) in Galway for providing me encouragement and support despite the distance and for his generosity in terms of time. To Dr. Linda Lundstrom at KTH (Royal Institute of Technology) Sweden, thanks for all the constructive discussions and sharing with me deep knowledge about peripheral aberrations.

My friends outside the School of Optometry and Vision Sciences made my life at Cardiff easy. I will never have enough words to thank Dr. Anabel Morte for being more than a friend, for being almost a sister, and for all those lunchtimes sharing PhD worries and life concerns. Thanks to all the people who made my Fridays better: Dr. Carmen Casaliggi, Dr. Veronica Gonzalez, Dr. Niek Buurma, Gabriele Banci, Giorgia Milani, Pili Larosa, Isabel Vazquez, Dr. Grazia Bezzu and Dr. Lino Carta, with a special mention to Dr. Maurizio Albano for his patience and encouragement. Thanks to Cristina Higuera for always being positive.

Thanks to all my students and thanks to the School for giving me the opportunity to demonstrate to them, I truly think that I learnt much more from them than they from me. It was a great experience. Special mention deserved by Diya Dassyne who became a friend for life, for always being there for me whenever I needed a smile or a hug.

I am such a lucky person, so rich in friends, that I would need a whole thesis to thank them. I would like to give special thanks to Sara Ortega for helping me out with the figures and with life in general for more than 15 years. Thanks to Dr. Lucia Santamaria for all the encouragement and for walking those steps before me, for being so honest and supportive and for her constructive criticism. A special mention is deserved by Belen Puerta but I have no words to explain what she means to me. Thanks to Alberto Gagliarducci for so many things, for being

always on the other side of the screen, for making me grow as a person during all these years. Thanks to Dr. Vincenzo Fusillo for making me believe in miracles, and giving me a reason to carry on despite all the troubles I encountered. Writing this thesis has been a long process, which I have carried out in three different countries while I was doing other things in parallel. So thanks to my friends who supported me while I was in Spain and also to my new friends and colleagues in Canada (in no particular order, Guillermo Santamaria, Maria del Mar Lopez, Irene Valenzuela, Ildiko Monus, Amor Rodriguez and Dr. Antonio Garcia y Beltran, Melissa Cotesta, Carole Panton, Wylie Tan, Michelle McFarlane, Angela Alonso, Dr. David Pajuelo and Dr. Jorge Mejias); and some other "Angeles de la Guarda" for their support encouragement and patience in enabling me to complete this thesis was much appreciated.

Last, but not least, I should not forget to thank all my subjects for giving me their time and the "use" of their eyes for the imaging sessions.

Yaiza García Sánchez
Spain, December 2011

A mis padres y a Manu.

Abbreviations

AL **A**xial **L**ength
CCD **C**oupled **C**harged **D**evice
D **D**iopters
GRIN **G**radient **I**ndex
He-Ne **H**elium **N**eon
HOA **H**igher **O**rder **A**berrations
HSWFS **H**artmann-**S**hack **W**ave**f**ront **S**ensor
λ Wavelength
LCA **L**ongitudinal **C**hromatic **A**berration
LRT **L**aser **R**ay **T**racing
LOA **L**ow **o**rder **A**berrations
MTF **M**oduation**T**ransfer **F**unction
μ microns
BS **B**eam-**S**plitter
PSF **P**oint-**S**pread **F**unction
RMS **R**oot **M**ean **S**quare
TCA **T**ransversal **C**hromatic **A**berration

Contents

List of Figures

List of Tables

Chapter 1

Introduction

The analysis of the retinal image quality of the human eye using aberrometry has been a popular topic in recent times, because provide useful information about the overall quality of the eye acting as an optical system. If more accurate information can be obtained, a better correction could be achieved.

The vision of humans and animals comprises very complicated phenomena and remains difficult to describe. During the last few decades, the study of both visual structures and perception, have become increasingly comprehensive. At present, the methods used are highly sophisticated and the accuracy of results achieved is constantly improving. The visual process involves mainly three steps: the first involves the eye, whereby light is focused onto the retina; the second step is phototransduction, which is accomplished by the retinal cells that turn the light into electrical and chemical signals; finally, once this signal is processed, it is sent to the brain. Of course, the most important organ involved is, the eye. In the course of this PhD, we have evaluated the quality of the eye's optics using as a parameter the amount of ocular aberrations and how they change with increasing eccentricities.

The human eye is optimized for central vision. In this position, the amount of aberrations under normal conditions reach its minimum. For a variety of physical reasons, the optics are better in this position. On the contrary, in many animals, peripheral optics must be used to perform a variety of presumably high acuity tasks. We focused on birds, specifically pigeons or chickens, because they are very dependent on vision and have remarkable visual capabilities. In addition, the eyes are often laterally placed, which is clearly related to the presence of a specialization in the temporal retina. In fact, these animals must look obliquely using the peripheral visual field, to see forward. There is frequently a second retinal specialization with high photoreceptor densities, implying that the optical

quality is also good.

The human eye has been extensively studied and from a very early time, attempts have been made to correct its optics when necessary, starting from the use of polished stones in ancient time, to compensate refractive errors and ultimately progressing the manufacture of spectacles and contact lenses. Since Helmholtz it has been well known that the eye is subject to aberrations other than defocus and astigmatism. The analysis and understanding of these High Order Aberrations (HOA) has been the subject of numerous studies [Liang et al. [1994], Liang and Williams [1997] and Porter et al. [2001]]. The assessment of aberrations at the clinical level has recently been revolutionized by the advent of refractive surgery, which has became a common practice in eye clinics Wang and Koch [2003].

Today, even more elaborated techniques are being developed and used, for example the design of customized ophthalmic lenses; contact lenses that have optimized compensation for certain types of higher aberrations is now a reality Smith et al. [2002]. But to achieve this level of correction, the study, and measurement of aberrations is absolutely necessary. So far, considerable attention has been dedicated to the study characterization and analysis of ocular aberrations for central vision, but in contrast the investigation of ocular aberrations for peripheral vision is a far less well explored topic. The first studies realized in this field were based on skiagrams that analyzed only the horizontal meridian of the human emmetropic eye Lotmar and Lotmar [1974]. More recent studies have explored the off-axis image quality by using double pass techniques Jennings et al. [1980], but again the majority of these initial studies was restricted to the horizontal visual field Atchison and Charman [2003] and Atchison and Scott [2007]. Lately, the Hartmann-Shack technique has been proved to be a valid technique for measuring peripheral refraction, among other aberrations Atchison [2003] and Sheenan et al. [2007], and very recently, a modified commercial aberrometer has been implemented for measuring ocular aberrations across the central 42 ° horizontal x 32 ° vertical visual field of five young emmetropic subjects Mathur et al. [2008].

The objective of the present study is to obtain a better understanding of the quality of peripheral vision in humans and animals. When the peripheral optics

of the eye are used, the quality of retinal images, in the case of human eyes, is significantly lower than along the visual axis Jennings and Charman [1997] and Navarro et al. [1998]. The measurement of aberrations in animals is not a new approach; the feasibility and the power of this technique has been shown in previous studiessuch as that of De la Cera et al. [2006b] where twelve eyes from old black C57BL/6 wild type mice were studied and the aberrations were measured using a custom-built Hartmann Shack system (using 680-nm illumination), or of Coletta et al. [2003] where an objective double-pass technique was used to measure the optical quality of the eyes of White Leghorn chickens for 21 eyes. The retinal quality was evaluated by means of the point spread function PSF for a wavelength of 543-nm. More studies have been performed with different species of birds. Harmening et al. [2007] measured the eyes of four adult American barn owls Tyto alba pratincola by means of the Tscherning Aberroscope with a 660 nm laser-diode illumination source.

During the planning stage for this project, the pigeon eye was chosen as a study subject, for several reasons. Most birds, including the pigeon, are highly visual animals with relatively large eyes that are easy to work with. The lateral positioning of the eyes in the head is another advantage for the exploration of peripheral vision. A previous study has shown that the pigeon eye is largely corrected in the periphery for lower order aberrations (LOA), i.e. defocus and astigmatism see Erichsen [1979], along the horizontal visual field. The presence of a lower field myopia, has been demonstrated in subsequent studies Hodos and Erichsen [1990] and Schaeffel et al. [1994], using retinoscopy in the former and infrared refractometer in the latter, but to our knowledge, no study has been performed using a Hartmann Shack aberrometer. Moreover, the extent of this correction for higher order aberrations and the underlying mechanisms involved are still unknown.

The aim of this thesis is to obtain a comprehensive knowledge of the extent of peripheral correction in the pigeon eye and its possible future application to improving correction of human vision and improve the design of artificial optical systems. In order to achieve this goal, we decided that the use of a Hartmann-Shack sensor was the best option for evaluating in the periphery the refractive state (i.e defocus and astigmatism) as well as the HOA. The investigations per-

formed in this thesis comprise a set of measurements in human eyes for later comparison with corresponding data from pigeon eyes, evaluating the off-axis ocular aberrations and peripheral refraction for a wide range of eccentric locations in both humans and pigeons.

The general structure of the thesis is as follows:

The **Chapter 2**, presents a brief description of the human and pigeon eye anatomy, focusing on their similarities and differences as well as the influence of the eye structure on the overall retinal quality.

Chapter 3, gives a brief historical review of aberrometry and refractive state assessment, and different techniques to measure ocular aberrations will be discussed and compared. After considering the mathematical formalism used to describe aberrations, a comprehensive description of the design and construction process of the instrument used in this study, i.e. a Hartmann-Shack aberrometer, will be provided.

Chapters 4 and **5** outline the studies carried out and the experimental results for the measurement of ocular aberrations central and peripheral in humans and pigeons, respectively.

Finally in **Chapter 6**, the findings of this project and the conclusions that can be drawn will be summarized and discussed.

Chapter 2

Human Eye and Pigeon Eye

2.1 The Human Eye Anatomy

2.1.1 General Ocular Anatomy

The receptor organ of the vertebrate visual system is the eye. Structurally, the eye is made up of three different layers or tunics: the fibrous tunic, the vascular tunic and the nervous tunic. The shape of the human eye itself is approximately spherical, and the axial length (AL) changes during early life. For a new born baby, the actual length is about 18 mm in diameter, but the eye keeps growing until it reaches about 24-25 mm in length for adults. Figure 2.1 illustrates the major parts of the eye in cross-section.

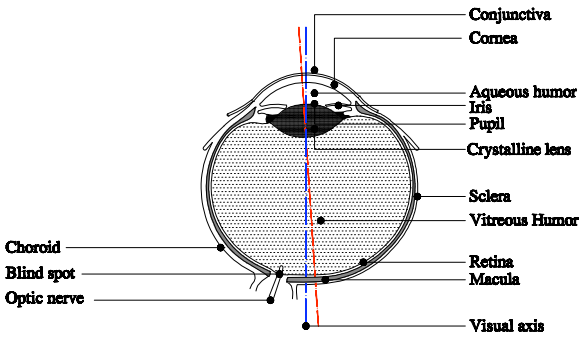

FIGURE 2.1 – Horizontal section of the Eye showing the main elements as well as axes (visual axis in red and central axis in blue)

The **fibrous tunic** is the most external layer of the eye and includes the sclera, the cornea and the limbus. It is made up of connective tissue, mainly

collagen, but its distribution changes depending on position. The collagen fibers comprising the cornea are arranged in a highly ordered way, which results in its required transparency.

The **vascular tunic** is the middle layer of the eye and consists of blood vessels, which provide the necessary oxygen to the other layers of the eye. The vascular tunic comprises the iris and ciliary body at the front of the eye and the choroid, which underlies the retina.

The **neural tunic** is the inner sensory layer of the eye and includes the retina, which contains two types of photoreceptor: the cones and the rods.

2.1.2 The Cornea

The cornea, the transparent cover or window of the eye that permits light to enter, is made up of collagen and belongs to the fibrous tunic to the eye. It provides the majority of the dioptric power of the eye, i.e. about two thirds or around 43 D . The human cornea is a non-vascularized organ that has a diameter of about 11.5 mm and a thickness of 0.5 mm - 0.6 mm in the center and 0.6 mm - 0.8 mm at the periphery. The radius of curvature of the anterior surface of the cornea is, on average, 7.8 mm, and its shape is approximately spherical in the center but flatter in the periphery, having an overall oval shape. The radius of the cornea is not homogeneous along all meridians, i.e. the cornea is a toric surface, and if the difference between the meridians is substantial, the subject will experience some astigmatism. The posterior surface of the cornea has a curvature radius of 6.8 mm; this surface provides, on average, a dioptric power of -5.88 D. The average refractive index of the corneal substance may be taken as 1.376, although every layer that comprises the cornea has its own specific refractive index. The adult cornea comprises five layers: epithelium, Bowman's membrane, stroma, Descemet's membrane and the endothelium, as depicted in Figure 2.2.

The epithelium is the most anterior layer of the cornea. Made up of five layers of cells, it is kept moist by the tear film. These cells grow rapidly and are easily regenerated. Bowman's membrane lies just beneath the epithelium. In this layer, the cells are very tightly packed, making it very difficult to penetrate, and

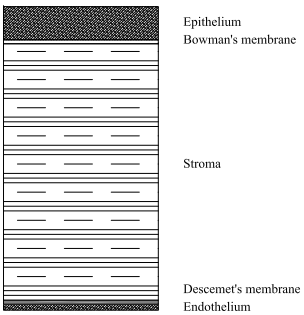

FIGURE 2.2 – Representation of the layered structure of the cornea

thus the deeper layers of the cornea are protected. The stroma is the thickest corneal layer and lies just underneath Bowman's membrane. The collagen fibrils that comprise this membrane run parallel to each other. This special orderly formation of the collagen fibrils provides the corneal transparency. Descemet's membrane lies between the stroma and endothelium and is formed by a single layer of cuboidal epithelial cells. The endothelium is just underneath Descemet's membrane and is only one cell layer thick; the shape of those cells is hexagonal. The endothelial cells pump water into the entire cornea to maintain the hydration level required to preserve the cornea's transparency. The first chamber of the eye is beneath the cornea and is called the **anterior chamber**, being filled with an aqueous solution, its consisting of 98% water Bennett and Rabbett [2007] The iris is an anatomical structure that lies between the cornea and aqueous humor and the crystalline lens. The central aperture of the iris is known as the pupil; which is circular under normal conditions. The pupil dilates and contracts as a reaction to luminance changes. Pupil size plays a very important role in the amount of ocular aberrations. Under normal conditions, the size of aberrations is higher when the pupil diameter increases because the amount of light entering the eye is greater.

Corneal Aberrations The corneal anterior surface is the interface between the eye and the air. Due to the large difference in refractive index at this interface, this surface is mainly responsible for the dioptric power of the eye, i.e. about 43 D. The cornea is mainly responsible for ocular aberrations (e.g. spherical aberration),

which are caused by both corneal surfaces. The amount of aberrations varies from one subject to another, especially in people. Since the anterior surface is more accessible, it is easier to perform simulations of the aberrations produced by that surface, as reported in the literature Navarro et al. [2006]. It has been shown that, in general, the amount of aberrations due to the first surface of the cornea is partially compensated for by the posterior surface of the cornea Arni et al. [2006]. For both corneal surfaces, a significant increase in aberrations with age was also found Artal et al. [2002].

We can summarize the influence of the cornea on the total amount of aberrations in the eye as follows:

- The spherical aberration of the posterior corneal surface starts with a negative value, taken from measurements of human adults, and increases to a positive value with age.
- The amount of monochromatic aberrations due to the cornea increases approximately linearly with age.
- The crystalline lens of the eye is able to partially compensate for corneal aberrations, but this compensation is not present in older subjects Artal et al. [2001].

These results have been reported in previous studies with the double-pass method, in combination with an aberroscope and a spatially resolved refractometer. Consequently, a one surface model is not sufficient to predict the spherical aberration of the cornea, and so additional measurements of the posterior surface of the cornea are important in order to more properly estimate the aberrations produced by this surface.

2.1.3 Tear Film

The first and most powerful optical surface of the eye is the tear film, which is liquid and covers the anterior part of the eye, cornea bulbar and palpebral conjunctiva. The tear film covers the entire curvature of the cornea, and the difference between its refractive index and that of air is the largest occurring in

the eye. We can describe the tear film as a three-layer structure consisting first of a lipid layer. Underneath lies the aqueous layer and the mucus layer, as shown in Figure 2.3. The approximate thickness of the tear film is around 9μm, varying after successive blinks.

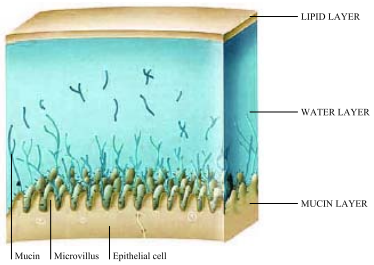

FIGURE 2.3 – Structure of the tear film (modified from http://www.nfburnetthodd.com/dryeye.html)

This structure serves several functions for the eye, including providing a smooth and more homogeneous optical surface. During blinking, the tear film spreads across the cornea, and the nutrition of the corneal surface is provided by this fluid by transferring the oxygen content in the film to the corneal surface. Previous studies Grupetta et al. [2005] have shown the importance of the tear film in the dynamics of ocular aberrations especially in the moment of its break-up. Another study Dubra et al. [2004] suggest that the tear topography dynamics under normal conditions does not play a significant role. Furthermore, eye movements affect aberrations, tear film evaporation and other external factors. Consequently, the aberrations introduced by the tear film are dynamic. The main contributions to tear film aberrations were observed to be from 4th order Zernike terms. The aberrations that have a vertical component are more important; this is due to the pressure made up from the opening and closing of the eyelids, which produces a vertical break up of the tear film.

2.1.4 The Crystalline Lens

The crystalline lens is located just behind the iris, and its position in the eye can be seen in Figure 2.4. The lens nucleus is made up of tightly packed fibers known

as laminae. The lens capsule, containing the lens, is held in place by the zonules that are connected to the ciliary body.

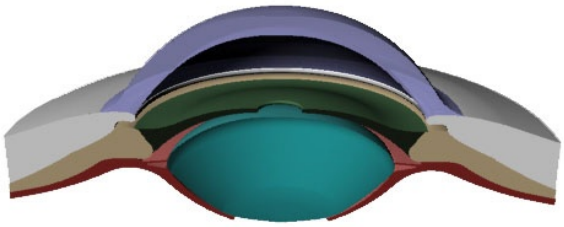

FIGURE 2.4 – Position of the crystalline lens in the eye.

The general shape of the lens can be described as biconvex with an average power of 14 D in the native, non-accommodative state.The thickness of the lens is about 3.6 mm, and the average diameter is about 9 mm. A cross sectional image is shown in Figure 2.5.

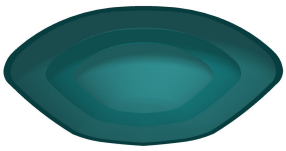

FIGURE 2.5 – Horizontal section of the Crystalline Lens.

It is well known that the crystalline lens is the main organ involved in the accommodation process, which is the mechanism that allows the eye to focus at different distances in the adult human. Contraction of the ciliary body produces the relaxation of tension on the zonules, resulting in an increase the lens curvature and this its dioptric power, allowing the eye to focus objects that are placed close to it. The opposite phenomena, i.e. relaxation of the ciliary body, produces a retraction of the zonules and thus a flattening of the lens and a reduction of its power, allowing in focus on more distant objects Glasser [2010]. During

the accommodative process, the contraction of the ciliary muscle will produce a change in the overall shape of the lens and a redistribution of the refractive index values that leads to a change in refractive power, this in turn allows the subject to bring into focus objects that are placed at a near distance. The outer part of the lens is called the capsule, which is a thin membrane that surrounds the lens and is made of collagen. Beneath the capsule can be found the lens epithelium, which regulates the homeostatic equilibrium of the lens. The lens nucleus is made of radially placed fibrils that keep growing throughout life by the formation of new layers in the exterior part. The refractive index of this structure is not uniform, resulting in a gradient index (GRIN) see Navarro et al. [2007]. An approximation of the mean refractive index of the lens is estimated to be 1.42, and its refractive power about 16 D.

Crystalline Lens Aberrations Previous studies have also shown that many aberrations can be present in the isolated crystalline lens. In this case Roorda and Glasser [2001], the measurements were taken using LRT (Laser Ray Tracing). Negative spherical aberration dominated, showing that the 4th order spherical aberration became more negative, and the 6th order spherical aberration progressed from negative to positive, during the accommodative process.

In vivo estimation of the crystalline lens aberrations is a complex process, because the lens is not as easily accessible as the cornea. However, some early studies assessed the aberrations of the crystalline lens in different ways Hage el and Berny [1973]. Determined the contribution of the lens to the total spherical aberration of the eye; first, photographic keratometry was used to measure the cornea and then, for the same subject, the spherical aberration of the eye was determined by the Foucault knife-edge test. The aberrations of the lens can also be estimated using psychophysical methods Tomlinson et al. [1993].

More recent approaches measured the high order aberrations (HOA) using a corneal topography system and a Hartmann-Shack wavefront sensor; wavefront aberrations of the anterior corneal surface and of the whole eye can be measured independently. From those values, the wave-front aberrations of the internal optical structure (which includes the posterior corneal surface as well as the position and shape of the lens) can be derived for the lens Wang and Santaella [2005].

Using this approach, the combination of the aberrations of the crystalline lens and those of the cornea was found to be either a compensatory or an additive process Artal and Guirao [1998] and Artal et al. [2001]. If the RMS of the wave-front aberration for the whole eye is always less than the RMS values for either the anterior cornea or the internal optics, the process is called compensatory. On the contrary, if the RMS value of the whole eye is higher then the RMS values of the cornea and the lens separately, the process is additive. But subsequent work Millodot and Sivak [1979] showed that the aberration of the lens does not systematically neutralize that of the cornea or vice-versa.

2.1.5 The Retina

The retina is a multi-layered sensory tissue that lies the back of the eye. It contains millions of photoreceptors that absorb light rays and convert them into electrical impulses. Ultimately arriving at the retinal ganglion cells, impulses travel along their axons, which comprise of the optic nerve, to the brain where they are processed and turned into the perception of images. In Figure 2.6, we can see the general structure of the retina.

The vertebrate retina has the following layers, from the outer to the inner layer :

- **PE** Pigment Epithelium
- **PR** Photoreceptor layer : rods/cones
- **ONL** Outer nuclear layer : cell bodies of rods and cones
- **OPL** Outer plexiform layer : projections of rods and cones ending in the rod spherule and cone pedicle, respectively. These make synapses with dendrites of bipolar cells in the macular region.
- **INL** Inner nuclear layer : contains the nuclei and surrounding cell bodies of the bipolar cells.
- **IPL** Inner plexiform layer : contains the synapse between the bipolar cell axons and the dendrites of the ganglion and amacrine cells.

- **GCL** Ganglion cell layer : layer that contains the nuclei of ganglion cells, the axons of which become the optic nerve.
- **ON** Optic nerve

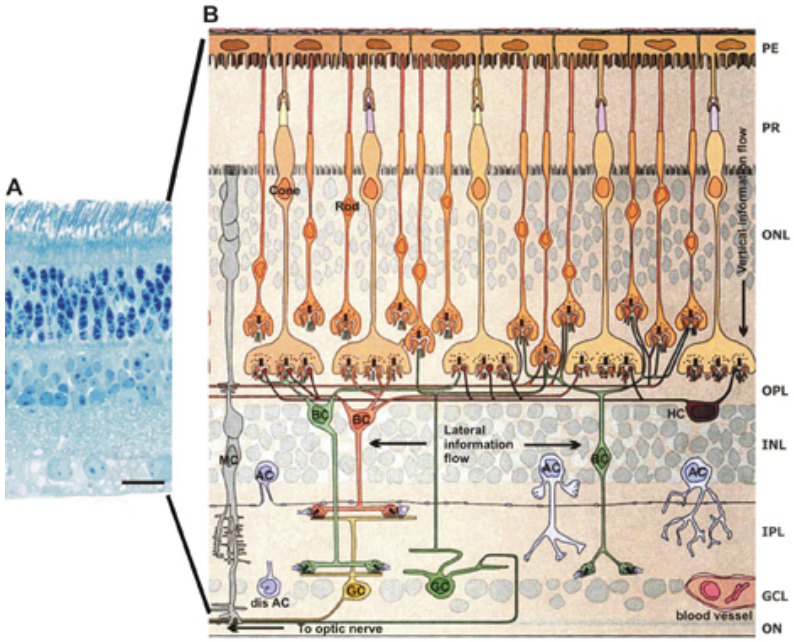

FIGURE 2.6 – Structural arrangement of the retina. (left) Methylene blue stained section (right) bar ($20\mu m$). Schematic diagram of retinal connections (Adapted from Rodieck 1998)

In the non-accommodative state of an emmetropic eye the ideal position of the retina corresponds to the focal point of the cornea and lens. If the focused image is behind the retina, the eye is hyperopic, and if in front of the retina, it will be myopic.

In the nasal part of the retina is the optic nerve, a circular to oval white area on a fundus photograph measuring about 2 x 1.5 mm across. From the center of the optic nerve radiate major retinal blood vessels as well as nerve fibers. The central part of the retina is defined by the position of the macula, where the density of photoreceptors is the highest, as shown in Figure 2.7. Approximately 17 degrees (4.5-5 mm) from the optic disc, a blood vessel-free spot, the fovea, can be seen in

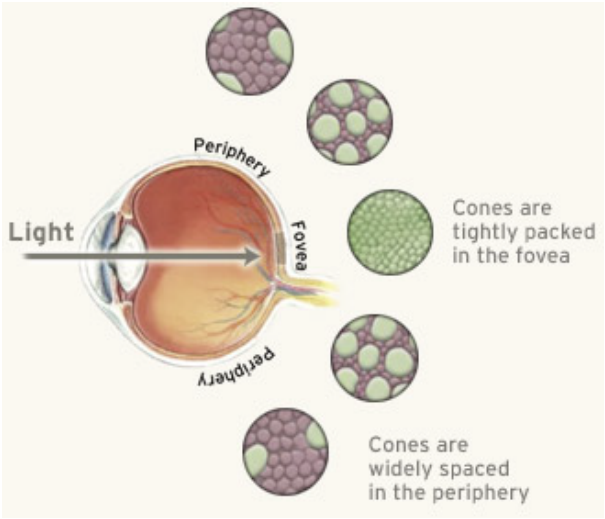

FIGURE 2.7 – Representation of the cone density distribution across the retina adapted from http://www.webexhibits.org.

the center of the macula. There are two types of photoreceptors in the retina: rods and cones. The human retina contains approximately 6 million cones, which are located primarily in the macula, the portion of the retina responsible for central vision. They are most densely packed within the fovea, as described in Osterberg [1935] and depicted in Figure 2.9, i.e. the very center portion of the macula. Thus, the central retina close to the fovea is considerably thicker than peripheral retina. Cones function best in bright light and allow us to discriminate color. Central retina is cone-dominated whereas peripheral retina is rod-dominated.

There are approximately 125 million rods. They are spread throughout the peripheral retina, functioning best in dim lighting and being responsible for peripheral and night vision. The relative distribution of cones and rods in the retina is shown in Figure 2.8.

The thickness of the outer nuclear layer (ONL) is approximately the same for central and peripheral retina and is composed of the cell bodies of the rods and cones. However, in the periphery, the rod cell bodies outnumber the cone cell bodies while the reverse is true for central retina. In the central retina, the cones have oblique axons displacing their cell bodies from their synaptic pedicles in the

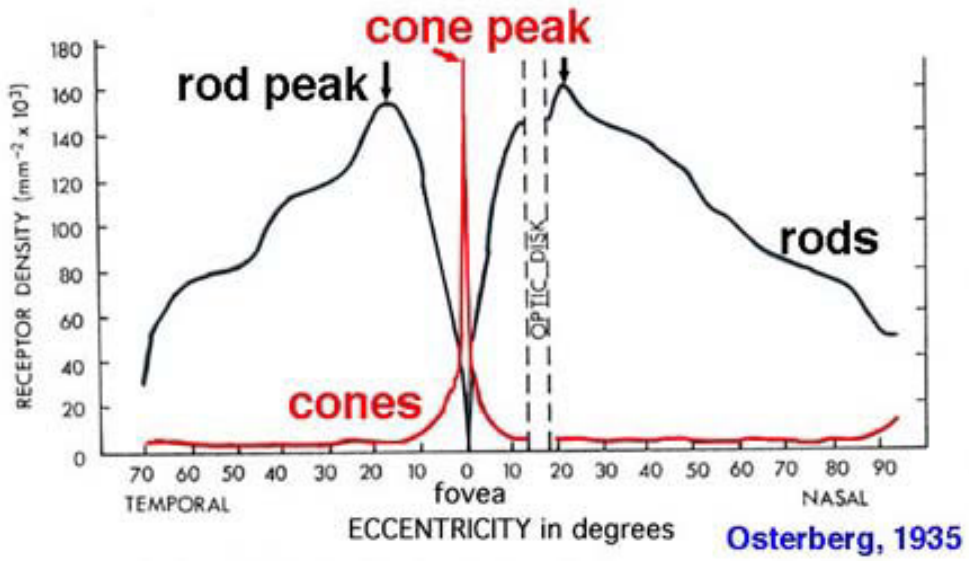

FIGURE 2.8 – Relative distribution of rods and cones in the retina depending on eccentricity

outer plexiform layer (OPL).

The inner nuclear layer (INL) is thicker in the central area of the retina as compared to the peripheral retina, due to a greater density of cone-connecting second-order neurons (cone bipolar cells). Horizontal cells are also more closely spaced, and there are numerous amacrine cells concerned with the cone pathways. The cone-connected circuits of neurons are less convergent than those in rod-connected pathways. A remarkable difference between central and peripheral retina can be seen in the relative thicknesses of the inner plexiform layer (IPL), ganglion cell layer (GCL) and nerve fiber layer (NFL). This is again due to the greater numbers and increased packing density of the ganglion cells needed for the cone pathways in the cone-dominant foveal retina as compared to the rod-dominant peripheral retina. The greater number of ganglion cells means more synaptic interaction in a thicker IPL and greater numbers of ganglion cell axons coursing to the optic nerve in the nerve fiber layer.A general overview is given in Figure 2.9.

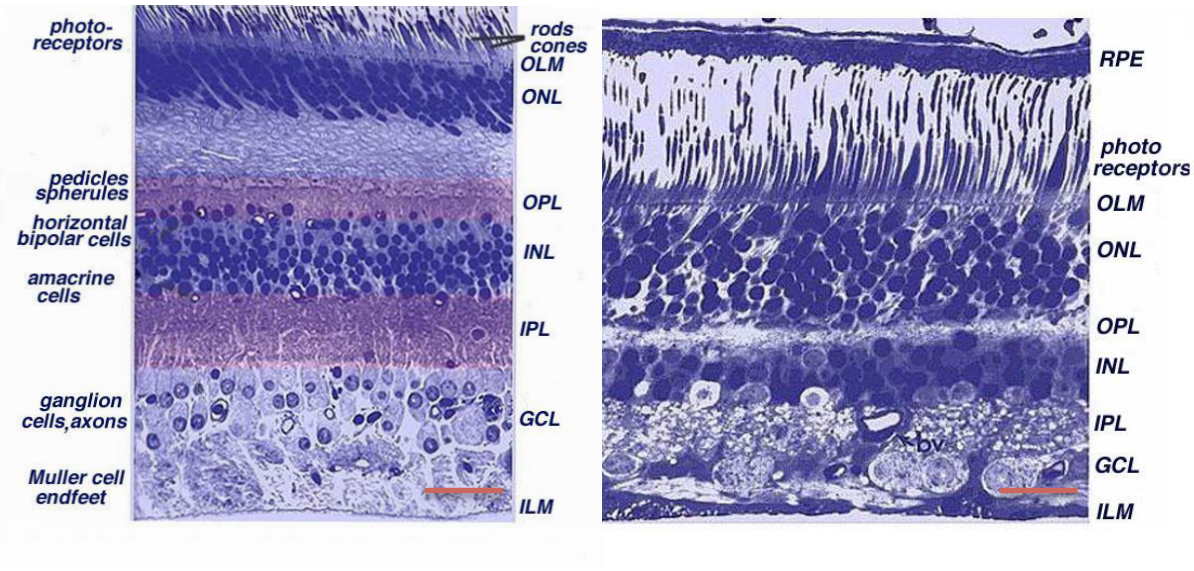

FIGURE 2.9 – Stained section (Richardson's methylene blue/azure II stain mixture, 40X objective) of the central retina(left) and peripheral retina(right) bar ($20\mu m$) (adapted from http://hc.les.dmu.ac.uk/mirrors/webvision/sretina.html)

2.1.6 The Fovea and Optic Disk

In the retina, we can distinguish anatomically and functionally two differentiated regions:

- **The fovea** From an anatomical point of view, the fovea has the highest density of cones. Therefore, normally visual acuity reaches its highest value in this region. In addition, we can also define the fovea and the parafoveal region from an optical point of view as the region of the retina where aberrations do not change significantly, thus being defined as an *isoaplanatic patch*.

- **The optic disk** This disk is located on the nasal side of the visual field whose center is the fovea. In humans is about 3 to 4 mm from the fovea. Anatomically the disk is the place where the axons from the ganglion cells exit to form the optic nerve; since no photoreceptors are present in this area, it is known as the blind spot.

2.1.7 Axis of the Eye

As said before, the eye is not a rotationally symmetric entity as an optical system. Therefore, a general axis should properly be defined by measuring the ocular aberrations along it. There is no common axis to all the surfaces present in the eye, but the axis used in this study is called *the line of sight* and is the line from the point of interest in object space to the center of the entrance pupil of the eye and continuing from the center of the exit pupil to the retinal point of fixation (generally the foveola). Another common axis used in vision sciences is the *optical axis* of the eye i.e. the line that joins the center of curvature of the anterior surface of the cornea and the posterior surface of the crystalline lens.

2.1.8 Refractive Errors

A refractive error occurs when the rays of light are not focused properly on to the retina. The resulting focal plane might either be in front of or behind the retina; the spherical refractive errors are then called **myopia** and **hyperopia**,

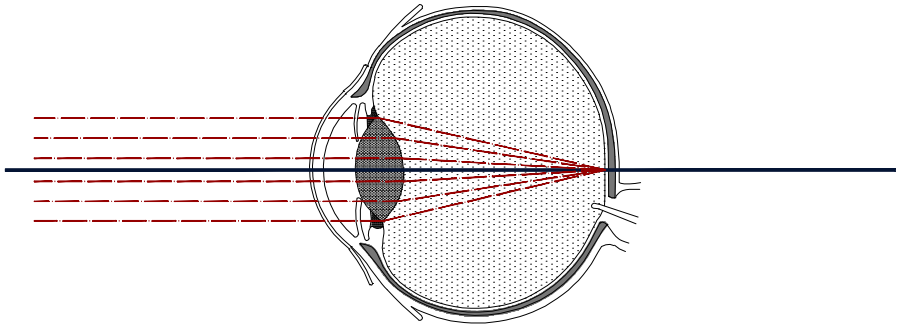

FIGURE 2.10 – Schematic representation of an emmetropic Eye.

respectively. Any cylindrical refractive error is called **astigmatism**.
The ideal, normal condition of the eye is called **emmetropia**, when the collimated rays that enter the eye in a relaxed state of the crystalline lens, i.e. without accommodation, are correctly focused onto the retina. In this case, no refractive correction is needed. An emmetropic eye is shown in Figure 2.10.

Myopia, often called short-sightedness, occurs when the collimated rays entering the eye are focused in front of the retina. As a result, the image is blurred on the retina, since the light is refracted more than necessary. The total dioptric power of the eye is higher than necessary to focus on the retina for a given axial eye length, as shown in Figure 2.11.

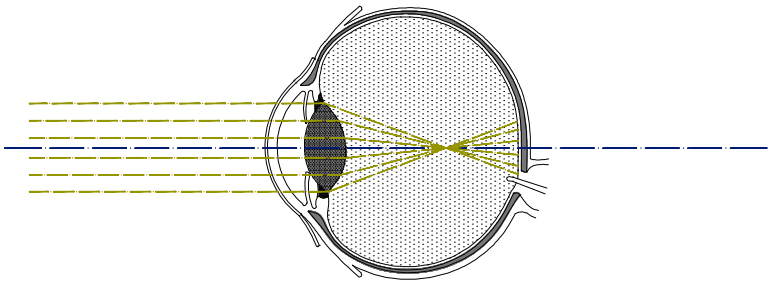

FIGURE 2.11 – Schematic representation of a myopic Eye.

Myopia may be due to different factors: either the excessive curvature of the cornea or axial eye length and can be compensated with (negative) glasses or contact lenses.

Hyperopia, also known as long-sightedness, occurs when the light that enters the eye is insufficiently refracted by the cornea and the lens relative to eye length. Hence, the focal point of this eye is behind the retina, and the image is also blurred for this refractive error. Most often, this condition occurs when the eye is either too short or the lens is not curved (i.e. powerful) enough. Hyperopia can be compensated with (positive) glasses of contact lenses. An hyperopic eye is illustrated in Figure 2.12.

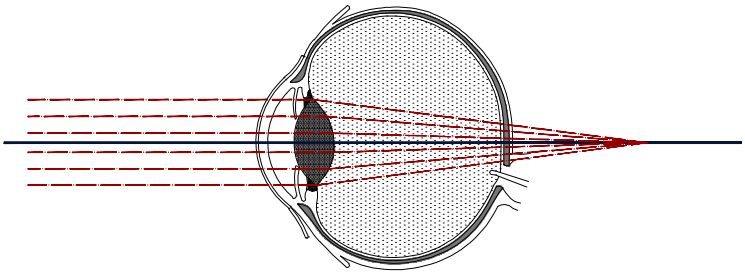

FIGURE 2.12 – Schematic representation of a hyperopic Eye.

Astigmatism occurs, when the cornea or the crystalline lens does not have a single radius of curvature. As a consequence, the light entering the eye is not focused symmetrically because the surfaces are not identically curved in all meridians, and consequently there are different focal planes and two different focal lines. Astigmatism can be corrected with glasses, using toric lenses.

2.2 The Pigeon Eye Anatomy

Pigeons are highly visual but they appear to possess a very specialized retina with adaptations for peripheral viewing. As a result, they are a suitable animal model for the study of visual optics. The eyes of pigeons are laterally positioned in the head, providing a nearly panoramic view of the world. Most birds also have a

secondary specialization of the temporal retina. Retinoscopy studies indicate that the pigeon eye is largely corrected for off-axis aberrations, but the extent of this correction and whether it includes HOA or how it is achieved are all unknown.

2.2.1 General Pigeon Ocular Anatomy

Similar to humans, vision is the primary sense for birds. Indeed, some species (e.g. eagles) have higher visual acuity. As vertebrates, birds have eyes that are structurally very similar to those of people (see figures 2.13 and Marshall et al. [1973]), and thus only the relevant differences will be discussed here.
The globe is large compared to body size, with a posterior segment disproportionately larger than the anterior segment comprising beak, jaw and orbit.

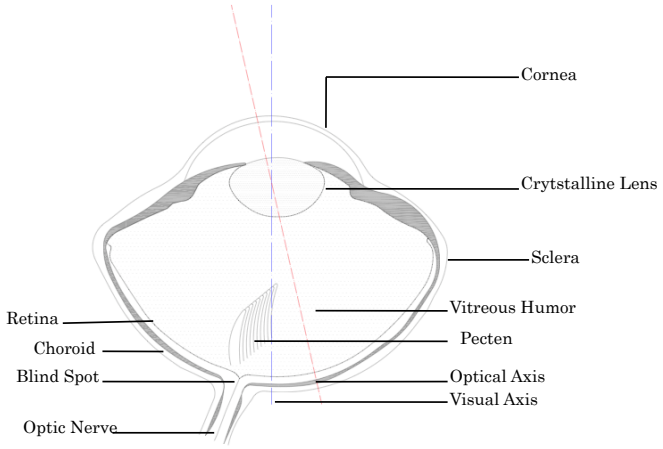

FIGURE 2.13 – Schematic representation of a horizontal section of the pigeon eye, the main elements as well as visual axes (visual axis in red and central axis in blue)

That the eye in the pigeon is very big compared to its body this fact has been demonstrated by several studies such as that of Hall and Ross [2006], which analyzed its allometry (i.e. the relative size of the eye in respect of the body). For very small body sizes (such as pigeon) eye size appears to be positively allometric, being consistent with defining the pigeon as a diurnal bird, (i.e. active during the day in a photopic, or light-rich, environment). The relative size of shapes that are maximized for visual acuity, with larger axial lengths relative to corneal diameters as shown in Russel [2004].

2.2.2 Pigeon schematic eye

In Figure 2.14 the schematic eye of the pigeon derived from 9 eyes presented in Marshall et al. [1973] is depicted. Being P and P' the anterior and posterior planes, N and N' the nodal points and F and F the foci. The curvature radii are presented in millimeters. According to these study the total power of the pigeon eye is 120D. The effective f-number is given by the distance from the posterior nodal point to the retina divided by the pupillary diameter, in this study the pupil diameter was calculated for a luminance of $2000cd/m2$ corresponding to overcast sky, the f number is of about 4.

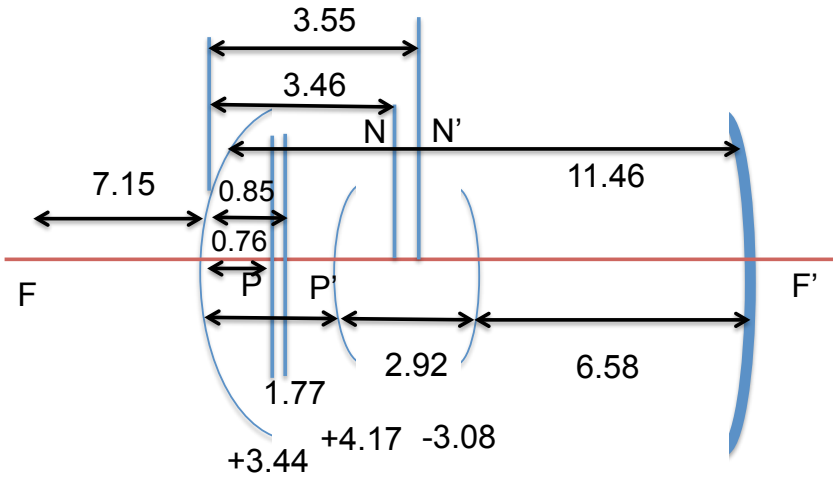

FIGURE 2.14 – The schematic eye of the pigeon, Adapted from Marshall et al. [1973]

2.2.3 Cornea and crystalline lens

Basically, the morphology of birds eyes, as well as their physiology is similar to that of mammals see Bayon et al., as illustrated in Figure 2.15.

Since cornea, lens and sclera of the human and pigeon eye, like those in most vertebrates, are very similar structurally and anatomically, a more comprehensive explanation of the anatomy of these structures of the pigeon eye is not necessary. Despite this fact, certain peculiarities that do exist must be considered.

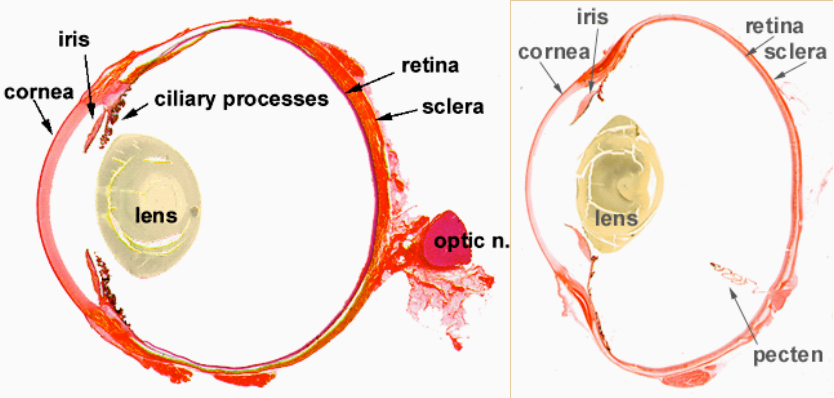

FIGURE 2.15 – Comparison between the shapes of the mammalian eye and avian eye, Adapted from Husband and Shimizu [2001])

2.2.4 Crystalline lens and accommodation

The lens is soft and almost spherical with a flat anterior surface in diurnal species, including pigeons. An annular pad lies under the lens capsule in the equatorial region and can be separated from the center of the lens during cataract surgery.

The mechanism of accommodation in the pigeon is far more sophisticated than in mammals. Firstly the power of the lens can be increased by contraction of the mid-striate ciliary muscles (Brucke and Crampton's muscles) which compress the annular cushion Williams [1994]). Lenticular changes in pigeon eyes are also due to a contraction of the iris muscle, Glasser and Howland [1997] and Ostrin et al. [2011] . The ciliary processes are attached to the equatorial lens capsule. Cramptons muscle has connections with the peripheral cornea, being able to produce changes in the corneal curvature when it contracts. Indeed natural accommodation has been shown to involve changes in the corneal radius of curvature, thus indicating that the cornea plays an important role. In the adult pigeon, the cornea is indeed responsible for the largest part of natural accommodation (up to approx. 9 D) Schaeffel and Howland [1987].

The iris muscles are mainly striated, with smooth muscles appearing only in smaller proportion. This fact allows a voluntary contraction of the pupil. The striated circumferential muscle seems to be the primary pupillary sphincter in all avian species. The circular pupil responds rapidly to accommodation and emotional state, as seen for instance in stress during handling. There is a direct

pupillary reex, but no consensual one, due to the complete decussation of the optical nerve axons. As in people, small degree of anisocoria can be normal Kern [2002].

2.2.5 The Retina

The anatomy of the pigeon retina is very interesting, since it is the part of the eye that is most different from the human eye. More importantly, for the purpose of this project, there is a higher degree of specialization in the avian retina. In contrast to most mammals, which do not have a fovea, most birds have a well developed central fovea as well as a secondary macula and/or fovea in the temporal part of the retina that allows them to posses a higher visual acuity in their frontal peripheral vision. More detailed information about the pigeon retina is provided by Nalbach et al. [1990].

In Figure 2.16, we can see a comparison of the foveal region for the human retina and avian retina, in this case the Artic Term (adaped from Husband and Shimizu [2001]). We can clearly distinguish the shape of both foveas being an apparently shallow-bowl shaped indentation in the case of humans and a much deeper convex depression in the bird.

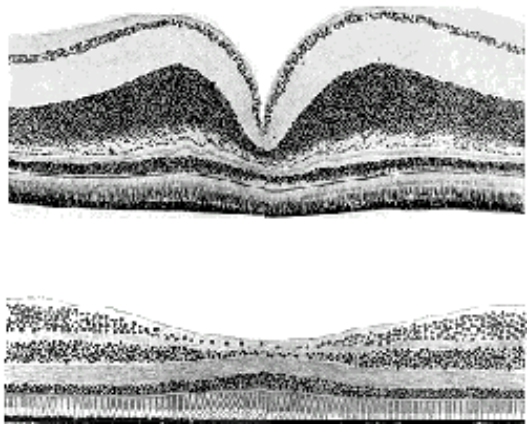

FIGURE 2.16 – Comparison between Human retina (bottom) and Avian retina (Artic term) retina(top).

Many birds have a horizontal streak or "central area"across the retina, with higher concentrations of sensory cells, usually associated with a fovea (area of highest concentration of sensory cells) at each end. Photoreceptor (cone) densities in the foveae may be as high as 65,000 per square millimeter in some diurnal birds of prey (e.g., American Kestrel) Sturkie [2000]. In humans, by comparison, the density of cones in the fovea is about 38,000 per square millimeter Curcio et al. [1990]. It also important to notice that the pigeon suffers from of an age related degeneration and a visual acuity loss related to the photoreceptor losses Hodos et al. [1991].

A representation of the retina of the pigeon is shown in figure 2.17. Here, the fovea can be visualized in a flat-mounted retina and its location referenced to the pecten tip, which of each eye in turn can be located in the visual field by perimetry. For the pigeon, the fovea is situated about 78° laterally away from the beak.

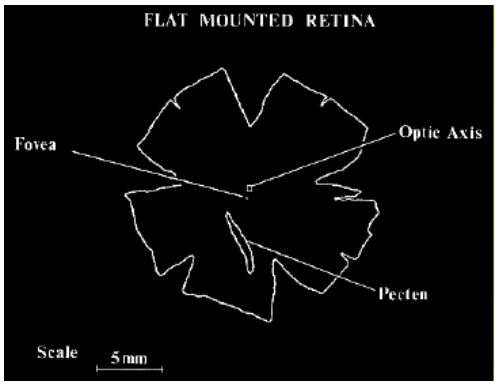

FIGURE 2.17 – Representation of the flat mounted retina for the pigeon

The avian retina contains as well two kinds of photoreceptors, rods and cones, similar to those of primates It also possesses (along with reptiles, many fish, and amphibians) photoreceptors known as double cones. The double cone consists of a principal cone (similar in structure to a normal single cone) and an accessory cone which curves around the inner segment of the principal cone

The principal and accessory segments of the double cone may contain different visual pigments. The interaction of signals from cones with different pigment types is crucial to color vision. The electrical signals generated by the double

cones in response to different wavelengths of light indicate that each member of the pair has strong interactions with the other.

The single cones, as well as one or both segments of double cones, may also contain an oil droplet. Oil droplets are a common feature of the cones in many vertebrate retinas, but are rarely found in rods. These drops consist of lipids in which carotenoid pigments are dissolved; they can appear transparent or clear, pale yellow, green, orange, or red.

Some authors have reported up to five different kinds of droplets with relative sensitivities of bands comprising from 600 and 610, 560 and 570, 470 and 514, 470 and 476 and below 430 μm, see Bowmaker [1977]. Most cones have a specialized, colored oil droplet interposed between the inner and outer segment that acts as a cut off filter to further refine the bird color vision. In the pigeon, the differential distribution of these oil droplets produces a yellow cast to most of the retina, but the superior temporal retina (i.e. the "red area") is rich in red droplets see Figure 2.18.

In the posterior dorsal part of the pigeon retina, rely the red field, about 80 per cent of the oil-droplets are red or orange as opposed to 25 per cent in the remaining part of the retina, the so-called yellow field. Therefore the red and the yellow fields are characterized by different ratios of oil-droplet/cone-pigment combinations. On the basis of these anatomical differences, the red and the yellow fields can be expected to have different photopic spectral sensitivities. It has been shown by Wortel et al. [1984] that, between 450 and 550 nm, the relative spectral sensitivity of the yellow field turned out to be higher than that of the red field. These results are in agreement with spectral sensitivity data, obtained by behavioral threshold procedures.

Ultraviolet reflectance could be used as a cue in discriminating foods (e.g. plants, seeds, berries) or other natural objects. Sensitivity to UV may also play a role in aerial navigation as an adaptation to the coloration of an unclouded sky.

The avian retina is not vascularized and the blood supply to the inner layers of the retina is dependent on diffusion from the **pecten**, a highly vascularized structure that protrudes into the vitreous this structure belongs to the choroidal tunic and is a non-sensory, pigmented structure lies over the point where the optic nerve enters the eyeball see Walls [1942]. Wolburg et al. [1999] provide a

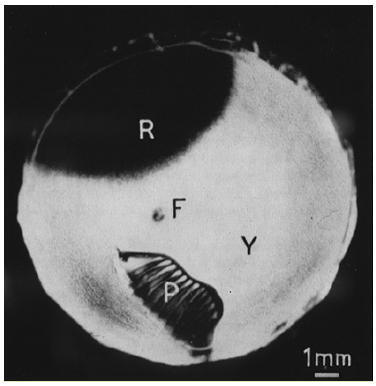

FIGURE 2.18 – Fundus of the pigeon eye illustrating the location of the pecten and the yellow (Y) and the red(R)field.

comprehensive overview of the pecten (in the case of chicken(*Gallus Domesticus*) and finds that the pecten oculi is a convolute of blood vessels in the vitreous body of the avian eye. This structure has been well known for more than a century, but its functions are still a matter of controversy. Most researchers believe that the function of this structure is to nourish the retina in the same way as as arteries and veins do in mammals, but via diffusion in the vitreous, since the avian retina is not vascularized. The location of the pecten in the pigeon could be the equivalent of the optic disk or blind spot in the mammalian eye.

2.2.6 Colour vision

Birds appear to have excellent color vision, which may be based on as many as four or five different photopigments, depending on species. This contrasts with the three cone pigments in primates. Evidence for tetra or pentachromatic vision in birds versus the trichromacy present in primates comes from analysis of the chemical properties of visual pigments and behavioral discriminations. Pigeons possess a rod photopigment (rhodopsin) with a maxima of $500\mu m$, and iodopsin and related cone pigments with maximum in absorption at about 413, 467, 514, and $567\mu m$ Blough [1957]. The scotopic function is fitted closely by aphakic human data. The photopic function shows inflections that may be related to similar inflections in corresponding human curves. The functions are

quite similar to those found in electrophysiological studies of the pigeon eye. They also correspond rather well to the absorption spectra of chicken rhodopsin and iodopsin.

In the study of Chen et al. [1984] spectral sensitivity was measured for different kinds of birds, these measurements demonstrated that the ultraviolet sensitivity of birds and seen in behavioral experiments has a biological foundation, and they provided further evidence that many vertebrates share with insects vision in the near-ultraviolet, this affirmation is also applicable to pigeons, mentioned in Goldsmith et al. [1984].

2.2.7 Placement of the eyes

In mammals, species with more frontally oriented orbits have broader binocular visual fields and relatively larger visual processing areas in the brain. This dependency was investigated in birds by Iwaniuk et al. [2008] who found that orbit orientation has a direct effect on the size of visual fields. For the specific case of pigeon (i.e. Columba Livia) was found to an orbital convergence of 49,6° and a correspondent binocular visual field of 22°. The morphometric points used are illustrated in the Figure 2.19, it is worth mentioning that orbit orientation is not the only determinant of the binocular visual field; eye movements can also alter the conjuration of the binocular visual field.

2.3 Central vision vs. Peripheral Vision

2.3.1 Human Visual Field

For a given eye position, **visual field** is best described as the space that contains all points that produce a stimulus in the eye (i.e. can be seen). In perceptual terms, the normal human visual field extends to approximately 60° nasally (toward the nose, or inward) in each eye, to 100° temporally (away from the nose, or outwards), and approximately 60 degrees above and 75° below the horizontal meridian. The macula corresponds to the central 13° of the visual field and the fovea to the central 3° .

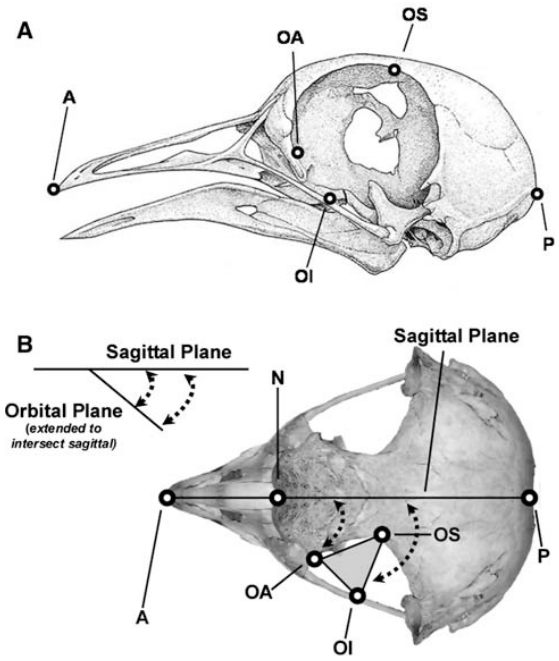

FIGURE 2.19 – Morphometric points used to define orbital and sagittal planes. The sagittal plane is defined by points A, N,and P. The orbital plane is defined by OS, OI, OA, the orbital convergence is therefore defined as the angle formed by the intersection of those two planes (adapted from Iwaniuk et al. [2008])

The configuration of the human visual field is typical for a predatory animal: the positioning of the orbits in the anterior part of the face and their axes are separated by approximately 45°. This configuration allows us to have a large binocular field. The extent of the monocular and binocular visual fields are shown in figure 2.20. To better understand the structure of the visual field, we can divide it into three parts:

- **Foveal vision** occupies an area about 3° wide at the center of attention. Whatever point we look at directly with attention is within the foveal field.
- **Parafoveal vision** occupies an area of about 20° on all sides of the foveal field. The parafoveal field provides the context for our focused attention, and typically frames in moderate detail the point we are looking, e.g. at the book we read, a person, a TV screen, etc.
- **Peripheral vision** is all of the remaining visual field, which in most people extends to 80° on either side of the center of attention (vision is limited above and below, because our eyes are set far behind our eyebrows and cheeks). This part of the visual field usually defines the overall environment, often in only very sketchy detail.

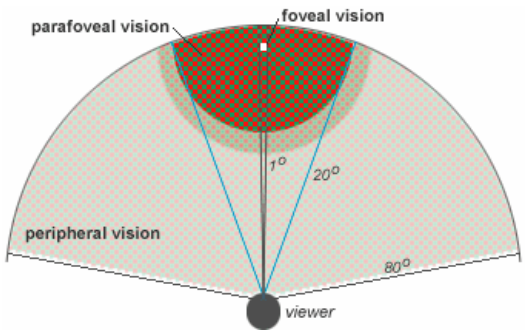

FIGURE 2.20 – Representation of the human visual field.

The limits of the monocular visual field are in the vertical meridian, the margins of the orbit, the nose in the nasal part and the projections of the retina on the ora serrata for the temporal side. The binocular visual field, occurring when both eyes are used, provides a wider total field of view than a single eye and

FIGURE 2.21 – Photograph of the positioning if the pigeon eyes.

also results in binocular summation by the brain's visual system, which enhances the ability to detect faint objects. Binocular vision is a requirement for stereopsis, produced from the different positioning and hence view of the two eyes, which enables depth perception, via the central processing of disparity information.

2.3.2 Pigeon Visual Field

The pigeon monocular visual field, as a result of evolutionary pressures, is much larger than in humans. Instead of having the eyes placed frontally, pigeons have their eyes laterally placed at an angle of about 80° from the beak, which provides a nearly panoramic view as shown in Figure 2.21.

This configuration provides them with a large visual field that comprises three parts, as shown in Figure 2.22. It is possible to differentiate only a small binocular field, where the monocular fields are overlapping. This binocular field of the pigeon can be seen in more detail in Figure 2.23. Binocular acuity in pigeons has been measured by means of the MTF Nye [1968] the peak sensitivity for the pigeon was found to lie at a spatial frequency of 0.07 cycles/min arc, whereas the corresponding peak sensitivity for the human eye lies in the region of 0.1 cycles/min arc. The difference between these maxima could arise from several sources: differences in retinal organization, size of receptive fields or the density

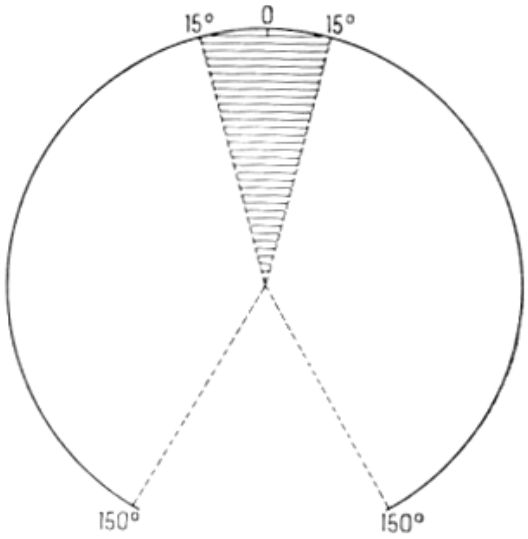

FIGURE 2.22 – Representation of the limits of the pigeon visual field.

of retinal receptors.

The binocular field for the pigeon (i.e. Columba livia) has been measured to have a maximum width of 27° and extends vertically by 130° (90° above the bill, 40° below it). Both the bill and cere intrude into the binocular field. Maximum optical binocularity also occurs approximately 20° above the bill. The plane containing the optic axes of each eye coincides with the bill Martin and Young [1983]. The size of the binocular field for the pigeon does not appear to be sufficient for the presence of stereopsis or 3D perception, but it was demonstrated that despite the small size of the binocular field of the pigeon, they do have depth perception McFadden [1987]. In contrast, the combined monocular fields are very extensive, providing the bird with a panoramic view of the world, which is useful for flying, orientation, and the early detection of predators (see Figure 2.23).

In conclusion, we can affirm that the frontal vision of pigeons involves the use of oblique optics. As will be mentioned in the next chapter for the human eye and many man-made optical systems the use of oblique optics normally implies a significant degradation in the quality of the final retinal image. An analysis of a range of studies of pigeon visual behavior indicates that distant objects tend to be viewed laterally but closer objects are viewed frontally Hahmann and Gunturkun [1993], Uhlrich et al. [1982], Hodos et al. [1976], as shown in Figure 2.24.

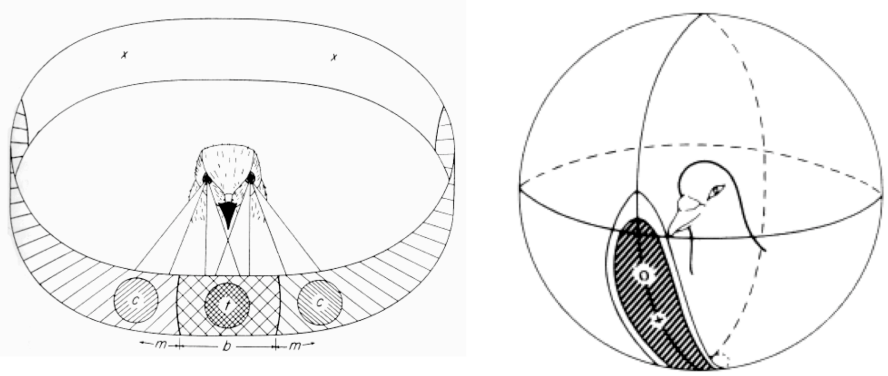

FIGURE 2.23 – Pigeon Visual field divided into monocular fields (left).Representation of the binocular visual field for the pigeon made of overlapping of monocular fields(right)

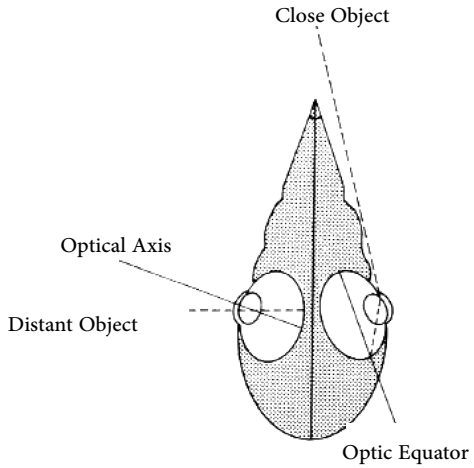

FIGURE 2.24 – Representation of the pigeon visual behavior.

This behavioral observation resulted in a hypothesis known as the Catania hypothesis, according to which the pigeon possess a myopic frontal visual field, whereas the lateral visual field is hyperopic, see Figure 2.25.

But this hypothesis is not consistent with the fact that pigeons use their frontal field not only for pecking but also for flying. In view of the obvious need for a more distant view of the world when flying, it is hard to accept that their entire frontal visual field is myopic.

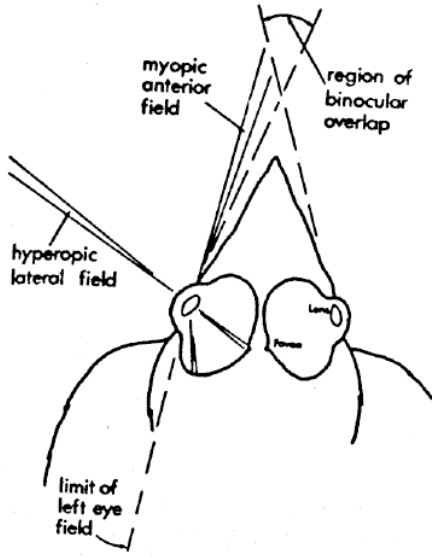

FIGURE 2.25 – Representation of the Catania hypothesis.

To investigate further the refractive state of the pigeon eye in a different part of the visual field, retinoscopy was used by Erichsen [1979], as previously used for the human eye Rempt et al. [1971]. Results of this study are shown in Figure 2.26, and the findings indicate that neither refractive error (defocus) nor astigmatism significantly change when we move along the horizontal meridian, even at large angles away from the fovea central axis, as we could expect in the human eye. In contrast, measurements of refractive state of the pigeon eye for different elevations showed that the amount of defocus does change (i.e. increasing myopia in the lower frontal field) but astigmatism remains low and reasonably constant as mentioned in 2.26.

This regional refractive error in lower elevations has been described as a Lower Field Myopia Hodos and Erichsen [1990] not only for birds but also for anphibians Schaeffel et al. [1994], the dioptric state corresponding to the eye-ground distance as shown in Figure 2.27. This myopia is likely to be an adaptation to the environment and cannot be considered pathologic, this appearing to be common in other ground birds but not present in raptors.

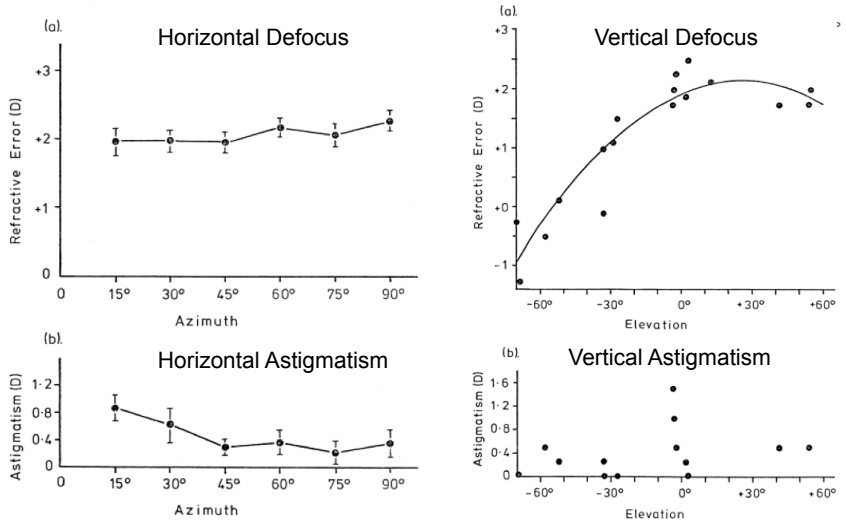

FIGURE 2.26 – Refractive state of the pigeon eye along the horizontal meridian defocus (right top) and astigmatism (right bottom). Refractive state of the pigeon eye along the vertical meridian defocus (right top) and astigmatism (right bottom). Adapted from Erichsen [1979]

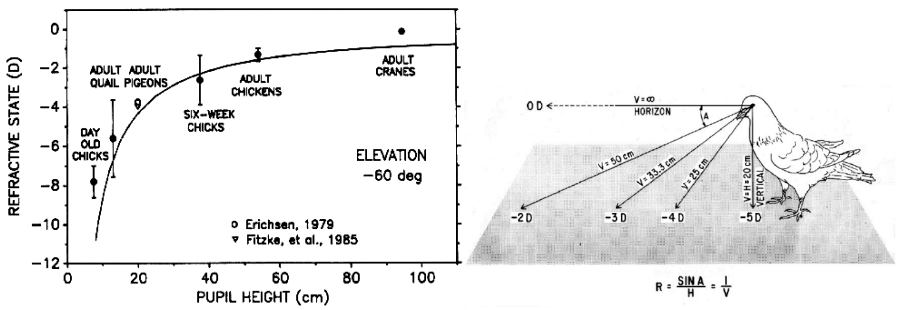

FIGURE 2.27 – Refractive state of different birds depending on their height. Adapted from Erichsen [1979]

Chapter 3

Aberration Measurement

During the past few decades, the advances in measuring ocular aberrations have been noteworthy. As mentioned before, this practice has been implemented in an increasing number of eye clinics. Indeed, the possibility of measuring monochromatic aberrations in a clinical environment as part of a routine examination potentially involves a large population. This quantitative knowledge about optics allows a better understanding of the process of image formation on the retina, in addition to producing a wider knowledge about the influence of ocular aberrations on the overall retinal image quality and the performance of the visual system.

Different approaches can be taken to describe the optical quality of the eye. For example, the more exhaustive explanations focus on mathematical descriptions, as in Goodman [1968], Born and Wolf [1997] and Nussbaum [2005]. For simplicity, in this section, we are going to review briefly some basic optics concepts, including a description of **Seidel Aberrations** and **Chromatic aberrations** as well as the influence of **Diffraction** on the quality of the final image yielded by the human eye. Then, the different ways of measuring ocular aberrations will be explained, starting with a description of several useful concepts, such as wavefront aberration, and concentrating on their relationship with Zernike polynomials as means of describing the quality of the retinal image.

This comprehensive explanation of the Zernike polynomial and its use to describe the **wavefront aberration** is necessary because the present study utilized this mathematical formalism. Following an historical review of the instrumentation used to measure aberrations, an extensive description will be provided of the development of the Hartman-Shack Wavefront Sensor, which was used to obtain the data for this study.

3.1 Image Formation

If we imagine the eye as an optical system, there are some parameters that we need to define in order to describe the behavior of that optical system. We can simplify the eye as one lens that focuses a beam of light exiting the object plane into the focal plane. If we start with Snell's law (see 3.1), we can confirm that, when a ray is coming to an interface that separates two different media, the ray can either be reflected or refracted as a function of the value of the refractive index represented by n_i in the object space and n_f in the image space. Then, the relation between angles of incidence and refraction can be calculated according to the Equation 3.1 (see Figure 3.1).

$$\frac{n_i}{n_f} = \frac{sin(\theta_f)}{sin(\theta_i)} \tag{3.1}$$

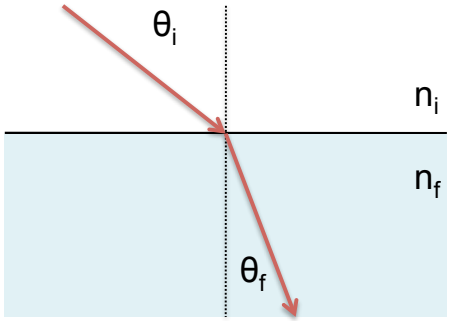

FIGURE 3.1 – Representation of the refraction of a ray according to Snell's Law

The reflection happens when

$$\theta_i = \theta_f$$

If we consider small angles we could ignore the sin and approximate $\sin\theta \approx \theta$ this supposition corresponds to the *paraxial approximation*. From an image point S, we will obtain a perfect image point P, as shown in Figure 3.2 obtaining the so called stigmatic representation, represented by blue rays.

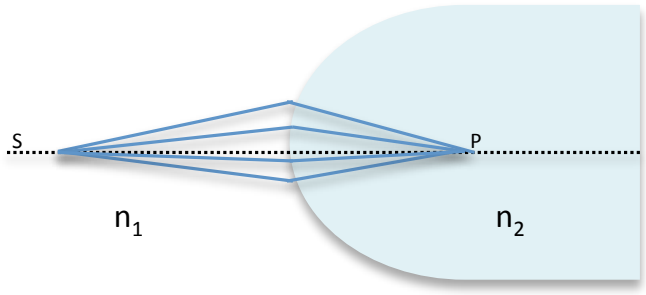

FIGURE 3.2 – Stigmatic representation of a point.

If, on the contrary, the angle θ is larger and the above mentioned approximation can not be taken, i.e. this situation occurs when more peripheral rays are incident, we have to take into account the Taylor expansion (see 3.1), this case is represented in the figure 3.2 by the red rays.

$$sin\theta = \theta - \frac{\theta^3}{3!} + \frac{\theta^5}{5!} - \frac{\theta^7}{7!} + \dots$$

If we do not truncate the above equation, there will be **third-order aberrations** to take into account. The ray traces for paraxial rays are depicted in the Figure 3.3.

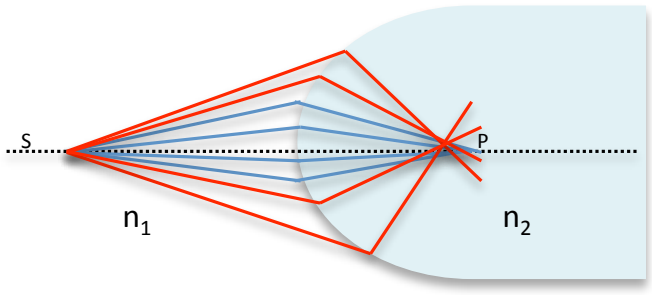

FIGURE 3.3 – Representation of a point for non-paraxial approximation, the red rays represent non paraxial rays and blue ones the paraxial ones

The wave aberration function, $W(x, y)$ is by definition the distance in optical path length from the reference sphere to the wavefront in the exit pupil, measured along a ray perpendicular to the aberrated WF, as shown in Figure 3.4.

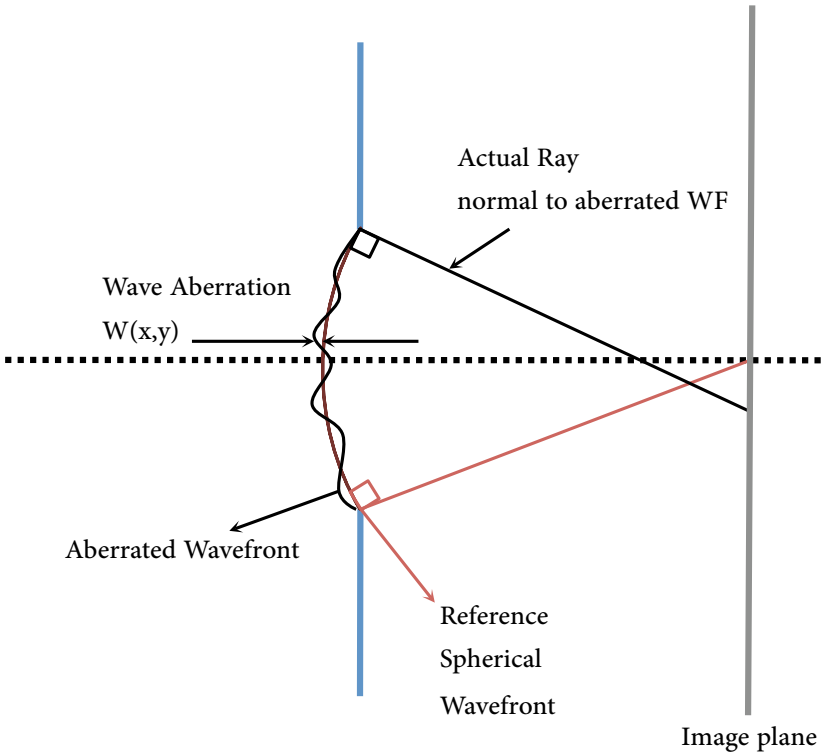

FIGURE 3.4 – Representation of the wavefront function

If we use the Taylor expansion polynomial in terms of the object height h and pupil polar coordinates (r, θ), we will obtain the next expression:

$$W(r,\theta) = W_{000} + W_{011} r cos(\theta) + W_{020} r^2 + \dots$$

$$+W_{040} r^4 + W_{131} h r^3 cos(\theta) + W_{222} h^2 r^2 cos^2(\theta) + \dots$$

$$+W_{222} h^2 r^2 cos^2(\theta) + W_{220} h^2 r^2 + W_{311} h^3 r cos(\theta) + \dots$$

Those terms can be easily identified with the Primary Seidel aberrations :

$$r^2 \rightarrow Defocus$$

$$r^4 \rightarrow Spherical\ Aberration$$

$$h r^3 cos(\theta) \rightarrow Coma$$

$$h^2 r^2 cos^2(\theta) \rightarrow Astigmatism$$

$$h^2 r^2 \rightarrow Field\ Curvature$$

$$h^3 r cos(\theta) \rightarrow Distorsion$$

The description and use of Seidel aberrations started in the middle of the 19th century to quantify and describe the degradation of images when we are outside of the paraxial approximation for centered optical systems.

3.1.1 Description of Zernike Polynomials

The Zernike polynomials are a set of functions that are orthogonal over a unit circle. For a complete derivation, see Born and Wolf [1997]. This description of the wave aberration in terms of these polynomials is very convenient for several reasons :

- It is the preferred way to describe the aberrations in the optical community and is the formal convention adopted by the OSA (Optical Society of America).
- The entry pupil of the human eye is considered circular over the pupil plane.

- Some terms can be directly related to well known ocular aberrations or ametropia, e.g, the 5th term of the expansion is equivalent to defocus. To describe astigmatism, we can use the 4th and 6th terms.
- The shape of each polynomial describes perfectly the deformation of the surface (in our case, the wavefront).
- They are additive; if we sum up one or more polynomic terms, it is possible to describe the shape of a more complex wavefront.
- The Zernike expansion can be truncated at any given order, depending on the needed accuracy.
- These polynomials are mutually orthogonal, and therefore mathematically independent, making the variance of the sum of the modes equal to the sum of the variances of each individual mode.
- They can be scaled to zero, and the non-zero order modes have zero mean and unit variance, making comparison between modes meaningful.

If we define the Zernike polynomials in polar coordinates (ρ, θ), where ρ is the radial coordinate ranging from 0 to 1 and θ is the azimuthal component ranging from 0 to 2ϕ. .

There are three components in each Zernike polynomials:

- Normalization factor represented byN_n^m.
- Radial dependent component, which is polynomial.
- Azimuthal dependent component, which is sinusoidal.

To avoid any ambiguity, a double index scheme is used to describe these functions, the index n describing the highest power (order) of the radial polynomial and the index m describing the azimuthal frequency of the sinusoidal component. The Zernike polynomials are defined as

$$Z_n^m(\rho, \theta) = N_n^m R_n^m(\rho) \cos(m\theta) \qquad if \quad m \leq 0 \tag{3.2}$$

$$Z_n^m(\rho,\theta) = -N_n^m R_n^m(\rho)\cos(m\theta)) \qquad if \quad m<0 \tag{3.3}$$

The definition expressed by equations 3.2 and 3.3 can describe uniquely any polynomials except for the normalization constant , being $R_n^{|m|}(\rho)$ given by:

$$R_n^{|m|}(\rho) = (-1)^s \sum_{s=0}^{(n-|m|)/2} \rho^{n-2s} \frac{(n-s)!}{s!\,[n+(n+|m|/2-s)!]\,[(n-|m|/2-s]!}$$

The normalization factor is defined by:

$$N_n^m = \sqrt{\frac{2(n+1)}{1+\delta_{m_0}}} \tag{3.4}$$

where δ_{m_0} is the Kronecker delta function (i.e . $\delta_{m_0} = 1$ for $m = 0$, and $\delta_{m_0} = 0$ for $m \neq 0$).

The radial order n is a positive integer or zero and the angular frequency m can only take on the values -n, -n + 2, -n +4, ...n.

Throughout the present study, the OSA convention will be used regarding definition, normalization and sign. In table 3.1, we can see the mathematical description of the Zernike polynomial functions and the common name for each.

The Zernike polynomials can be described as combination of Seidel aberrations.

j	n	m	Z_j	Aberration
1	0	0	1	Piston
2	1	1	$2\rho\ \sin\theta$	Tilt along y-axis
3		-1	$2\rho\ \cos\theta$	Tilt along x-axis
4	2	0	$\sqrt{3}\ (2\rho^2-1)$	Defocus
5		-2	$\sqrt{6}\ \rho^2\ \sin 2\theta$	Astigmatism at 45 °
6		2	$\sqrt{6}\ \rho^2\ \cos 2\theta$	Astigmatism at 0 °
7	3	-1	$\sqrt{8}\ (3\rho^3-2\rho)\ \sin\theta$	Coma along y-axis
8		1	$\sqrt{8}\ (3\rho^3-2\rho)\ \cos\theta$	Coma along x-axis
9		-3	$\sqrt{8}\ \rho^3\ \sin 3\theta$	Trefoil at 45 °
10		3	$\sqrt{8}\ \rho^3\ \cos 3\theta$	Trefoil at 0 °
11	4	0	$\sqrt{5}\ (6\rho^4-6\rho^2+1)$	Spherical aberration
12		2	$\sqrt{10}\ (4\rho^4-3\rho^2)\ \cos 2\theta$	Secondary astigmatism at 45 °
13		-2	$\sqrt{10}\ (4\rho^4-3\rho^2)\ \sin 2\theta$	Secondary astigmatism at 0 °
14		4	$\sqrt{10}\ \rho^4\ \cos 4\theta$	Tetrafoil at 0 °
15		-4	$\sqrt{10}\ \rho^4\ \sin 4\theta$	Tetrafoil at 45 °
16	5	1	$\sqrt{12}\ (10\rho^5-12\rho^3+3\rho)\ \cos\theta$	Secondary coma along x-axis
17		-1	$\sqrt{12}\ (10\rho^5-12\rho^3+3\rho)\ \sin\theta$	Secondary coma along y-axis
18		3	$\sqrt{12}\ (5\rho^5-4\rho^3)\cos 3\theta$	Secondary trefoil at 0 °
19		-3	$\sqrt{12}\ (5\rho^5-4\rho^3)\sin 3\theta$	Secondary trefoil at 45 °
20		5	$\sqrt{12}\ \rho^5\ \cos 5\theta$	Pentafoil at 0 °
21		-5	$\sqrt{12}\ \rho^5\ \sin 5\theta$	Pentafoil at 45 °

TABLE 3.1 – The first 21 Zernike circle polynomials and their common names

3.1.2 On axis Seidel Aberrations

Spherical aberration Spherical aberration is the only high order aberration that is also present for object points placed on the optical axis for rotationally symmetric systems. In this case, the rays entering in the optical system are refracted more if they are more peripheral, i.e. the focal point for each ray depends on the distance from the central point of the lens or optical system. This means that, the higher the angle, the more aberrated are the rays because they are farther from the paraxial limit. An eye with spherical aberration is shown in Figure 3.5.
The term representing this aberration has a dependency on r^4.

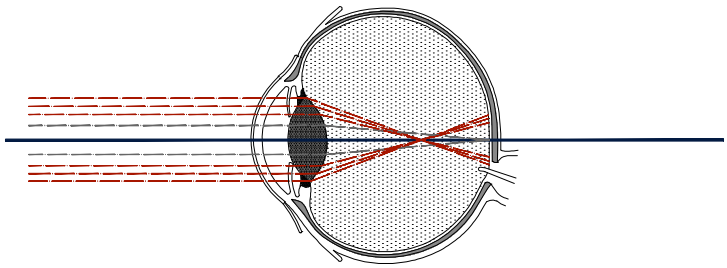

FIGURE 3.5 – Schematic representation of rays affected by spherical aberration, on the human eye.The amount of aberration is not to scale it has been incremented for illustrating purposes

When spherical aberration is present, non-paraxial rays do not intersect at paraxial focus. The value of spherical aberration is considered be positive if the rays cross in front of the retina, whereas in the case of negative spherical aberration, rays will cross behind it. The effect of spherical aberration on the retinal image can be seen in Figure 3.6.

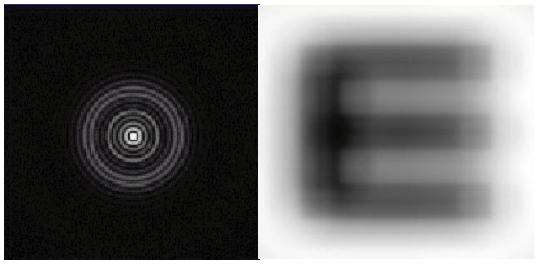

FIGURE 3.6 – Representation of an aberrated PSF and simulation of the spherical aberrated image of a Snellen's E. Adapted from http://www.cvs.rochester.edu/williamslab/r$_c$*ontacts.html*

3.1.3 Off axis Seidel Aberrations

The main visual tasks in normal life, specially those requiring high resolution, are performed using central vision, and for normal subjects, the amount of aberrations is lower for this position. By contrast, peripheral vision is used largely to detect movement and guide our own movements in the environment. Previous studies have shown that there are a great deal more aberrations in peripheral optics, which produce a correspondingly lower quality image in these eccentric regions of the retina— Gustafsson et al. [2001].
On the other hand, the lower density of photoreceptors in the periphery is correspondingly affecting the resolution with which a person can perceive an image, thus resulting in poorer vision so that the person would not see as well in the peripheral region even if central optics were used Frisen and Glansholm [1975]. The relative distribution of cones and rods in the retina also affects this difference in vision. In the fovea, the density of cones is higher and the information gathered from them is directly sent to the brain, but once we move to more peripheral parts of the retina, the density of cones (and ultimately rods) decreases dramatically, and the connection with the brain is not one-to-one between cone or rod

and ganglion cell; several photoreceptors are converging onto a single ganglion cell. In the macula, the main type of photoreceptors present is the cones, which are specialized for color perception, but in the peripheral region, where most of the rods are located, the photoreceptors are farther apart and coupled together so that a number of receptors share the same connection to the brain. As result, peripheral vision would never provide the same resolution as central vision does, even if the optics were corrected.

Coma Coma aberration is an off-axis aberration, which is present when the object points are placed out of axis. The final image is straightened out to a coma shape; the distribution of the light is not uniform along this structure and the system (in this case the eye) may produce a sharp image in the center of the field but become increasingly blurred toward the edges. Figure 3.7 shows the retinal image affected by coma. The term representing this aberration has a dependency on $hr^3cos(\theta)$

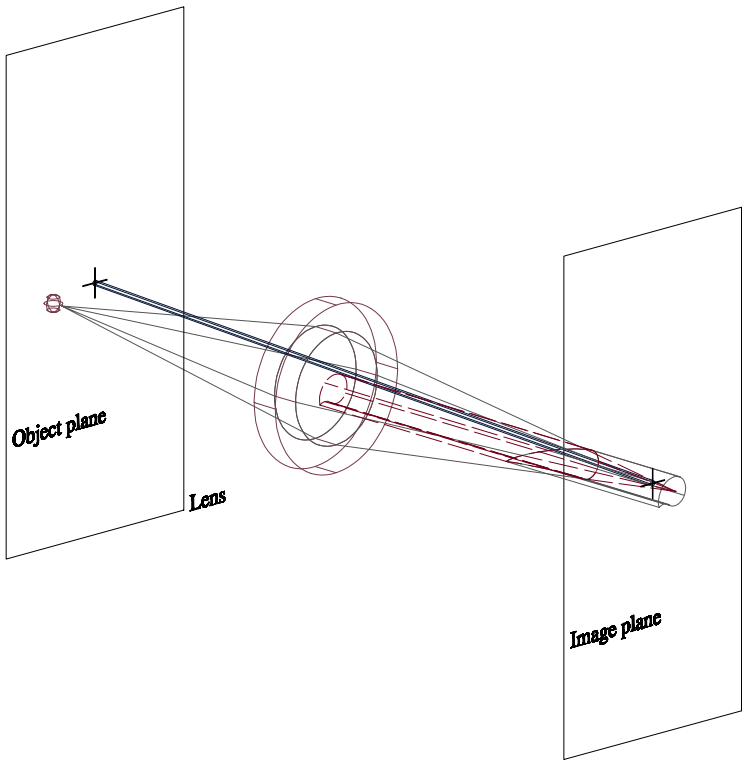

FIGURE 3.7 – Representation of off-axis rays affected by coma aberration.

Optical systems affected by coma, the paraxial rays are focused correctly, but the peripheral rays are spread out, ending up in a blurred image. In Figures 3.8 and 3.9, we can see the simulation of the effect of coma aberration (vertical and horizontal respectively) on PSF and the degradation produced on the image of a Snellen E.

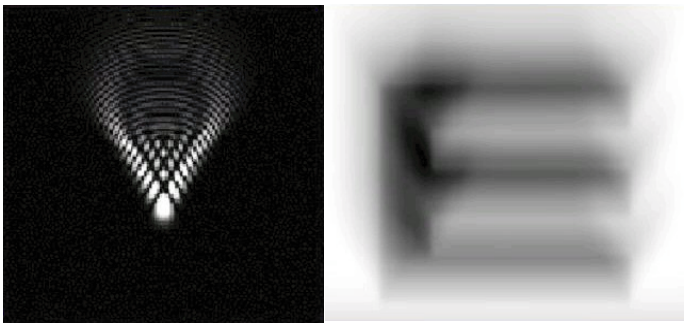

FIGURE 3.8 – Simulation of the effect produced by vertical coma on a Snellen E image. Adapted from http://www.cvs.rochester.edu/williamslab.

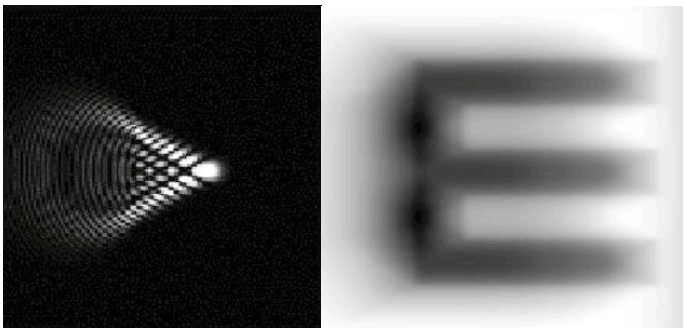

FIGURE 3.9 – Simulation of the effect produced by horizontal coma aberration on a Snellen E image. Adapted from http://www.cvs.rochester.edu/williamslab.

Astigmatism Another off-axis aberration is oblique astigmatism, which happens when the angle subtend for the object is bigger than the paraxial limit. It causes radial and tangential lines in the object plane to focus sharply at different distances in the image space.

Oblique astigmatism occurs for off-axis objects because of the oblique illumination of the lens. In the sagittal plane, the rays will come into the lens at an oblique angle, and this angle increases with the distance between the object and the optical axis. Because the rays need to go through a thicker part of the lens with a greater refractive power, these rays will focus in Fs, known as **sagittal focus**. In the meridional plane (see figure 3.10), the rays are coming into the lens at an oblique angle, and they are focused at Ft, known as **transverse focus**.

There will be two focal lines: one corresponds to the sagittal plane and the other corresponds to the tangential or transverse plane. This fact greatly blurs the final image because there is no single point where the rays meet. The images will be elongated either radially or tangentially depending on whether the focal plane is nearer to the sagittal or transverse focus, respectively, so the best possible image is located in between the two focal lines, i.e. the least confusion circle. The term representing this aberration has a dependency on $h^2r^2cos^2(\theta)$.

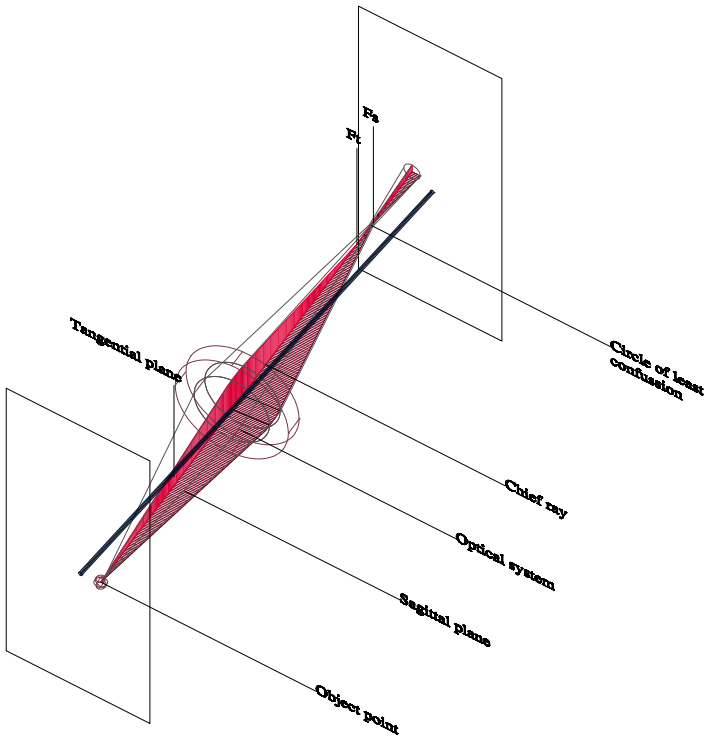

FIGURE 3.10 – Representation of oblique astigmatism.

Distortion This aberration does not produce a loss of information in the image. Although the image differs geometrically from the object, all the object points are correctly focused in the image plane. There are two types of distortion, **positive** or pincushion and **negative** or barrel distortion, as shown in figure 3.11. As distortion increases, although the image appears in focus over the entire field, the size of the image differs at the center and periphery of the field of view. The term

representing this aberration has a dependency on $h^3 r cos(\theta)$

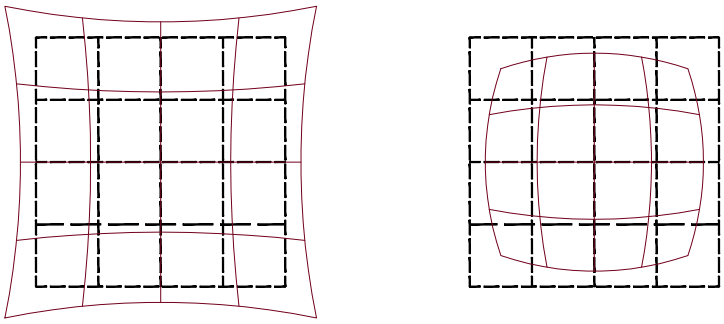

FIGURE 3.11 – Representation of distortion aberration, (right) barrel distortion, (left) pincushion distortion.

Field Curvature This is another off-axis aberration. In this case, the representation of a point is stigmatic, which means that we will have another point on the image plane, but the representation of an object plane is not a plane as the paraxial optics predict. The **focal plane** is not flat but rather curved. If the curvature in the image is inwards, the aberration is called positive, and if the curvature is outwards, the aberration is negative. Figure 3.12 represents the effect of this aberration for the human eye. The term representing this aberration has a dependency on $h^2 r^2$. If the optical system is mainly composed of positive surfaces, which is the case in the eye, the final image will be in front of the ideal image plane, which is known as the Gaussian plane. For small angles, the image is in a plane called the Petzval surface. This aberration usually occurs together with astigmatism, which is due to the fact that both aberrations are off-axis aberrations. Since the retina is curved, this aberration has little effect on the quality of the final retinal image. For different optical systems where the final image plane is flat the effect of field curvature is not negligible distorting the final image considerably.

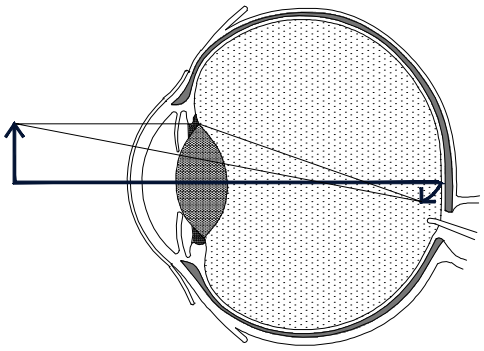

FIGURE 3.12 – Representation of the effect of Field Curvature on the final image.The amount of aberration is not to scale it has been incremented for illustrating purposes

3.1.4 Chromatic aberration

Chromatic aberrations are inherent to all of optical systems because all the media are dispersive, which means that the value of the refractive index depends on the wavelength, as shown in the equation 3.5.

$$n = n(\lambda) \tag{3.5}$$

In our specific case, chromatic aberration will obviously be present in the human eye. We can divide the chromatic aberration into two terms: longitudinal chromatic aberration (**LCA**) and transversal chromatic aberration (**TCA**). When different wavelengths are focused at different image planes, we will have (**LCA**), and a variation on refractive power depending on wavelength will be present. In contrast, (**TCA**) is present when different wavelengths are focused at different positions in the focal plane. In figure 3.13, we can see the effect of (**LCA**) and how the different wavelengths focus at different distances; therefore the human eye has different refractive power depending on the wavelength of light. In practice, the longitudinal and transversal components are coexistent.

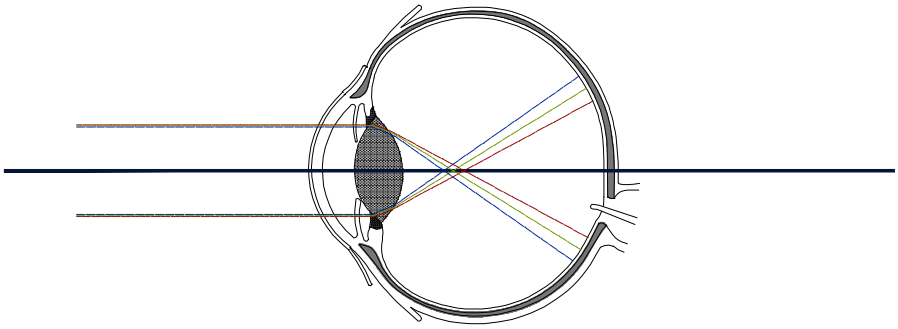

FIGURE 3.13 – Representation of longitudinal chromatic aberration.

The influence and impact of chromatic aberration has been studied by several investigators in order to clarify the impact of this chromatic shift on visual performance, as in Marcos et al. [1999] and Thibos et al. [1990] where we can find an in depth study and a careful description of the theory of chromatic aberrations as well as ways of measuring it. The relative impact of this aberration has also been explored in a model eye Villegas et al. [1996]. The possibility for having a compensating mechanism of this effect has been explored by McLellan et al. [2002].

3.2 Wavefront Aberrations

Until now, we have used a geometrical description of the aberrations, but to get a better understanding, we need to explain the principles of wave optics.

The accuracy of the paraxial approximation is restricted to small angles of incidence into the optical system because, in that case, the sine of the angle may be approximated by the angle itself, according to the first term of the Taylor expansion.
In other situations, this approximation can not be taken, and we need to use the term **aberration** to describe the wavefront. Aberration means that not all of the rays proceeding from the object are focused in the image plane, and this results

in a worsening or degrading of the final image.
Optical aberrations in the human eye can impose a limit on visual performance. As previously discussed, the main contributors to the aberrations in the eye are the anterior surface of the cornea and the crystalline lens. The influence of aberrations on the final quality of the retinal image is a central problem in physiological optics. Refractive errors may be corrected by glasses, contact lenses or even with refractive surgery, but a more comprehensive study of the wavefront will provide much more information related to the quality of the retinal image of the eye, allows us to discover whether high order aberrations are present (as well as their extent) when we are not taking the paraxial approximation. These aberrations are also known collectively as the Seidel aberrations when we include only up to the third order. Aberrations are called third order aberrations because they cannot be seen in the so-called first order approximation.

In this study, we are going to describe the performance of the eye as an optical system in terms of the wave aberration, $W(\rho, \theta)$. The wavefront can be described as the surface that contains all the points that have the same phase, and the optical rays are always perpendicular to this surface. If the system is perfect and no aberration is present from a spherical wave, all the rays emerging from a point P in the object plane will converge at another point P' on the image plane, as represented in Figure 3.14.

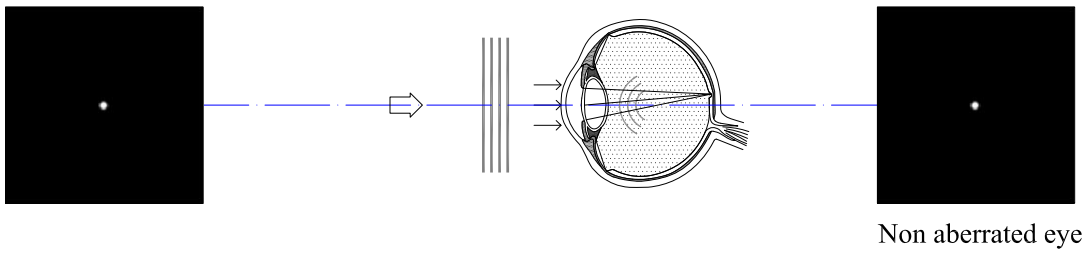

FIGURE 3.14 – Representation of an stigmatic optical system, in this case an ideal aberration-free human eye

If aberrations are present, the wave is no longer spherical and the rays emerging from an object point are not going to converge at one single image point, as represented in Figure 3.15.

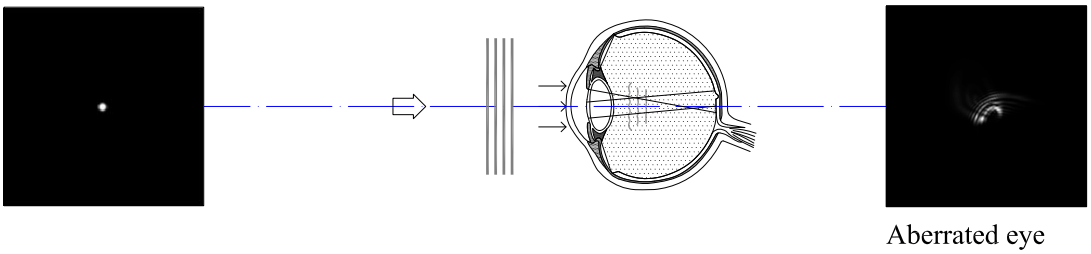

FIGURE 3.15 – Representation of an aberrated optical system, in this case the human eye

The aberration associated with a given wavefront can be described in different terms. The difference between the real wavefront and an ideal one can be measured at the exit pupil, and the transverse aberration associated with each ray can be described as the difference in position from its ideal position in the image plane. In mathematical terms, the shape of the wave coming out from the eye can be described as

$$W(\rho,\theta) \approx \sum_{n} \sum_{m} C_n^m Z_n^m(\rho,\theta) \tag{3.6}$$

In this equation, $W(\rho,\theta)$ represents the wavefront measured and, C_n^m represents the value of the Zernike coefficients i(measured in microns) and Z_n^m represents the Zernike polynomial function associated to this coefficient.

Since the polynomials are orthogonal over a circle unit, they are usual to represented in polar coordinates, using the convention shown in Figure 3.16:

3.2.1 Representation of the wave aberration using Zernike Polynomial

The ANSI report and Thibos et al. [2000] have been followed. The nomenclature and description of ocular aberrations.This expression, Z_n^m, represents any Zernike polynomial, where n corresponds to radial order and m to meridional frequency, both represented in cartesian coordinates. According to OSA regulations, it is also common to represent theta as a function of radial coordinates. In that case,

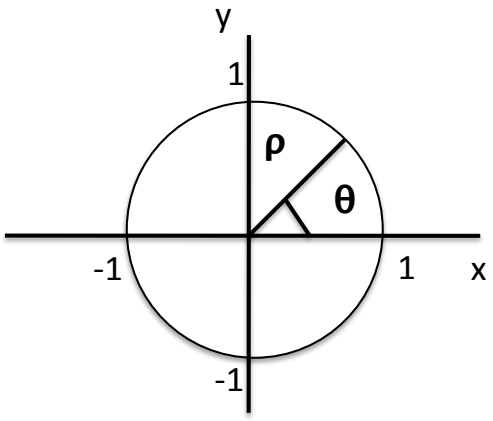

FIGURE 3.16 – Representation of a generic circle unit were the Zernike coefficients are defined

we can redefine the Zernike polynomials in polar coordinates (ρ,θ).We can then represent the wavefront aberration in polar coordinates in terms of the Zernike polynomial as follows :

$$W(\rho,\theta) = \sum_{i=0}^{n} a_i Z_i(\rho,\theta) \tag{3.7}$$

The coefficients are given by the next integral over the area of the circular aperture A:

$$a_i = \int\int_A W(\rho,\theta)\, Z_i(\rho,\theta)\, d\rho d\theta \tag{3.8}$$

For a better understanding of the aberration description, it is necessary to define the useful RMS concept. The root mean square is defined in statistics as a measure of the magnitude of a varying quantity, and it is calculated as the square root of the mean of the sum of the squared values of the quantity. We can define the RMS as written in equation 3.9. Where $W(X,Y)$ represents the wave aberration and $P(X,Y)$ represents the pupil function. In this case, a circular

pupil will be used.

$$RMS = \sqrt{\frac{\int\int W(X,Y)^2 dxdy}{P(x,y)^2}} \tag{3.9}$$

In our particular case and for wavefront description purposes, we can use an equivalent definition for the RMS as the square root of the sum of the squares of a given number of Zernike coefficients, as described in 3.10 The total value of RMS can give us a general estimation of the total amount of all considered aberrations.

$$RMS = \sqrt{\frac{\int\int W(X,Y)^2 dxdy}{P(x,y)^2}} = \sqrt{\frac{\sum_{m,n} (c_n^m)^2 P(x,y)^2}{P(x,y)^2}} = \sqrt{\sum_{m,n} (c_n^m)^2} \tag{3.10}$$

3.3 Retinal Image Quality

From the wavefront exiting the eye, we cam estimate the light distribution on the retina. For that purpose, we will use the formalism of Fourier Optics, in this work, we will give a general overview. For a more detailed information, see Goodman [1968]

If we describe by $W(\rho, \theta)$ the wavefront deviation over the exit pupil compared to a perfect sphere on a point A at the image plane we can calculate (using equation 3.11) the intensity in the image plane as shown in Born and Wolf [1997]

$$I(x,y) = C \left| \int_{-\infty}^{+\infty} \int_{-\infty}^{+\infty} P(\xi,\eta)\, exp^{-\frac{2\pi i}{\lambda R}(x\xi + y\eta)}\, d\xi d\eta \right|^2 \tag{3.11}$$

Being C a constant that we can omit for simplicity, λ the wavelength, (x, y) the coordinates with respect A and R the distance from the exit pupil to the image plane,

$$P(\xi, \eta)$$

the pupil function defined as follows :

$$P(\xi,\eta) = exp\left[\frac{2\pi i}{\lambda} W(\xi,\eta)\right] \tag{3.12}$$

If (ξ, η)acquire values within the aperture of the system and being 0 elsewhere.

If we define the PSF (point-spread-function) as the illuminance distribution of a point source of light produced by an optical system, we can identify this function with the previous equation 3.11. Alternatively, for the final image, its mathematical shape is described by equation 3.13. Following this definition, when no aberrations are present, the PSF of an image point corresponds to the Fourier Transform of the pupil function. If the pupil is assumed to be circular, then we will obtain the Airy disk.

$$PSF = |FT(P(x,y))|^2 \tag{3.13}$$

The PSF can be related to the wave aberration function by Fourier Transform. The value of the PSF can be affected by various conditions such as diffraction and/or scattering produced by the ocular media. The wider the PSF, the more aberrated is the eye (or optical system).

If we consider incoherent illumination is also true that the intensity of the signal I_o (i.e.light) after going through the eye can be described as proportional of the convolution of the incoming light intensity I_i and the point spread function:

$$I_o(x,y) = \int_{-\infty}^{+\infty} \int_{-\infty}^{+\infty} PSF(x-x_1, y-y_1)\, I_i(x_1,y_1)\, dx_1 dy_1 \tag{3.14}$$

or alternatively applying Fourier Transform, being (x, y) coordinates on the image plane and (x, y) :

$$I_o(x,y) = FT^{-1} FT\{I_i(x_1,y_1)\}\, FT\{PSF(x,y)\} \tag{3.15}$$

It is common to describe the goodness of the PSF by means of the Strehl ratio which is a number between zero and one that corresponds to the fraction defined by the maximum value of the aberrated PSF, normalized to the maximum of the diffraction-limited PSF, as represented by equation 3.16.

$$StrehlRatio = \frac{maximum(PSF_{aberrated})}{maximum(PSF_{diffraction})} \tag{3.16}$$

The Fourier Transform of the PSF is the optical transfer function, OTF, a complex function that evaluates, for each frequency present in the object, how the contrast is degraded by the optical system and can be described by equation 3.17.

$$OTF(x,y) = MTF(x,y)PTF(x,y) \tag{3.17}$$

The modulation transfer function, the modulus of the function, is the part of the OTF most frequently used to describe the overall optical quality of the human eye. Its corresponding modulus represents the spatial frequency response of the optical system and is used to describe the reduction in contrast from object to image.

3.3.1 Wave aberration and Optical Transfer Function

The OTF, as mentioned above, is a complex function that comprises two parts:

- The Modulation Transfer Function, MTF.
- The Phase Transfer Function , PTF.

The MTF defines how much contrast is transferred by the optical system to the image plane as a function of the spatial frequency. We can establish a relationship between OTF and Wavefront Aberration via the generalized pupil function, as follows:

$$P(x,y) = A(x,y)e\frac{(-2\pi i)W(x,y)}{\lambda} \tag{3.18}$$

where

$$A(x,y) \tag{3.19}$$

represents the generalized pupil transmission function and gives information about the geometry of the pupil,

$$P(x,y) \tag{3.20}$$

is the generalized pupil function,

$$W(x,y) \tag{3.21}$$

represents the wave aberration function in cartesian coordinates. In conclusion, the retinal image quality can be determined by knowing the wavefront aberration and vice versa.

3.3.2 Calculation of Sphero-Cylindrical refraction form Zernike Coefficients

All off the wavefront measurements performed throughout this study have been made by means of the HSWFS. described in the section ref, it provides as output a series of Zernike Coefficients up to 5th order from each chosen eccentricity. In the field of wavefront aberrometry, conventional sphero-cylindrical refractive errors are called aberrations of the second Zernike order.

In the case of avian eye and to make it possible to compare to previous studies such as Erichsen [1979] as well as retinoscopy measurements wavefront information has to be analyzed in order to provide the spherocylindrical equivalent.

Different approaches can be taken to calculate refraction from wavefront aberrations data. The first is based on calculations made at the exit pupil plane, but alternatively we can use metrics that are based on the retinal image quality see Applegate et al. [2006] and William [2006].

Refractive error is commonly predicted to minimize the RMS value of the wavefront error measured at the pupil exit. In this way we will know the shape of a toroidal wavefront that will compensate the measured aberrated wavefront.

If we consider the convergent aberrated wavefront exiting from the eye, convergent as shown in the Figure 3.3.2, we can calculate the equivalent focal length by means of the following expression :

$$(f-h)^2 = f^2 - R^2 \tag{3.22}$$

Taking into account that f-h is a positive quantity, we will take just the positive root, and using the binomial approximation of $f - \sqrt{f^2 - R^2}$ for $R \ll f$, we can find the following relationship:

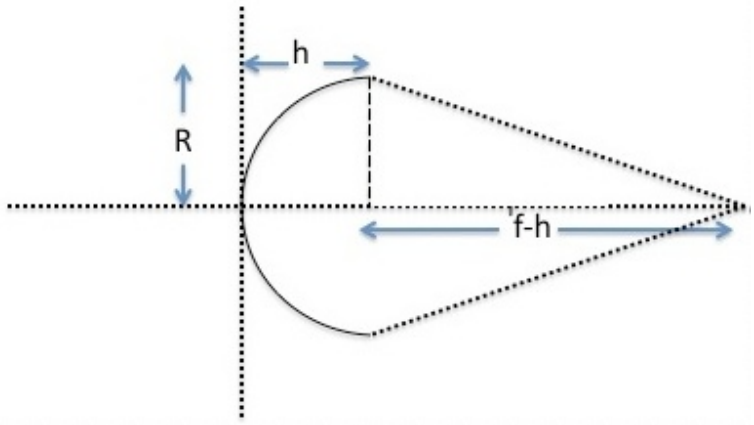

FIGURE 3.17 – The geometry of a converging spherical wavefront for determination of the sag h at the pupil edge

$$h = f - \sqrt{f^2 - R^2} = f - f\left[1 - \left(\frac{R}{f}\right)^2\right]^{1/2} \approx f - f\left[1 - \frac{(R/f)^2}{2}\right] = \frac{R^2}{2f} \tag{3.23}$$

From the definition of Zernike coefficients, we know that defocus is $2\sqrt{3}c_4Z_4$ and astigmatism at 0∘ and 45∘ is represented by $\sqrt{3}c_6$ and $\sqrt{3}c_4$ respectively. Identifying those values with equation 3.3.2, we obtain the expression of spherocylindrical power as follows:

$$M = -4\frac{\sqrt{3}}{R^2}c_2^0 \tag{3.24}$$

$$C_0 = -4\frac{\sqrt{6}}{R^2}c_2^2 \tag{3.25}$$

$$C_{45} = -4\frac{\sqrt{3}}{R^2}c_2^{-2} \tag{3.26}$$

where the coefficients and the radius of the pupil, R , are in meters to give the refractive correction expressed in diopters.

Alternatively, we can used the Seidel refraction expressed by equations 3.27 , 3.28 and 3.29 which include higher orders the Zernike expansion. For the calculation of refraction, this approach has been shown and analyzed by Guirao and Williams [2003] and Thibos et al. [2004]. The general conclusion is that minimize of RMS is not enough in the presence of large high order aberrations, and a more accurate result of the subjective refraction will be given by use of metrics that are based on the retinal image quality.

$$M = -4\frac{\sqrt{3}}{R^2}c_2^0 + 12\frac{\sqrt{5}}{R^2}c_4^0 - 24\frac{\sqrt{7}}{R^2}c_6^0 + 40\frac{\sqrt{9}}{R^2}c_8^0 - ... \tag{3.27}$$

$$C_0 = 4\frac{\sqrt{6}}{R^2}c_2^2 - 12\frac{\sqrt{10}}{R^2}c_4^2 + 24\frac{\sqrt{14}}{R^2}c_6^2 - 40\frac{\sqrt{18}}{R^2}c_8^2 + ... \tag{3.28}$$

$$C_{45} = 4\frac{\sqrt{6}}{R^2}c_2^{-2} - 12\frac{\sqrt{10}}{R^2}c_4^{-2} + 24\frac{\sqrt{14}}{R^2}c_6^{-2} - 40\frac{\sqrt{18}}{R^2}c_8^{-2} + ... \tag{3.29}$$

3.4 Diffraction

Due to the dual nature of light, the image formed by an optical system of a point of light will never be another point. On the contrary, the image quality will be limited by diffraction. Due to the circular shape of the pupil, we will obtain the so called Airy disk. Hence, from a perfect plane wave in a non aberrated system, the image in the retina will be the Airy disk as shown in Figure 3.18. In that case, if we assume that the only limitation to the image forming system is diffraction, we can suppose that the diverging beam of light that emerges from the object point, after going through the eye, will be converted into a converging beam focusing on one point contained on the focal plane. In the case of the human eye, the image plane is the retina.

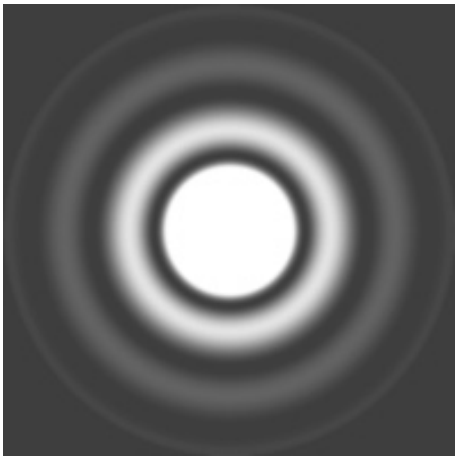

FIGURE 3.18 – Representation of Airy's disk. Adapted from http://www.universetoday.com.

The mathematical representation of this aberration-free diffraction pattern for a given diameter represented by D, the size of the diameter of the Airy disk, can be calculated by using the following expression, where r_1 represents the radius of the central circle of the Airy pattern and λ_z represents the used wavelength.

$$r_1 = 1.22\frac{\lambda_z}{D} \tag{3.30}$$

The size of the Airy disk depends on pupil size as represented in Figure 3.19. The bigger the pupil, the smaller is the diameter of the Airy disk and therefore the effect of diffraction on the final image quality. We could argue that the best image quality of a non aberrated optical system occurs when the aperture is maximal, but if we take a normal eye with both spherical and cylindrical errors corrected, we can see that the effect of aberrations increases as we increase the pupil size, as shown in Figure 3.20.

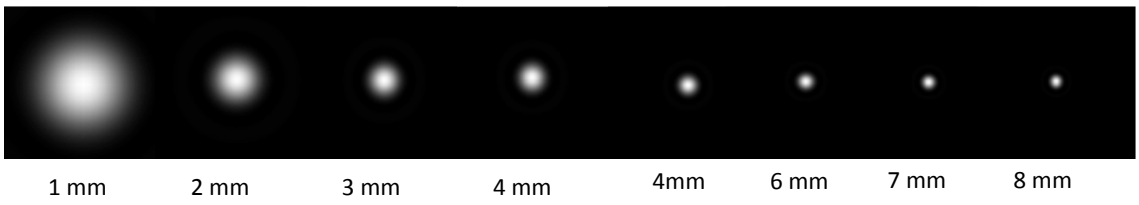

FIGURE 3.19 – Representation of the size of the Airy disk depending on pupil size. Adapted from http://vision.berkeley.edu

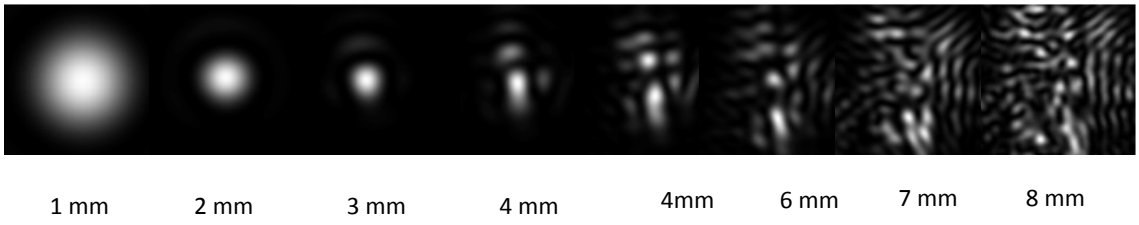

FIGURE 3.20 – Representation of the effect of aberrations depending on pupil size. Adapted from http://vision.berkeley.edu

We could affirm that the resolving power of the eye is hence limited by *diffraction* and *aberrations*.

In other words he bigger the entrance pupil of the optical system, the smaller is the effect of the diffraction, but in the case of the human eye, there is a trade off because the bigger the pupil, the larger is the influence of the higher order aberrations (HOA).

For smaller pupils, even in the case of aberrated systems, the image of the PSF (point-spread function) is limited only by diffraction, but for increasing pupil sizes, the influence of aberrations is more remarkable.

3.5 Measurements of Aberrations

The field of aberrometry is rapidly evolving. As mentioned before on one side there is the desire of the clinical community to improve visual function by improving retinal image quality and minimizing aberrations to achieve this goal. On the other side, we should consider the interest and dedication showed by members of the vision sciences community to improve the performance of the aberrometers to achieve much better system that measure with even higher accuracy.

Throughout this section, I will analyze the different techniques historically and currently used to measure aberrations. For an exhaustive study of the wavefront technology ref Charman [2005b] provides a good review

The first distinction that should be made is the placement of the image that will be analyzed by our "generic aberrometer" to evaluate the retinal image quality.

Some instruments the retinal image is re-imaged our of the eye for a further analysis this is known as "retinal imaging aberrometry" as named in McRae et al. [2001]. In contrast, there are instruments that deliver a narrow light beam into the eye and trace the rays from the retina out of the eye, this technique being known as "outgoing optics aberrometry".

Another distinction worth considering is the influence of the subject on the measurement. In all cases except one, the technique is objective, i.e. the subject is not judging the image, whereas in subjective techniques, the goodness or badness of the image, i.e. the quality of the retinal image is evaluated by subject being measured.

A third distinction of system features is the mode of measurement, which can be simultaneous, i.e. the entire wave aberration is evaluated at the same time, or sequential i.e. the evaluation of the wavefront is computed by adding together the information obtained measuring different pupil locations at different time.

Laser Ray Tracing (LRT) The first description of this technique is provided in Navarro and Losada [1997]. The LRT technique is based on direct measurements of ray deviations on the retina, or so-called "into the eye" . In this technique, narrow beams are sent into the eye, entering at different locations on the pupil in sequence. To measure different pupil locations a mirror or a combination of two mirrors is used to drive the light beam to a new position. For each pupil location, the ray coming from the retina is re-imaged back through the pupil onto a charged coupled device (CCD) array. A schematic representation of this kind of aberrometer can be seen in 3.21.

These images are then compared with a reference beam that is focused onto the retina. The result of these measurements is an array of spots (PSF) that can be used to estimate the aberrations analyzing the deviation of the centroids associated with each measurement respect to the reference beam. The distance between the focus of the reference and aberrated beams corresponds to the tilt of the wavefront in that part of the pupil.

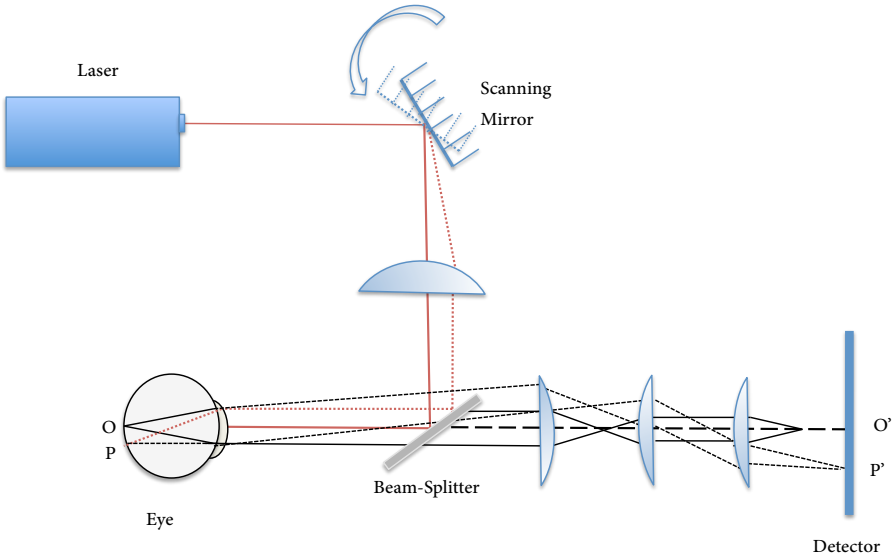

FIGURE 3.21 – Schematic representation of a classical configuration of laser ray tracing aberrometer.

3.5.1 Description of different types of Aberrometers

Tscherning Aberrometer and its variation the Howland aberroscope The Tscherning aberroscope was proposed by M. Tscherning in 1894 as a subjective method for measuring the aberrations of the human eye. We can consider this technique as belonging to "into the eye" aberrometry; the image produced in the retina is re-imaged out of the eye in order to analyze it. The eye is illuminated by a point source and this beam will focus, after going through the aberrometer lens, at a point in front of the retina. By doing so, the retina is illuminated with a disc of light since the beam is diverging after this point. The spot mask pattern produces a shadow onto the entrance pupil of the eye, finally forming an image on the retina. The subjective evaluation of the aberrations is then performed by asking the subject to report how he perceived the grid and how would he describe its deformation. The aberrations that can be measured by this system are mainly focus error, astigmatism and spherical aberration.

In the studies of Howland and B. [1977] and Howland and Howland [1976] a modified Tscherning aberroscope was designed, in which the grid was preceded and followed by a pair of $5D$ lenses. This modification produce an enhancement

of the retinal image making it sharper and easier to describe by the subject.

The limitations of these techniques are obvious as they highly depend on the ability of the subject to describe and draw the grid.

As shown in the Figure 3.22 a modern version of the Tscherning Aberroscope developed by Mierdel et al. [2001] including a beamsplitter between the eye and the aberroscope in order to capture the image of the grid with a camera making the analysis easier to interpret. If the optical power of the aberrometer lens is increased, it is possible to measure much higher aberrations. Transverse aberrations are determined by comparing the image positions with those of a reference schematic eye, which might induce some image scale errors because a real eye will have a different image size compared to the paraxial image size in a schematic eye.

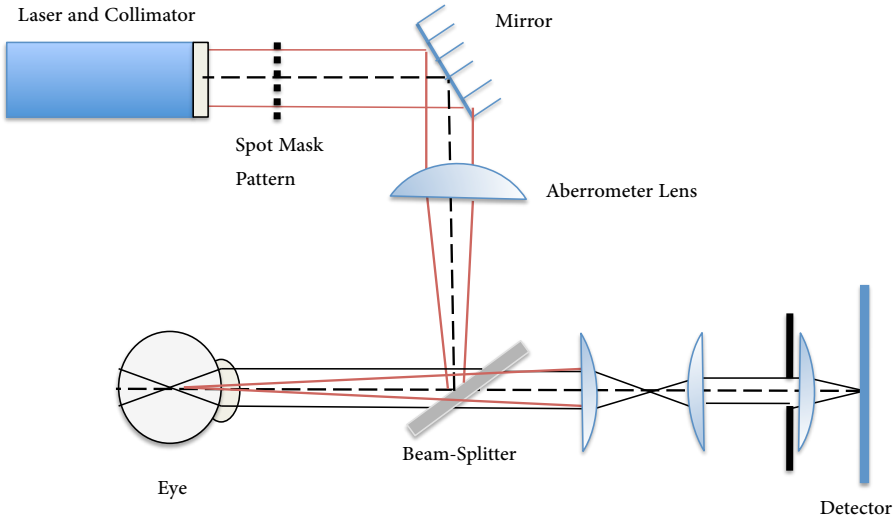

FIGURE 3.22 – Schematic representation of a classical configuration of Tscherning aberroscope.

Sequential retinoscopy Retinoscopy was used first time by Cuignet as a refraction technique to evaluate the presence of ammetropias (e.g myopia, hyperopia or astigmatism). By adding a set of trial lenses it is also possible to quantify them.

The Figure 3.23 will clarify the mechanism of retinoscopy.

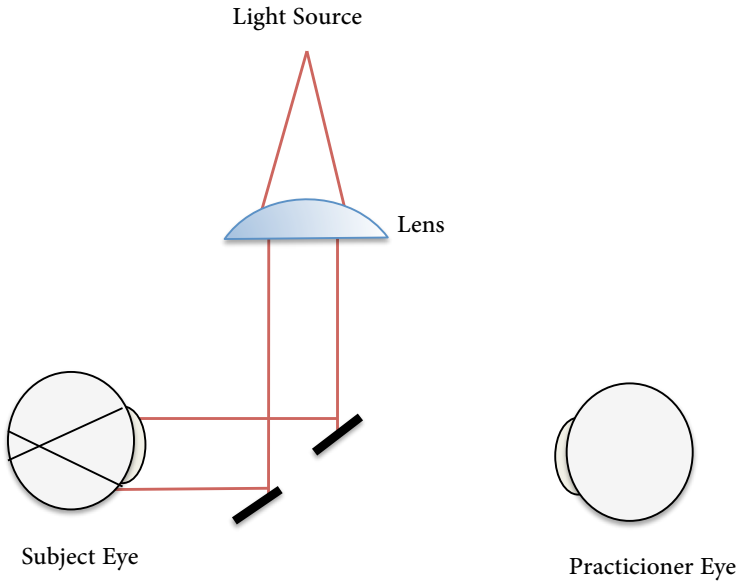

FIGURE 3.23 – Illustration of the retinoscopy mechanism

A narrow beam coming from the light source is imaged by a lens to give a divergent beam that scans the subject's retina.

The practitioner observes the shape and movement of the so called reex coming from the subject's retina and by analyzing the movement, the ametropia can be classified.

In the case of sequential retinoscopy, an infrared beam is directed into the eye, scanning the retina both radially and angularly the retina. Figure 3.24, a detailed description of the ray-path is given.

To scan the retina radially, a chopper drum is used, which allows the retina angularly by rotating the beam and drum Hieda [2003], McRae et al. [2001], McRae et al. [2004].

In a myopic eye, the aperture of the system is conjugated with a point placed in front of the retina, and the retina is scanned from top to bottom. The radiation reaching the detectors passes across the cornea from bottom to top and vice versa in the case of hypermetropia. The retina will reflect some of the light, the aperture being conjugated with the retina in the case of emmetropia, and plays the same

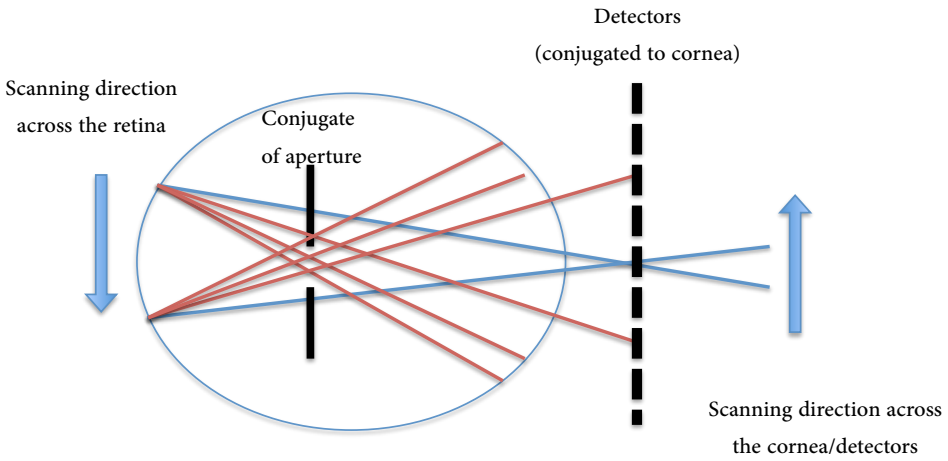

FIGURE 3.24 – Principles of sequential retinoscopy

role as the sight hole in conventional retinoscopy. The aperture will vignette the outcoming beam, which will be analyzed by an array of photodetectors placed in a plane conjugate to the cornea. This system will scan the narrow beam of light radially and angularly across the retina. The longitudinal aberrations are estimated by measuring the time delay at which the peak light intensity strikes each photodetector, compared with on-axis reference detectors. Since only sphero- cylindrical refraction may be estimated with a retinoscope, the method is limited to low order aberration measurements only.

Pyramid Sensor The pyramid (or prism) sensor was rst proposed by Ragazzoni [1996] as a wavefront sensor for astronomical applications.

The set-up is shown in Figure 3.25. The pupil of the eye is imaged onto the vertex of a four faceted pyramid with its vertex placed in the focal plane of the imaging lens. The blur spot is divided up between the four faces, and the beam will be split into four parts that is re-imaged onto an image detector, which is divided into 4 sub-pupils.

In the case of a non aberrated wavefront, the intensity on each of the four parts is the same. In the case of a distorted wavefront, the difference in intensity is non-zero in the sub-pupils. The reconstruction of the wavefront is made by measuring the differences in intensity pixel-by-pixel. It has recently been reported that the

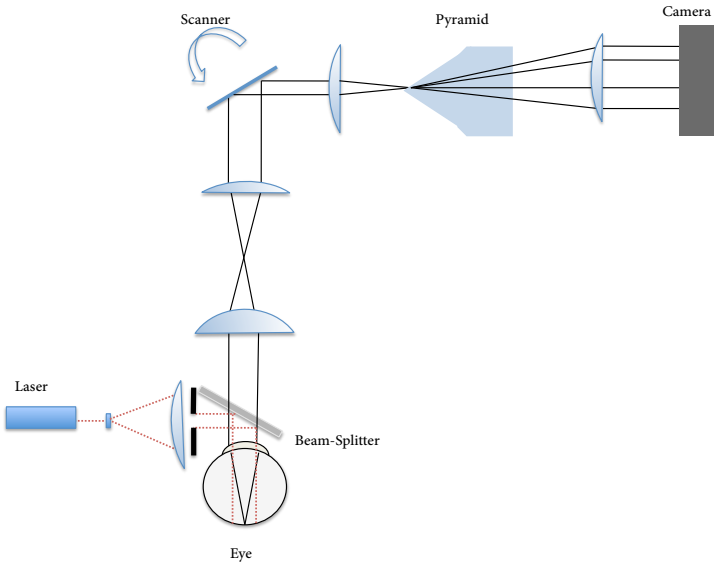

FIGURE 3.25 – Schematic representation of Pyramid sensor

pyramid wavefront sensor is a versatile instrument, and can be used to measure aberrations at the level of $0.1\mu m$ RMS Daly and Dainty [2010].

Spatially resolved refractometer The spatially resolved refractometer (SRR), was first introduced by Webb et al. [1992]. This technique is mainly subjective and can be used to measure transverse aberrations. In a commercial application, it consist of two narrow beams of visible light. A reference beam is sent to a reference part of the pupil, usually its center. A second light ray, known as the test source, is a moveable one and is delivered onto the eye at the same time but entering at a different pupil location.

If no aberration is present, the subject sees the two rays aligned, whereas when the second beam is aberrated, the subject needs to make some adjustments to align the two beams. (see Figure 3.26).

For each location of the movable source, the subject is asked to look at a target (similar to the laser ray-tracing method) and then the subject has to adjust the moveable light on the retina to align it with the reference spot on his own retina. For that purpose, there is a manipulator linked with an adjustable mirror. The same task is repeated at different locations of the movable source in the pupil

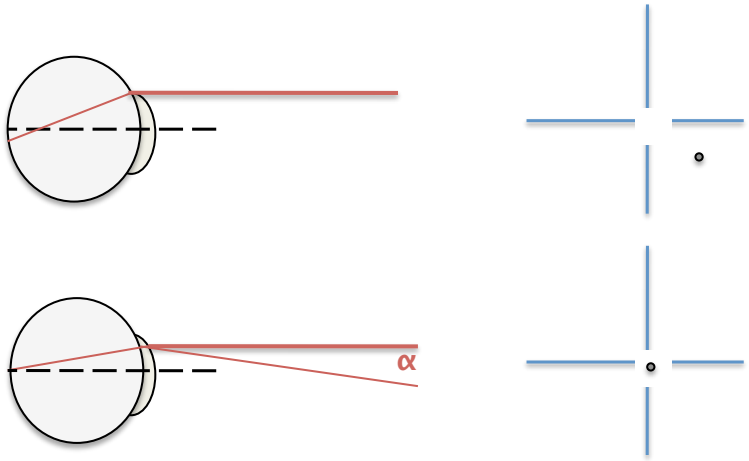

FIGURE 3.26 – Principles of spacial resolved refractometer

plane, and for each locus, the incident beam has to be realigned by the subject. The local wavefront tilt can then be derived from the incident beam- position correction. The movements that are necessary to achieve the apparent alignment are the measurement of transverse aberration present. Transverse aberration may be converted into longitudinal aberrations (LA). This technique is limited by the ability of the subject to align the beam, and is by far the most time consuming. A more detailed explanation of this technique can be found in Burn and Marcos [2001].

Curvature Sensor This sensor was developed by Roddier [1988]. The principal aim was to measure the curvature of the wavefront instead of the slope. The laplacian of the wavefront, together with wavefront tilts at the aperture edge, are measured, providing data to solve the Poisson equation to reconstruct the wavefront.

The principle of this sensor is illustrated in Figure 3.27. The curvature sensor consists of two image detectors placed out of focus. Irradiance distributions are measured in two out-of-focus planes. In one of the planes, placed at P_1 at a distance of l from the field lens, there will be an excess of illumination and in the other detector placed at P_2 , also placed at a distance of l from the field lens, there will be a lack of it; the calculation of the normalized difference of illuminance

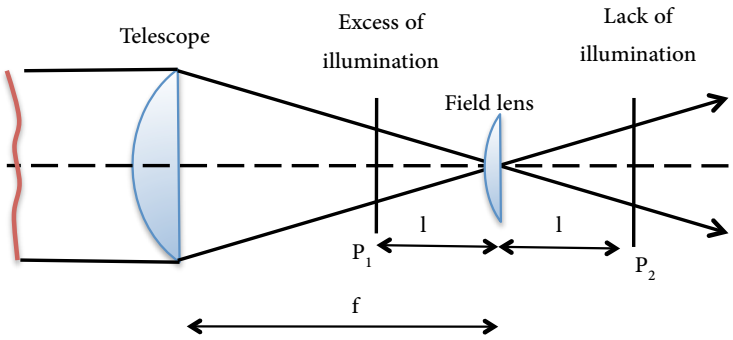

FIGURE 3.27 – Principle of curvature sensor

between these two planes determines the curvature and estimates the aberrations. The field lens is used for symmetry in order to reimage the pupil. The setup proposed by Roddier uses a variable curvature mirror placed at the focal plane of the telescope of the field lens. Which allows the reimaging on the detector of both array the inside ad outside focus blurred pupil images by its concave or convex deformation.The curvature signals are recovered by synchronous detection. The pixels inside the beam give the local curvatures, the pixels of the edge of the beam at local wavefront slopes. The big advantage of this wavefront sensor is its quantum efficiency and the fact that only two detectors are needed.

3.5.2 Hartmann Shack Wavefront Sensor

Originally, this kind of sensor was developed to measure the aberrations produced by the atmosphere, and the main goal was to improve the optical quality of satellite images taking by telescopes placed on earth. The design of this sensor was first proposed by Hartmann in 1900 and built by Shack and Platt in 1971 Platt and Shack [2001]. In the mid 1980s, Dr. Josef Bille, from the University of Erlangen-Nurnberg, started working with Dr. Roland Shack to use the lens array for measuring the profile of the cornea. Bille was the first to use the sensor in ophthalmology, and having used it initially to measure the profile of the cornea, he later measured aberrations in the eye, by projecting a point source onto the retina. The aim of the Hartmann-Shack sensor is to measure the shape of the wavefront, and it is probably the sensor most commonly used in the field of Adaptive Optics.

Many papers have been published on this topic and its efficiency and reliability. The first application of the HSWFS in the human eye was made by Liang et al. [1994]. The principles are quite simple; a narrow beam from a point source is imaged on the eye and the light coming back from the fundus is imaged by the HS sensor. This sensor is an array of microlenses with focal length, f, placed in the plane conjugated to the pupil of the eye.

Each of these lenslets samples the local gradient of the wavefront, and from them, it is possible to reconstruct the complete wavefront. The slopes of the wavefront are the first derivative and are represented by $\partial W(x, y)$; the factors $\triangle x$ and $\triangle y$ represent the displacement of the spots in the respective x and y directions.

$$\frac{\partial W(x,y)}{\partial x} = \frac{\triangle x_s}{F} \tag{3.31}$$

$$\frac{\partial W(x,y)}{\partial y} = \frac{\triangle y_s}{F} \tag{3.32}$$

If we are imaging a perfect non aberrated eye on the detector of the sensor (placed at the focal plane of the microlenses) we will have a perfect arrangement of spots and no displacement will exist. See Figure 3.28.

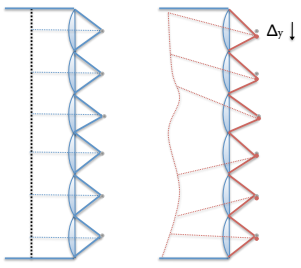

FIGURE 3.28 – Schematic representation of the Hartman Shack principle on the lenslet array

If on the contrary aberrations are present, the spots produced will be displaced from their unaberrated position.

The displacement of each spot is proportional to the wavefront slope at the location In the Figure 3.29, we can see in detail a schema of this kind of aber-

rometer.

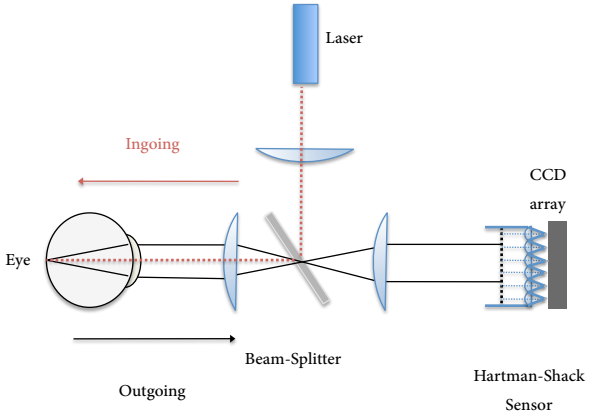

FIGURE 3.29 – Schematic representation of the Hartman Shack principle

The SH sensor can be used as part of an adaptive optics system to monitor and correct aberrations in the eye Liang and Williams [1997], and may even be adapted to measure scatter in the eye Donnelly et al. [2004].

Chapter 4

Aberrations of the human eye

4.1 Abstract

Chapter 2 provided general overview of human eye anatomy, investigating image formation and the sources of aberration in the human eye. **Chapter 3** presented the essential background on wavefront aberrations and its mathematical definition, a brief study of aberration theory and ways of evaluating retinal image quality.

In this chapter, the different ocular aberrations will be measured, not only for central vision but specifically for the peripheral visual field. For that purpose, a HSWFS was developed and the process will be described in detail in Figure 4.1. We measured high order aberrations up to the 5th degree comprising 18 terms, including both lower and high order aberrations, for central vision as well as at ten different locations in the peripheral visual field. We found, as reported in the literature, that the retinal image quality decreases dramatically for non-perifoveal locations and the contribution of oblique astigmatism is very large for off axis locations.

4.2 Literature Review

4.2.1 On Axis aberrations

The study of aberrations in the human eye is nothing new. Helmholtz was able to establish that the optical quality of the human eye was far from perfect as an optical system, and in recent years, with the advent of new technology, optical studies of the eye have become more popular and comprehensive. The advances in this field in the last 50 years have been enormous, from a procedure used only in

research laboratories to a widely used technique in everyday clinic assessments. Past studies, such as that of Howland and B. [1977] estimated the influence of HOA using a subjective system. Walsh et al. [1984] , Howland and Howland [1976], and Howland [2002] all provide more detailed results from which we can extrapolate useful information as to the large variability in the values of HOA amongst individuals.

The measurement and analysis of the distribution of ocular aberrations for foveal vision by means of HS has been studied in depth over the last 25 years, starting with the classical study of Liang and Williams [1997], and Liang et al. [1994] and then moving to large population studies of healthy eyes as such as those of Porter et al. [2001] , Plainis and Pallikaris [2008] and Castejon-Mochon et al. [2002]. A very important study is that of Thibos et al. [2002], who found that the population averages of Zernike coefficients were nearly zero for all of the higher-order modes except spherical aberration. This result indicates that a hypothetical average eye representing the central tendency of the population is nearly free of aberrations, suggesting the possible influence of an emmetropization process or evolutionary pressure for corrected optical performance in the human eye. Some studies have been performed to investigate the impact of age on the distribution of the aberrations (Atchison and E.L. [2008] and Radhakrishnan and Charman [2007].)

The accommodative state is also an important variable to take into account since the aberrations and their relative weight change with accommodation Berrio et al. [2010] and Atchison et al. [1995]. The impact of the correction of those aberrations on the accommodative response is a very interesting topic explored in detail by Fernandez and Artal [2001]

The main effect of the ocular aberrations on the human eye is the degradation of the retinal image and can be quantified by the enlargement of the PSF. This effect can be defined as a purely optical effect, but the presence of a high amount of aberrations has other non-desirable effects, such as a decrease in contrast sensitivity capabilities Zang et al. [1997] and difficulties in detecting borders. The previously mentioned effects become more acute for peripheral vision since the limitations are not only optical but also neural as the detection and resolution thresholds are affected by aliasing, as previously mentioned by Thibos et al. [1987]

and Thibos et al. [1996].

Ocular aberrations are not static but change as result of several factors, for example as the eye ages Berrio et al. [2010] and Radhakrishnan and Charman [2007]. Very recently, the multifractal dimension of the dynamics of ocular aberrations has been examined Hampson and Mallen [2011] as well as the correlation between optical quality of both eyes Chin et al. [2008]. This dynamic nature of the ocular aberrations is of interest to explore if our ultimate aim is to compensate for these aberrations.

The impact of ocular aberrations is not the same for emmetropic eyes as it could be for myopic or hyperopic eyes because the relative distribution of all the Zernike terms differs depending upon the refractive state of the subject, (see Charman [2005a] , Buehren and Collins [2005] and Rossi et al. [2007] and Charman [2005a]).

Despite everything mentioned above, the human eye, as a whole, is a robust optical system; we must take into account not only the optics of the human eye but also retinal processing and the existence of several neural mechanisms that compensate the HOA to achieve a better performance, as mentioned in Artal et al. [2006] and Tabernero et al. [2007].

4.2.2 Off Axis aberrations

More recently, attention has shifted towards the study of the importance and impact of aberrations in peripheral vision. As mentioned before and widely studied in the past, the resolution achieved in the peripheral visual field is much poorer than along the visual axis or line of sight. However, the functional significance of the peripheral visual field is not negligible, as it is clearly very important for the detection of movement and orientation tasks.

Several studies have measured ocular peripheral aberrations by using different techniques, as already mentioned in Chapter 3. The most remarkable finding of those studies is the major impact on the total RMS of the eye made by lower order aberrations such as myopia and astigmatism.

The technique used to measure the aberrations include retinoscopy Millodot and A. [1974] and Rempt et al. [1971] and Wang et al. [1996] and manual op-

tometers Ferre et al. [1932] and Ferre [1931]. More recently, there have been several studies using double pass techniques Jennings et al. [1980], Artal et al. [1995] , Guirao and Artal [1999], Gustafsson et al. [2001], Navarro et al. [1998] and Williams et al. [1996], and others computed the MTF function along the visual field using aerial images Navarro et al. [1993] by means of double pass to estimate the image quality of the eye across a wide visual field of 120°. The investigations of Lundstrom (Lundstrom [2007], Lundstrom et al. [2007] , Lundstrom et al. [2005a] and Lundstrom et al. [2009a]) give a more in depth insight into the whole phenomenon of peripheral ocular aberrations as well as providing a very useful comparison between techniques including the use of photorefraction.The peripheral aberrations have been measured by means of autorefractometers Atchison [2005] and Mathur et al. [2008].

The first study found in the literature that analyzes the impact of the HOA is that of Navarro et al. [1998], who used LRT to measure the aberrations and described the aberrations by means of Zernike polynomials. Later studies by Atchison and Scott [2002] used HSWFS to measure peripheral aberrations and showed the large effect of the third order aberrations on the total value of the RMS, whereas the higher order aberrations have less impact, as shown by Lundstrom et al. [2005a] and Sheenan et al. [2007]. Thus, RMS is primarily influenced made by the lower order aberrations, defocus and astigmatism.

The aberrations off-axis are influenced by aging of the eye, as studied by Mathur et al. [2010], who found that total root-mean-square and higher-order aberrations increased more rapidly with field angle in older emmetropes. Another study, Charman and Jennings [2005], found that the central refraction shifted in the expected hyperopic direction, while the radial and tangential image elds in the periphery became more myopic. The reported loss with age in peripheral visual performance does not seem to be attributable to markedly increased peripheral astigmatism. Therefore, it is unlikely that peripheral visual performance deficits observed in normal older individuals are primarily attributable to the increased impact of higher-order aberration, and under normal conditions, the relative importance of the increased higher-order aberrations in older eyes is lessened by the reduction in pupil diameter with age (i.e. senile miosis).

The distribution of aberrations, depending on refractive state of the subject,

is also important Seidelmann et al. [2002] and Lundstrom et al. [2011]; at 45 deg eccentricity, the double-pass technique revealed relatively more hyperopic sphere in myopic subjects than in emmetropic subjects and more myopic sphere equivalents in hyperopic subjects.

As mentioned above, the accommodative state is also an important variable to take into account since the aberrations, and the relative weight of them, change with accommodation, but in the case of peripheral aberrations, the changes are not as important in adults. For most of the adult emmetropes studied, any changes with accommodation and aberration were small, as described in Mathur et al. [2009] and Lundstrom et al. [2009b].

It is also important to know the relative influence of the cornea and lens on peripheral aberrations. Atchison [2004] described that, in general, the anterior corneal aberration components were considerably higher than the overall aberrations across the visual field and were balanced to a considerable degree by the internal ocular aberration components. Both components and overall Zernike aberrations were greater for the nasal than for the temporal visual field.

4.3 Experimental Design

To characterize any optical system, as in this study of the human eye, **wave aberration** will be used. As mentioned before in detail, if we evaluate the image produced by a perfect eye, it should only be limited by the diffraction pattern. In real eyes, however, the image is not a perfect point, but is distorted due to several aberrations, which can be detected in the shape of the exiting wavefront. As previously discussed, the cornea and the lens each contribute in a different way to the total aberrations of the eye Artal and Guirao [1998]. However, in this study, we will concentrate on measurements of the complete wavefront of the human eye for several peripheral locations.

Considering the different techniques used to measure the shape of a wavefront, as discussed in the preceding chapter, wavefront sensors can be classified by whether the measurements are based on objective or subjective methods and if the wavefront sensor measures the light coming into the eye or coming out of the eye.

HSWFS was chosen for this study because of the specific advantages, i.e. the simplicity and the ability to make fast and precise measurements of the ocular aberrations. One of the sources for the theoretical analysis HS in the human eye is the work of Prieto and Vargas-Martin [2000].

We measured the aberrations at the School of Optometry and Vision Sciences in Cardiff University. The system used for that purpose, designed and built by the author, was assembled on an optical table, and comprised a detection channel and a pupil tracking channel. The final configuration of the sensor is shown in Figure 4.1.

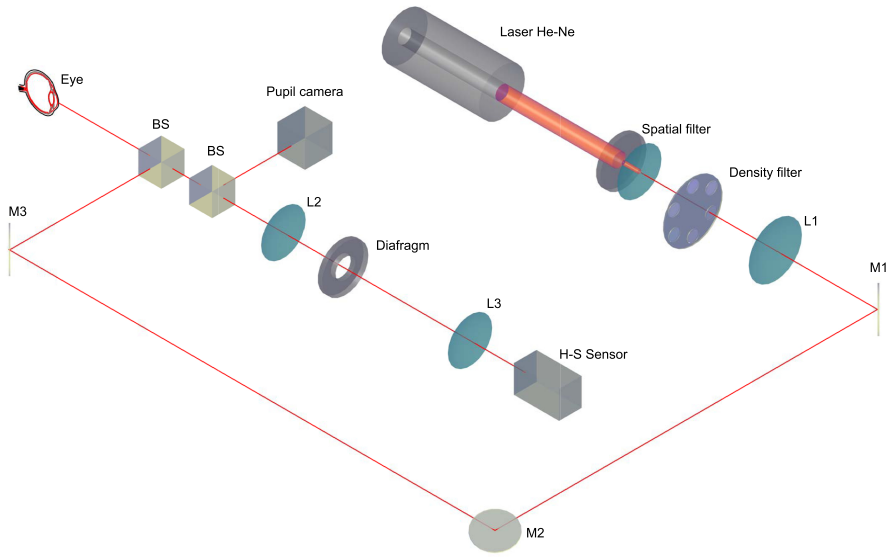

FIGURE 4.1 – Schematic diagram of the HS set-up used to measure wavefronts in this work, collimated rays coming from the He-Ne source are spatially filtered and driven onto the eye, the reflected beam is focused on the HS sensor bye mean of L2 and L3. Notation: L1- focusing lens, L2-3 telescope, BS-beam splitter,M1,M2 ,M3 being plane mirrors

An overview of the instrument follows .

4.3.1 Sensing Channel

In the sensing channel, the laser source emitting a wavelength of 633μm is firstly spatially filtered and then dimmed by means of a neutral density filter, producing a collimated narrow beam entering into the eye. The diameter of the laser beam is around 1 mm, and the power level does not exceed 0.8 μW.

The light is then reflected from the surface of the retina, and it emerges from the eye to be captured by the sensor itself, in this case a Hamamatsu camera consisting of an array of microlenses and a CCD camera. The microlenses sampling the emerging beam were in a quadrangular pattern, and they were placed on the conjugated plane of the eye pupil. Each lenslet was 0.3 mm x 0.3 mm over the eye pupil and had a 7.21-mm focal length. The CCD camera was placed on the focal plane of the lenslet array and conjugated with the retina, to record the HSWFS spot pattern. As explained above, the local slopes of the wave aberration measured by the HSWFS sensor are proportional to the wavefront error. The aberrated wavefront is reconstructed using modal reconstruction to obtain the Zernike coefficients, and the reconstruction of the aberrated wavefront is achieved by using the Zernike polynomials.

The experimental set-up used for this study comprised the following components:

- **Laser**: The light-source used was a conventional Helium-Neon laser. It emitted coherent, collimated and monochromatic light with a power of (1 mW) and a wavelength of 633 nm, which corresponds to red light. The laser was Class 3a (see Appendix .1).

- **Spatial Filter**: A microscope objective was used to focus the laser light, and a convex lens was used to broaden the beam exiting from the source. Then there was a pinhole of 10 microns diameter placed at the focal plane of the microscope objective, and the light was focused through the pinhole to ensure a diffraction-limited point source.

  Density Filter: A neutral density filter was introduced to better control the amount of light reaching into the eye, and this filter was used to reduce the intensity of the beam since only a very small and narrow beam is needed

to perform the measurements.

L1: An achromatic lens with a power of (+4.5 D) and a diameter of 50mm was placed with its back-focal-point in the pinhole, in order to get a collimated (almost parallel) beam out. The focal length of the lens was chosen to be short to get a small f-number (f/ = focal length / diameter of aperture). The smaller the f-number, the more light comes through the lens.

Optical elements

In Figure 4.1, **M1**, **M2** and **M3** reflect the beam to the right position. The elements, **BS1** and **BS2** are beam splitters that divide the beam into two parts, one of which is reflected and the other is transmitted. From **B1**, part of the beam will be directed into the eye, and once it reaches the retina, will be reflected to reach the HSWFS sensor. The remaining light will once again be split into two parts, one directed to the pupil camera and the rest transmitted to the HSWFS sensor.

- The detector **HS**: The Hartmann-Shack sensor used consists of a lenslet array developed by Hamamatsu, with quadrangular lenses (0.3 x 0.3mm). That form a circle. The focal length of the microlenses is approximately 7.21 mm. **CCD**: A CCD-camera (Charge Coupled Device-camera) is placed behind the lens array at a distance of one micro-lens focal length (7.21 mm).

4.3.2 Pupil positioning channel

The **Pupil Camera** is a CCD camera conjugated with the pupil plane and gives information about the correct positioning of the eye during the measurements. The pupil of the subject will be seen correctly focused in the pupil camera only when the pupil is also conjugated with the H-S sensor. **L2** and **L3** are a telescope that conjugates the pupil plane of the subject with the entry pupil of the H-S sensor. This pupil camera, in combination with a bite bar, and having a fixation target, assured the correct positioning of the eye, during the measurements.

4.3.3 Calibration and repeatability of the HSWFS

Before the experiment was carried out, an additional method of validation was used. The ocular aberrations of an artificial eye were measured, for a common pupil size of 5 mm. The artificial eye was made of a convergent lens and a moveable "retina" that allowed a simulation of different levels of ametropia. Since the primary aim of the project was to measure low order aberrations of the pigeon eye in the peripheral visual field (see Chapter 5), we also simulated the defocus produced by adding trial lenses in front of the artificial eye, and the results are shown in the Figure 4.2.

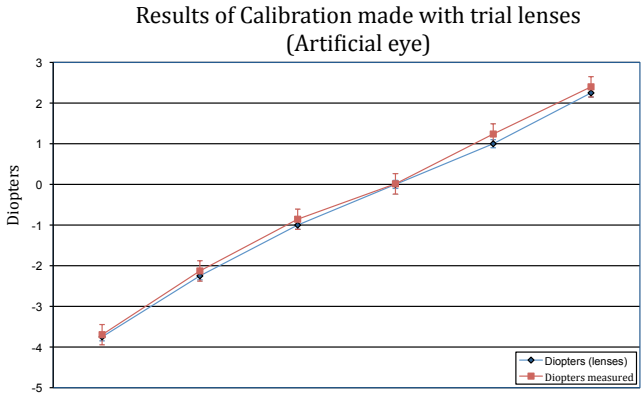

FIGURE 4.2 – Results of the calibration of the system, by adding trial lenses in front of artificial eye.

The results presented on Figure 4.2 present a good agreement between the power of the trial lens measured and the power calculated based on the corresponding Zernike coefficients for lower aberrations, the calculation was performed for a common pupil size of 5 mm. It is worth remarking that the agreement becomes less accurate as we increase the power of the trial lenses since the process involved by adding more lenses.

It is very important to study and isolate any possible systematic error, whilst measuring ocular aberration, in real subjects.There are normal fluctuations of common parameters such as IOP and accommodation status. As mentioned in

previous sections, the nature of the ocular aberrations is dynamic. By taking into account the dynamic of the ocular aberrations while neglecting the possible effect of the changes related to blood pressure and tear film evolution, we could identify any possible systematic error in the measuring procedure. Therefore, a series of measurements was taken for the same subject on different days to demonstrate the correct realignment.

Another possible source of errors could be any head movement during the measurement, and this was controlled for by the pupil camera and the bite bar. A bite bar was made for each subject prior to the measurement using a bi-phasic material commonly used in dentistry. This bar kept the shape of the subject's bitting pattern and was placed on the optical table, so that the subject was at the right distance to ensure pupil conjugation.

The repeatability of any sensing system can be defined as the variation of the measurement obtained by the system for the same subject measured under the same experimental conditions. In order to evaluate the repeatability of our instrument, we measured the right eye of a subject natural conditions. The subject was asked to xate her eye on the central point of the fixation target and a measurement was taken. Then the subject was asked to reposition him or herself and bite the bar again and another measurement was taken, to make a total of 5 during each session over a total of three sessions. The results are shown in Figure 4.3. After each measurement, the subject was realigned and the procedure was repeated until reaching a total of 20 measurements.

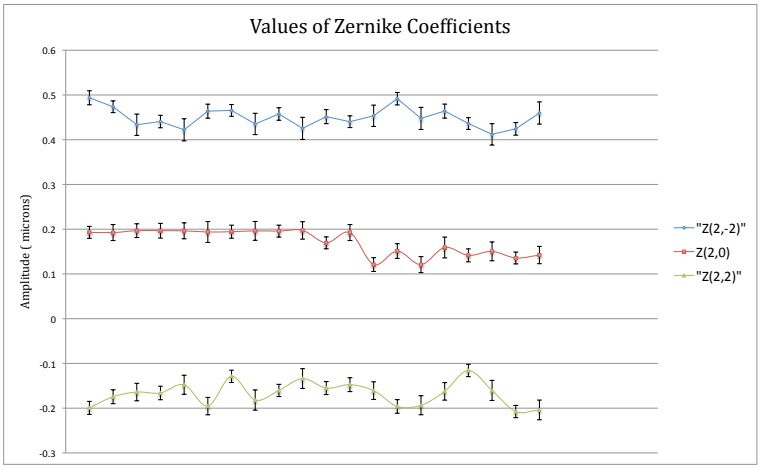

FIGURE 4.3 – Repeatability test on the HS aberrometer. Amplitude in microns measured over 20 single measurements of one subject after successive realignment.

Figure 4.3 shows the fluctuation of the Zernike coefficients over 20 single measurements, each measurement comprises three measurements and the error bars correspond to standard deviation.

The three Zernike coefficients corresponding to low order aberrations fluctuate in amplitude, the astigmatism coefficients Z_2^2 and Z_{-2}^2 both oscillate around 0.15μm, and the coefficient corresponding to defocus Z_0^2 oscillate less than 0.1μm.

4.3.4 Data Processing

In this study, all the slopes were fitted using a modal reconstruction up to the 5th degree (18 terms). This adjustment was accomplished by means of the program, CAMWIN, which was developed at LOUM Universidad de Murcia, and one of its characteristic input interfaces is shown in the Figure 4.4.

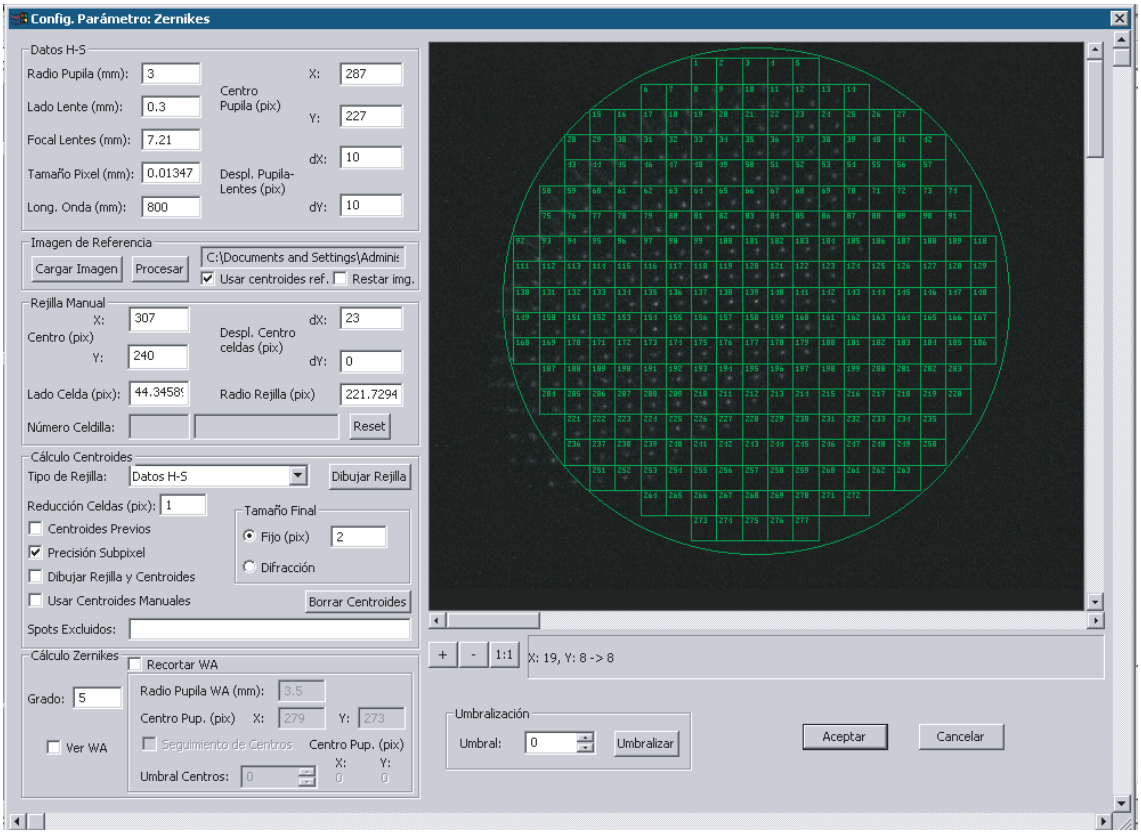

FIGURE 4.4 – Representation of the configuration screen on CAMWIN

The software reproduces the wavefront of each of the measurements and a simulation of the PSF (Point Spread Function) corresponding to this wavefront (See Figure 4.5). When using CAMWIN, we can reconstruct the wavefront only in black and white. Figure 4.6 shows a reconstructed wavefront averaged from the twenty measurements at each eccentricity. This figure corresponds to subject CT on the temporal side for OD.

To provide comprehensive information about the shape of the aberrated wavefront, a MATLAB code was developed to average up to twenty measurements. In this way, the mean of all the measurements taken for the same eye for each position can be derived. Another advantage of this reconstruction of the wavefront made with MATLAB is the possibility of visualizing the wavefront representation in color using the color scale.

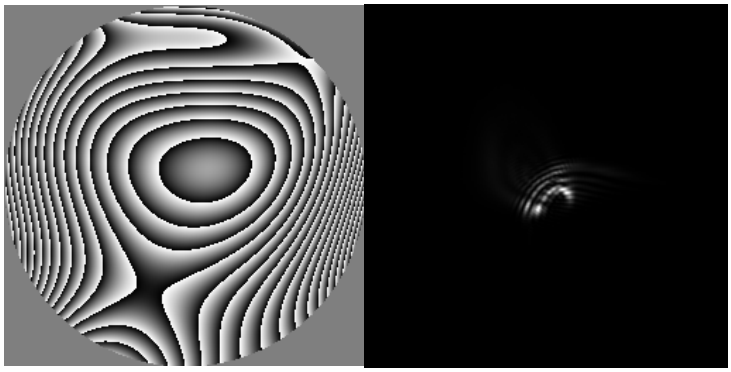

FIGURE 4.5 – Wavefront reconstructed and PSF simulation calculated by CAMWIN

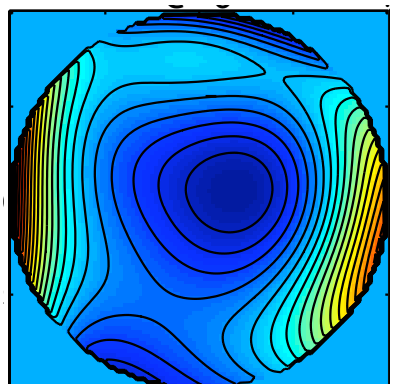

FIGURE 4.6 – Representation of the wavefront aberration reconstructed by MATLAB

4.4 Results

4.4.1 Preliminary Data

During initial phase of this study, a set of measurements was taken on three different subjects to prove the simple procedure employed. The subject was first placed in front of the instrument. In order to ensure the correct head position, a bite bar was used, which the subject was asked to bite while keeping their head still.

In the first instance, measurements were taken on axis. The subject just needed to fixate on the red beam, and the angle of eccentricity in this case is e=0°. The measurement was then taken twenty times, while subject remains still.

For measurements off-axis, different fixation targets were placed on the wall in front of the subject, and the subject needed to fixate on one of them each time. The measured angles at the retina were 7.5°, 13.4°, 20.5° and 25.4°.

Once the subject fixated on one of the targets, the reflected image was shown on the main screen of the program. The important goal was to avoid any corneal reflection during the measurements. The positioning of the targets and the subtended angles are shown in Figure 4.7.

For measurements in human eyes, 3 healthy adult subjects(see Table 4.1), either emmetropic or with only a low amount of myopia (-1 ± 0.25), were chosen. Twenty measurements were performed at each location. Each single wavefront measurement took about 40 ms, and the results provided an average of the aberrations in the eye at each position.

SubjectNumber	*Age*	*Gender*	*sphere Refraction[D]*	*Cylinder [D]*
1	28	M	planar	planar
2	20	M	-0.75	-0.50
3	18	F	-1.25	0.50

TABLE 4.1 – Refractive state of the subjects included in this study

The raw (non post-processed) measurements corresponding to an image of the

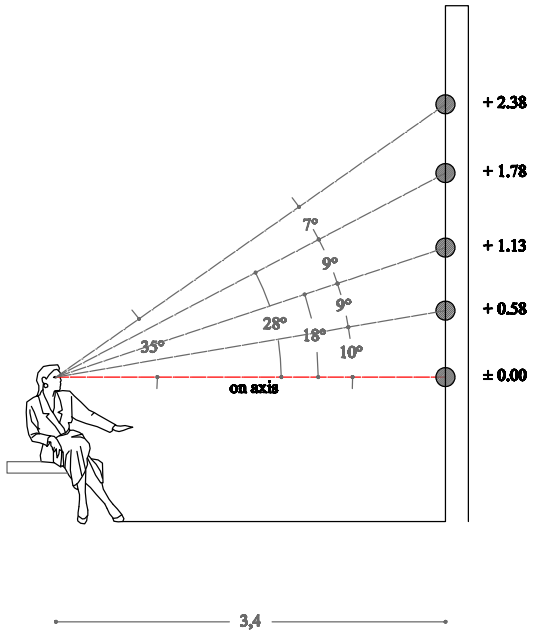

FIGURE 4.7 – Representation of the measured eccentricity angles

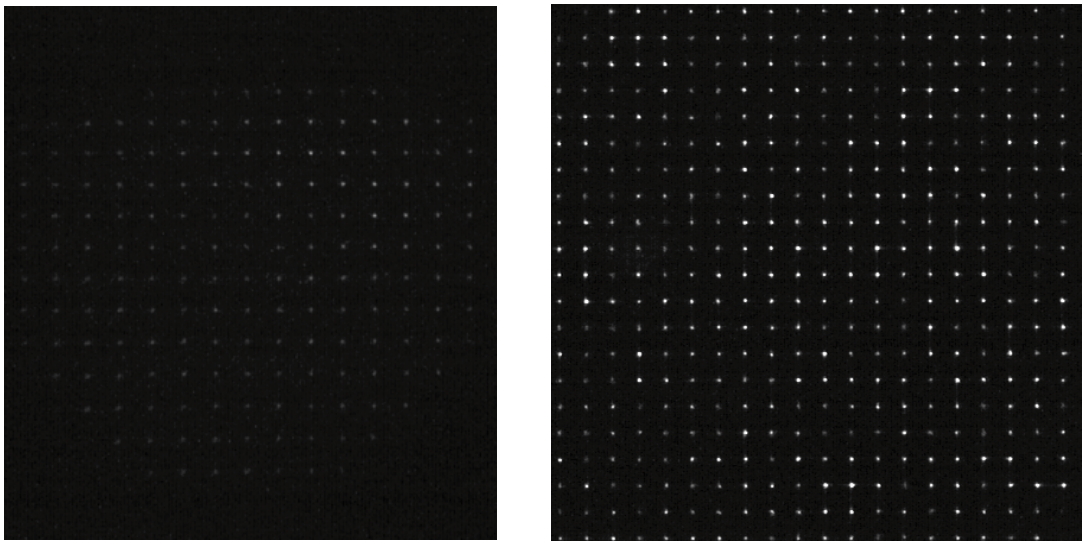

FIGURE 4.8 – Image of the raw data provided by the system for measurements on axis subject CT (left). Image of the reference wavefront(right)

aberrated wavefront produced by the lenslet array is shown in Figure 4.8. The aberrations of the subject can be calculated from this image. The image produced by each lens is displaced due to the aberrations, and the software compares the raw image with a reference image, which is taken each time before the actual wavefront measurements. An example of a reference image is shown in Figure 4.8.

The measurements in normal humans were acquired for three adult subjects (aged between 18 and 28 years). The results of the wavefront aberration are shown in Figure 4.9 . We can see the reconstructed wavefront averaged from the twenty measurements at each eccentricity.

For each set, we calculated the average value for the corresponding Zernike coefficients up to fifth order, starting with the coefficient Z_2^{-2}. Figure 4.10 depict the value of the Zernike coefficients using the standards of the OSA (Optical Society of America).

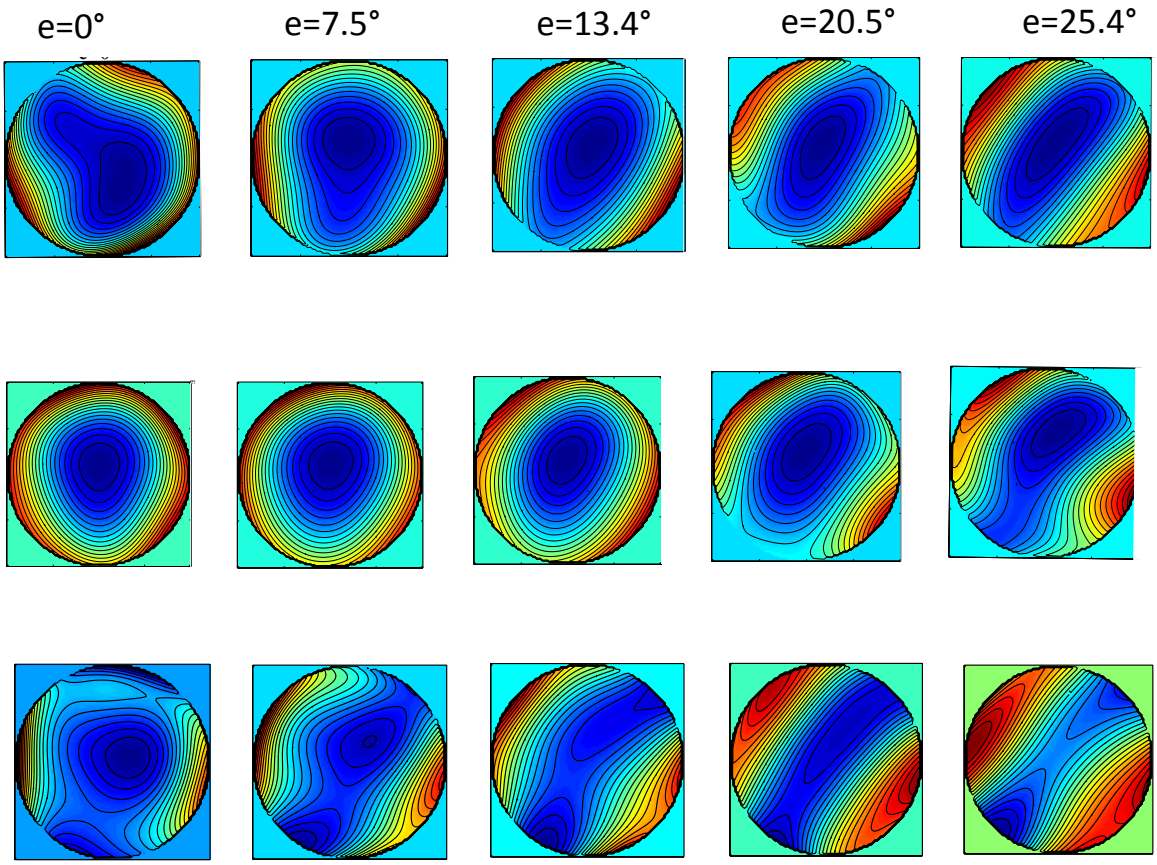

FIGURE 4.9 – Representation of the wavefront aberration for increasing eccentricities for human eye for the subjects S1, S2, S3 respectively from top to bottom, and increasing eccentricities from left to right.

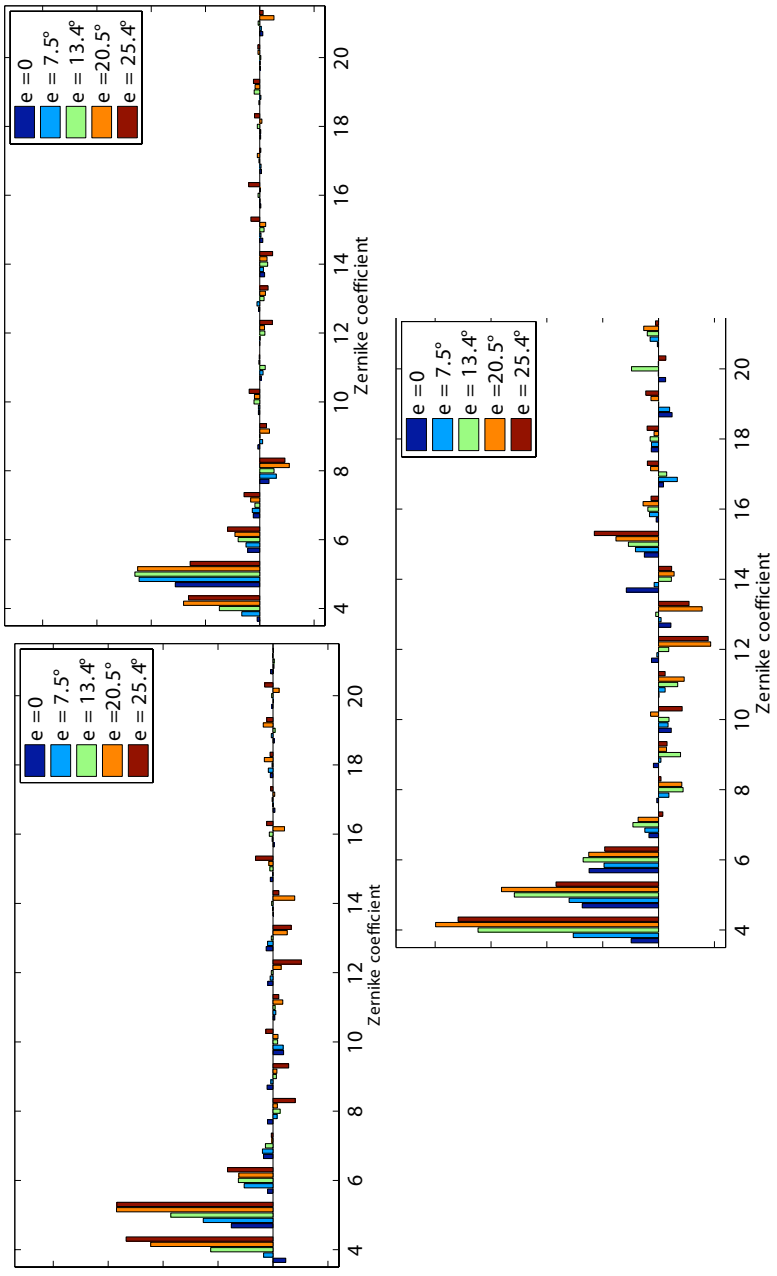

FIGURE 4.10 – Representation of the Zernike coefficients up to 5th degree, measured for different eccentricities for the subjects S1(top left) , S2 (top right), S3 (bottom). The error bars have been omitted for clarity purposes.

SubjectNumber	*Age*	*Gender*	*sphere Refraction[D]*	*Cylinder [D]*
1	23	F	-0.50	planar
2	22	M	-1.50	planar
3	25	F	planar	planar
4	27	F	-1.00	planar
5	28	M	+0.5	planar
6	26	F	-1.25	0.25
7	22	M	planar	0.25
8	20	M	-0.25	0.5
9	27	F	-1.5	0.25
10	19	M	+1.25	-0.25

TABLE 4.2 – Refractive state of the subjects included in the study (OS)

4.4.2 Emmetropic population study

For this section of the study, 10 young subjects (5 female, 5 male) were chosen with an age range between 19 and 28 and an average age of 24. All subjects were healthy with no previous eye surgery. The refractive error was chosen to be within a margin of sphere (+0.5 to -1.50D) and up to 0.25D cylinder. Prior to the measurements, the refractive state of both eyes as well as a general eye test was performed by the author at the Eye Clinic, Cardiff University. The project received written approval of the Ethical Committee of the School of Optometry and Vision Sciences.

The measurements were performed without using cycloplegic agents since we wanted to evaluate the ocular aberrations for peripheral vision under normal conditions. For that purpose, the measurements were finally performed with the lights dimmed in order to allow the pupil to dilate in each case, but the results were evaluated for a common pupil of 5mm. No spectacles or contact lenses were used, and the refractive error was not corrected. The information regarding the subjects is presented in Table 4.2.

In Figure 4.11, the values of the Zernike coefficients for the OS of ten experimental subjects and standard errors are depicted for the three measuring points located in the superior visual field.

From Figure 4.11 , we could affirm that despite the high intersubject variability a general trend can be seen, the major contributors to the total aberration

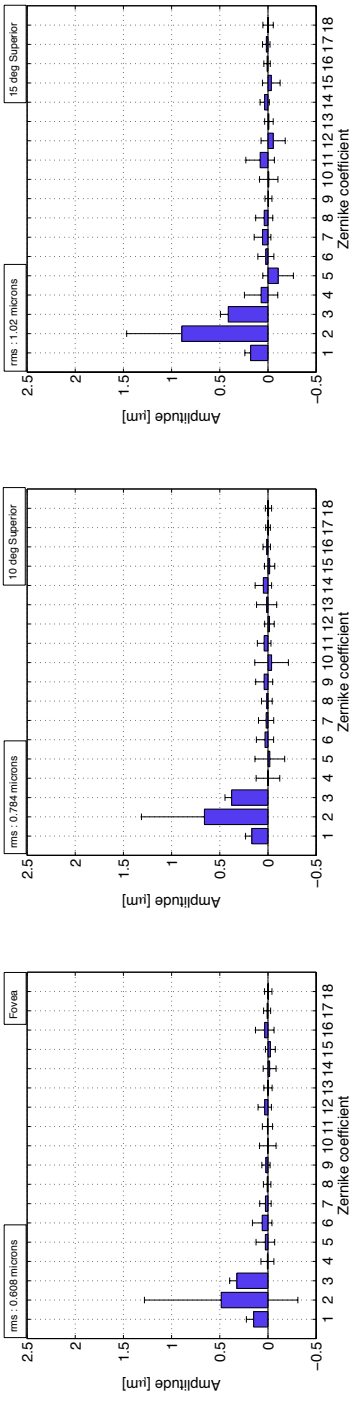

FIGURE 4.11 – Mean values of the Zernike coefficients up to 5th order for 5mm pupil diameter for superior field of view. Error bars correspond to standard deviation.

	RMS Values for Superior Field		
Zernike Coefficient	Fovea	10 deg	15d deg
	Mean ± *SD* [μm]	Mean ± *SD* [μm]	Mean ± *SD* [μm]
Total RMS	0.609 ± 0.844	1.017 ± 0.646	1.022 ± 0.655
"Z(2,0)=0"	0.367 ± 0.259	0.424 ± 0.355	0.486 ± 0.379
HOA RMS	0.094 ± 0.259	0.098 ± 0.355	0.184 ± 0.379

TABLE 4.3 – Calculated RMS values for the subjects included in the study. First row total RMS; second row, defocus has been removed; last row corresponds only to HOA.

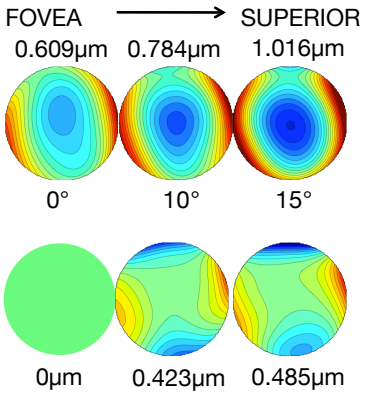

FIGURE 4.12 – Representation of the wavefront aberration for different eccentricities for human eye for the subjects included in the study; increasing eccentricities from left to right.

are both terms of astigmatism and also defocus.

A wavefront plot is presented on 4.12 where the overall shape of the WF is plotted in combination with the RMS calculated values. On second row the residual WF are depicted this approach has been used before Nowakowski [2010]. We can see that the total WF is clearly degrading as we increase the eccentricity.

In order to better understand the influence of individual aberrations, a further calculation was made in Fig 4.13, to obtain the total value of RMS in the superior visual field. It can clearly be seen that the total RMS increases as we increase the angle, as expected from the distribution of aberrations, and it is worth noticing that the 2nd order aberrations mimic the overall value of RMS. The value of both astigmatic terms increase in a linear way following a similar trend.

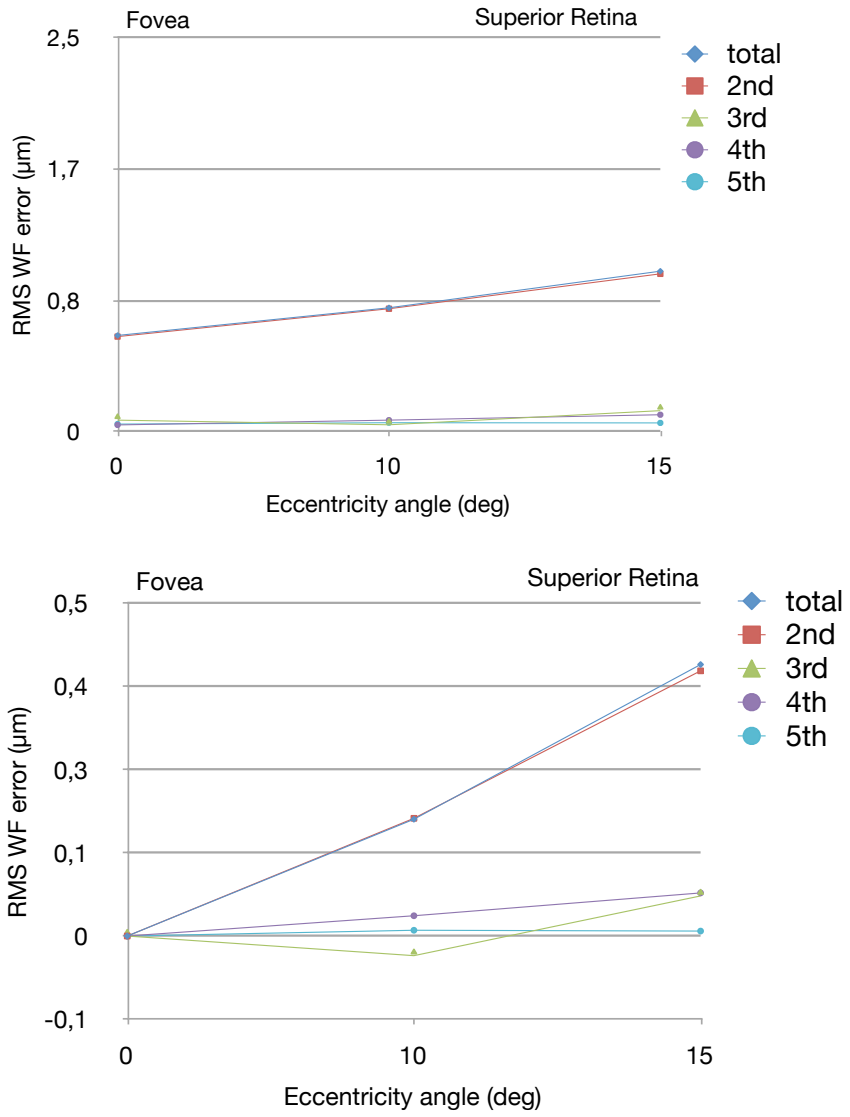

FIGURE 4.13 – RMS values in microns for 10 eyes across for superior field.The aberrations have been grouped according the order (top) . The values of the aberrations have been corrected to represent the residual aberrations once the value corresponding to foveal location have been substracted (bottom). Error bars have been omitted for clarity.

In Figure 4.14, we present the evolution of combinations of aberrations defocus Z_2^0, both components of astigmatism $((Z_2^2)^2+(Z_2^{-2})^2)^{\frac{1}{2}}$, coma $((Z_3^1)^2+(Z_3^{-1})^2)^{\frac{1}{2}}$, trefoil $((Z_3^3)^2+(Z_3^0)^{-3})^{\frac{1}{2}}$, and spherical aberration Z_4^0. This type of represen-

tation offers a better way of visualization. It has been mentioned above that the impact of lower order aberrations is very high in this representation. We can see that defocus is almost overlapping with the total value whereas astigmatism has a relatively lower impact. Spherical aberration, in contrast should not change by definition and we can see that it remains mostly constant along the field.

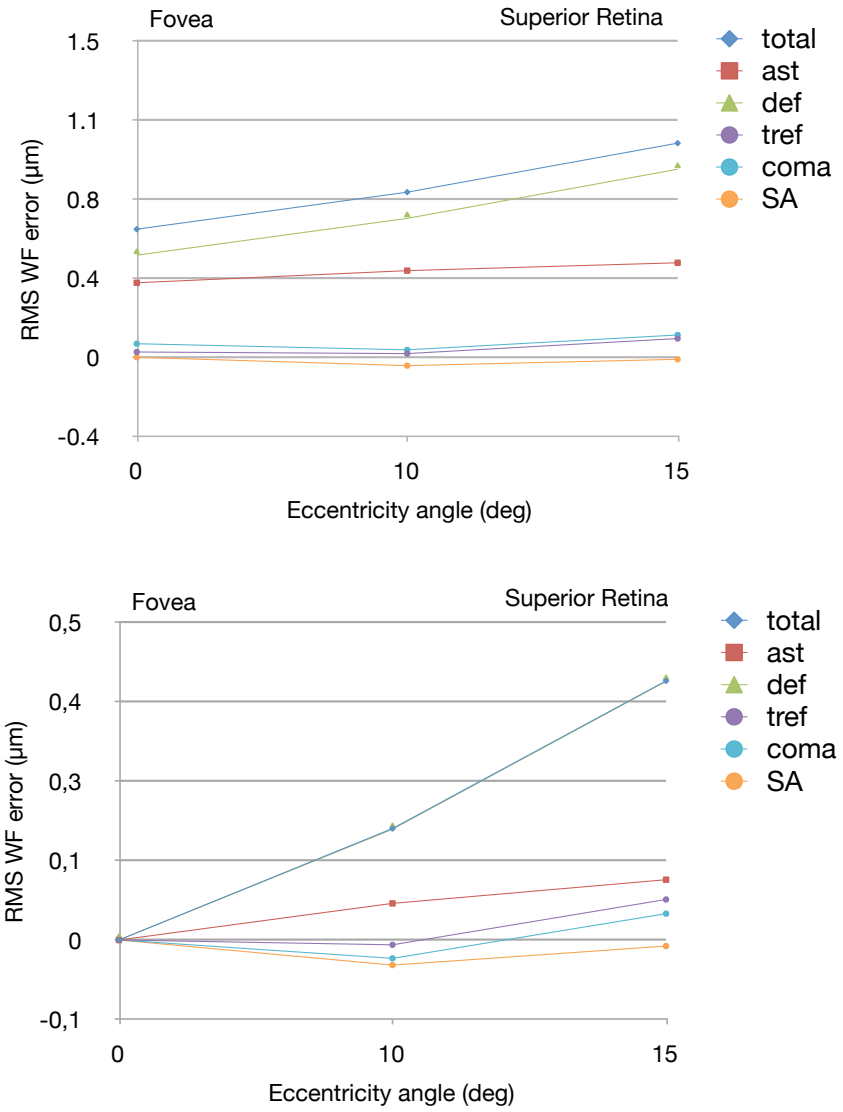

FIGURE 4.14 – RMS evolution for combination of aberrations in microns for 10 eyes for superior field (top). Residual values of RMS for combinations of aberrations once normalized respect to foveal value (bottom). Error bars have been omitted for clarity.

For completeness, the values of the coefficients are presented in the following Table 4.4.

	Superior Retina		
Zernike Coefficient	Fovea	10 deg	15d deg
	Mean ± *SD* [μm]	Mean ± *SD* [μm]	Mean ± *SD* [μm]
Z(2,-2)	0.148 ± 0.076	0.167 ± 0.0658	0.180 ± 0.06
Z(2,0)	0.486 ± 0.796	0.660 ± 0.653	0.893 ± 0.573
Z(2,-2)	0.322 ± 0.075	0.377 ± 0.069	0.412 ± 0.082
Z(3,-3)	0.006 ± 0.067	0.000 ± 0.123	0.071 ± 0.173
Z(3,-1)	0.027 ± 0.097	-0.02 0 ± 0.155	-0.105 ± 0.159
Z(3,1)	0.06 ± 0.102	0.031 ± 0.089	0.022 ± 0.083
Z(3,3)	0.026 ± 0.059	0.019 ± 0.079	0.056 ± 0.087
Z(4,-4)	0.008 ± 0.039	0.012 ± 0.055	0.039 ± 0.089
Z(4,2)	0.021 ± 0.043	0.04 ± 0.088	-0.005 ± 0.036
Z(4,0)	0.002 ± 0.086	-0.038 ± 0.174	-0.008 ± 0.095
Z(4,2)	0.005 ± 0.053	0.04 ± 0.071	0.081 ± 0.148
Z(4,-4)	0.033 ± 0.069	-0.016 ± 0.05	-0.054 ± 0.125
Z(5,-5)	0.000 ± 0.043	0.014 ± 0.104	-0.01 0 ± 0.044
Z(5,-3)	-0.017 ± 0.067	0.048 ± 0.085	0.034 ± 0.048
Z(5,-1)	-0.025 ± 0.051	-0.017 ± 0.054	-0.035 ± 0.092
Z(5,1)	0.033 ± 0.096	0.013 ± 0.039	0.009 ± 0.033
Z(5,3)	0.009 ± 0.036	-0.001 ± 0.024	0.017 ± 0.039
Z(5,5)	-0.003 ± 0.038	-0.005 ± 0.033	-0.001 ± 0.054

TABLE 4.4 – Measured the averaged values corresponding to Zernike Coefficients, up to 5th degree, measured at given eccentricities for superior retina.

In Figure 4.15, the values of the Zernike coefficients for the left eye of ten experimental subjects, and standard errors are depicted for three measuring points located in the nasal visual field.

From Figure 4.15 and Table 4.5, it can clearly be seen that the total RMS increases as we increase eccentricity in agreement with previous studies and as expected from the distribution of aberrations. The major impact on the RMS value is produced in this case by the second order aberrations, i.e. defocus and astigmatism. The value of both astigmatic terms increase in a linear way following a similar trend. The 3rd order terms do not change dramatically with the eld angle. And the 4th and 5th order aberrations have a little impact on the final retinal image quality. In Table 4.5, we also present the value of the RMS and additional information about RMS calculated after cancelling the influence of Z_2^0, i.e. corresponding to defocus, since it is one of the major contributors to the overall WF aberration. The contribution of the HOA to the total RMS value is also presented.

	RMS Values for Nasal Field				
Zernike Coefficient	Fovea	10 deg	15d deg	25 deg	35deg
	Mean ± *SD* [μm]	Mean ± *SD* [μm]	Mean ± *SD* [μm]	Mean ± *SD* [μm]	Mean ± *SD* [μm]
Total RMS	0.609 ± 0.844	1.035 ± 0.595	1.162 ± 0.617	1.223 ± 0.626	1.364 ± 1.095
Z(2,0)=0	0.367 ± 0.280	0.443 ± 0.325	0.679 ± 0.431	0.666 ± 0.471	0.702 ± 0.541
HOA RMS	0.094 ± 0.259	0.076 ± 0.268	0.147 ± 0.367	0.138 ± 0.377	0.099 ± 0.354

TABLE 4.5 – Calculated RMS values for the subjects included in the study. First row total RMS; second row, defocus has been removed; last row corresponds only to HOA.

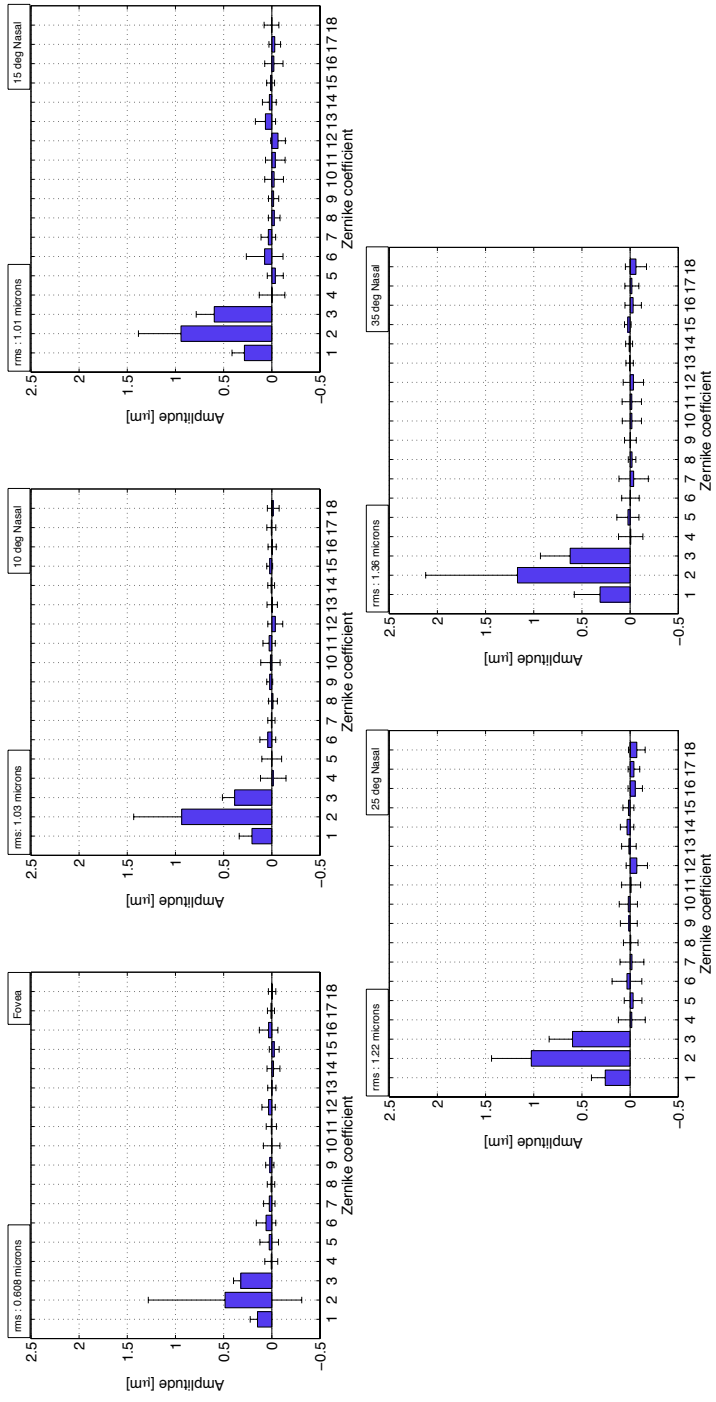

FIGURE 4.15 – Mean values of the Zernike coefficients up to 5th order for 5mm pupil diameter, increasing eccentricities from left to right continuing in the next line, on the nasal side. Error bars correspond to standard deviation.

In Figure 4.16, the values of the zernike coefficients for the left eye of ten experimental subjects and standard errors are depicted for three measuring locations in the temporal visual field.

	RMS Values for Temporal Field				
Zernike Coefficient	Fovea	10 deg	15d deg	25 deg	35deg
	Mean ± *SD* [μm]	Mean ± *SD* [μm]	Mean ± *SD* [μm]	Mean ± *SD* [μm]	Mean ± *SD* [μm]
Total RMS	0.609 ± 0.844	1.007 ± 0.646	1.022 ± 0.655	1.044 ± 0.678	1.149 ± 0.652
Z(2,0)=0	0.367 ± 0.280	0.464 ± 0.353	0.435 ± 0.290	0.505 ± 0.327	0.584 ± 0.342
HOA RMS	0.094 ± 0.259	0.094 ± 0.342	0.082 ± 0.275	0.085 ± 0.298	0.113 ± 0.304

TABLE 4.6 – Calculated RMS values for the subjects included in the study. First row total RMS; second row defocus has been removed; last row corresponds only to HOA.

From Figures 4.15 and 4.16, we can affirm that the major contribution to RMS are provided by the lower order aberrations, defocus Z_2^2, and both components of astigmatism Z_2^2 ,Z_{-2}^2 being the second order astigmatism and the oblique astigmatism respectively. The RMS values increase slowly with eccentricity, as reported previously e.g. Lundstrom et al. [2009a] and Navarro et al. [1998].

We regrouped Zernike coefficients depending on the order of the aberration, i.e. 2nd order terms, and HOA split into following degrees, i.e. 3rd 4th and 5th. In Figure 4.17 is depicted the total value of RMS across the horizontal field.

Previous studies, such as Navarro et al. [1998], found substantial third-order aberrations that increased with visual eld angle. Our study involves ten eyes measured in both directions along the horizontal meridian, and we found that the results are similar. A small nasal-temporal asymmetry is visible, the former slightly higher than the latter. It has been mentioned that the second order aberrations produce the strongest contribution to the total value of RMS whereas higher order aberrations are contributing only minimally to the total wave aberration.

Figure 4.18 presents more detailed information about individual aberrations, including defocus Z_2^0, both components of astigmatism $((Z_2^2)^2 + (Z_2^{-2})^2)^{\frac{1}{2}}$, coma

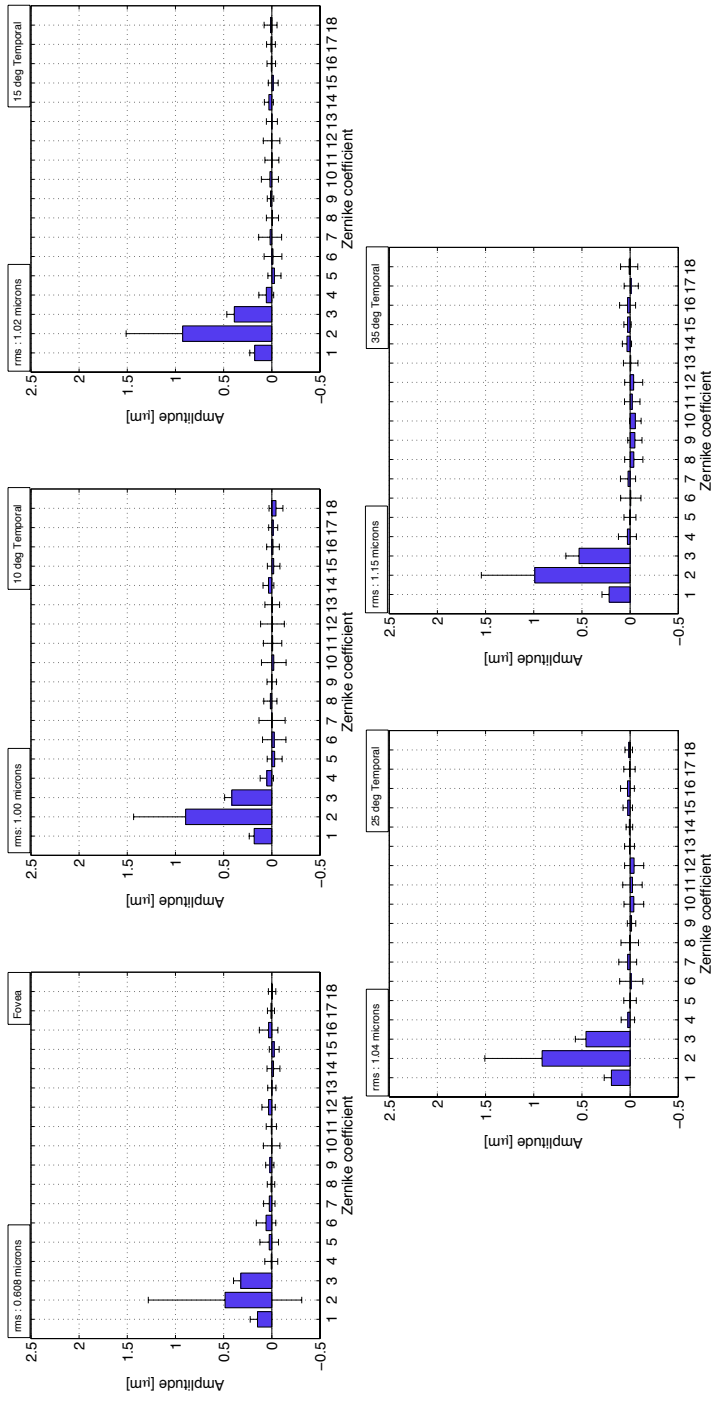

FIGURE 4.16 – Mean values of the Zernike coefficients up to 5th order for 5mm pupil diameter, increasing eccentricities from left to right continuing in the next line, on the temporal side. Error bars correspond to standard deviation.

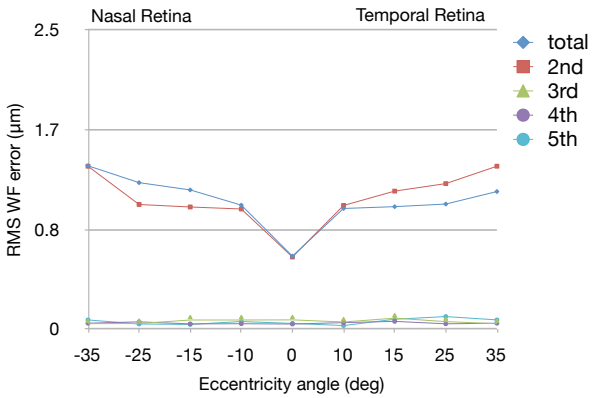

FIGURE 4.17 – RMS values in microns for 10 eyes across the horizontal field. Error bars have been omitted for clarity.

$((Z_3^1)^2 + (Z_3^{-1})^2)^{\frac{1}{2}}$, trefoil $((Z_3^3)^2 + (Z_3^0)^{-3})^{\frac{1}{2}}$, and spherical aberration Z_4^0 .

In Figure 4.20 we can see the field dependence of aberrations with eccentricity angle. A different method of visualization was used. In this case the value corresponding to the RMS at the foveal location (which was taken as a reference) has been subtracted in order to have more clear information about the aberrations evolution this operation to visualize peripheral aberrations has been used in Nowakowski [2010].

Similarly to the previous presented data, the second-order terms (defocus and astigmatism) are the major contributors. In the horizontal meridian, we have a symmetric distribution of increasing values of astigmatism.

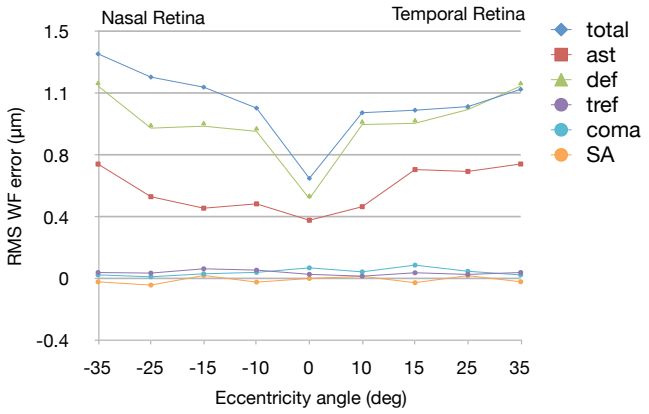

FIGURE 4.18 – RMS evolution for combination of aberrations in microns for 10 eyes across horizontal field. Error bars have been omitted for clarity.

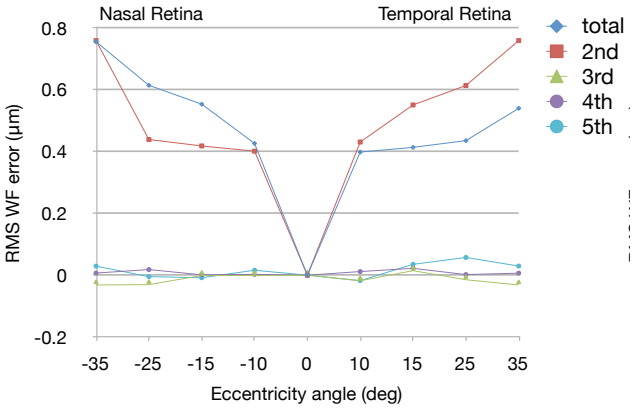

FIGURE 4.19 – RMS values in microns for 10 eyes across the horizontal field. The values of the aberrations, grouped by order, have been corrected to represent the residual aberrations once the value corresponding to the foveal location has been subtracted. Error bars have been omitted for sake of clarity.

Using absolute values reveals in a clearer way the main contributors to the WF error. Figure 4.20 presents more detailed information about individual aberrations. Including defocus Z_2^0, both components of astigmatism $((Z_2^2)^2 + (Z_2^{-2})^2)^{\frac{1}{2}}$, coma $((Z_3^1)^2 + (Z_3^{-1})^2)^{\frac{1}{2}}$, trefoil $((Z_3^3)^2 + (Z_3^0)^{-3})^{\frac{1}{2}}$, and spherical aberration Z_4^0 . This type of representation offers a better way of visualization, since the field evolution of the grouped aberrations is presented. It is worth to

notice that defocus was not corrected in any our measurements.

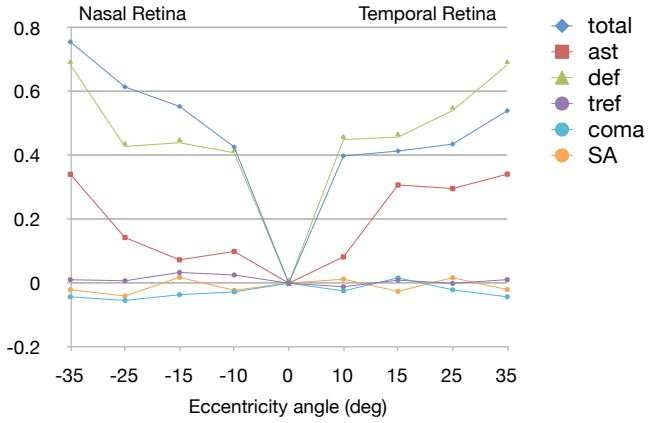

FIGURE 4.20 – Residual values of RMS for combinations of aberrations after normalization with respect to the foveal value.

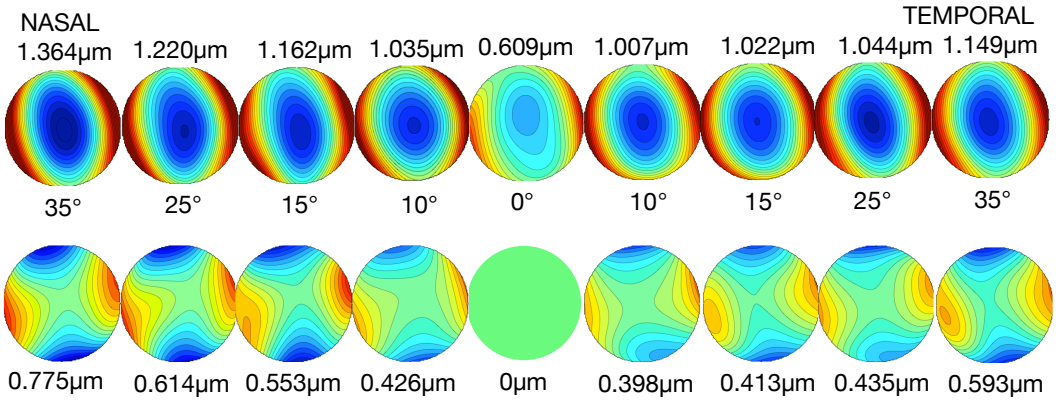

FIGURE 4.21 – Representation of the wavefront aberration for increasing eccentricities for human eye for the subjects included in the study, and increasing eccentricities from left to right

In Figure 4.21 the original wavefront maps correspondent to emmetropic study and the residual ones for all the measured eccentricities are depicted.

For completeness, the values of the coefficients are presented in Tables 4.7 and 4.8.

	Nasal Retina				
Zernike Coefficient	Fovea	10 deg	15 deg	25 deg	35 deg
	Mean ± *SD* [μm]	Mean ± *SD* [μm]	Mean ± *SD* [μm]	Mean ± *SD* [μm]	Mean ± *SD* [μm]
Z(2,-2)	0.148 ± 0.076	0.206 ± 0.1327	0.285 ± 0.128	0.258 ± 0.144	0.311 ± 0.2681
Z(2,0)	0.486 ± 0.796	0.935 ± 0.4981	0.943 ± 0.4417	1.026 ± 0.4125	1.169 ± 0.9525
Z(2,2)	0.322 ± 0.075	0.385 ± 0.127	0.598 ± 0.1866	0.598 ± 0.2428	0.622 ± 0.3084
Z(3,-3)	0.006 ± 0.067	-0.015 ± 0.1322	-0.002 ± 0.1328	-0.018 ± 0.1395	-0.006 ± 0.1262
Z(3,-1)	0.027 ± 0.097	0.001 ± 0.1024	-0.036 ± 0.0832	-0.031 ± 0.0918	0.023 ± 0.1143
Z(3,1)	0.06 ± 0.102	0.042 ± 0.0824	0.074 ± 0.1906	0.033 ± 0.1542	-0.003 ± 0.0906
Z(3,3)	0.026 ± 0.059	0.004 ± 0.0376	0.036 ± 0.0756	-0.019 ± 0.1236	-0.037 ± 0.1523
Z(4,-4)	0.008 ± 0.039	-0.012 ± 0.0457	-0.025 ± 0.0602	-0.007 ± 0.0761	-0.021 ± 0.0393
Z(4,-2)	0.021 ± 0.043	0.022 ± 0.0309	-0.018 ± 0.0531	0.014 ± 0.0878	-0.003 ± 0.0612
Z(4,0)	0.002 ± 0.086	0.014 ± 0.1002	-0.024 ± 0.0972	0.019 ± 0.0943	-0.019 ± 0.0994
Z(4,2)	0.005 ± 0.053	0.028 ± 0.0638	-0.036 ± 0.1018	-0.010 ± 0.0987	-0.018 ± 0.1004
Z(4,-4)	0.033 ± 0.069	-0.036 ± 0.0778	-0.064 ± 0.0761	-0.070 ± 0.1107	-0.034 ± 0.1055
Z(5,-5)	0 ± 0.043	-0.004 ± 0.0535	0.066 ± 0.1046	0.012 ± 0.0754	0.005 ± 0.0384
Z(5,-3)	-0.017 ± 0.067	0.007 ± 0.0348	0.026 ± 0.0714	0.031 ± 0.0698	0.010 ± 0.0362
Z(5,-1)	-0.025 ± 0.051	0.022 ± 0.0304	0.012 ± 0.0408	0.017 ± 0.057	0.024 ± 0.0341
Z(5,1)	0.033 ± 0.096	-0.004 ± 0.0425	-0.021 ± 0.095	-0.053 ± 0.0748	-0.032 ± 0.0856
Z(5,3)	0.009 ± 0.036	0.005 ± 0.0464	-0.031 ± 0.0604	-0.040 ± 0.0605	-0.018 ± 0.0724
Z(5,5)	-0.003 ± 0.038	-0.015 ± 0.061	0.003 ± 0.0766	-0.070 ± 0.0865	-0.060 ± 0.1097

TABLE 4.7 – Measured averaged values corresponding to Zernike Coefficients, up to 5th degree measured at given eccentricities for the Nasal Retina.

Temporal Retina					
Zernike Coefficient	Fovea	10 deg	15 deg	25 deg	35 deg
	Mean ± *SD* [μm]	Mean ± *SD* [μm]	Mean ± *SD* [μm]	Mean ± *SD* [μm]	Mean ± *SD* [μm]
Z(2,-2)	0.148 ± 0.076	0.184 ± 0.051	0.177 ± 0.052	0.194 ± 0.074	0.218 ± 0.074
Z(2,0)	0.486 ± 0.796	0.894 ± 0.541	0.925 ± 0.587	0.914 ± 0.594	0.989 ± 0.555
Z(2,2)	0.322 ± 0.075	0.415 ± 0.074	0.389 ± 0.077	0.458 ± 0.111	0.530 ± 0.137
Z(3,-3)	0.006 ± 0.067	0.052 ± 0.069	0.058 ± 0.077	0.023 ± 0.070	0.028 ± 0.093
Z(3,-1)	0.027 ± 0.097	-0.029 ± 0.078	-0.027 ± 0.068	0.001 ± 0.065	0.002 ± 0.062
Z(3,1)	0.060 ± 0.102	-0.025 ± 0.122	-0.012 ± 0.092	-0.012 ± 0.120	-0.007 ± 0.105
Z(3,3)	0.026 ± 0.059	-0.003 ± 0.136	0.018 ± 0.119	0.025 ± 0.093	0.022 ± 0.078
Z(4,-4)	0.008 ± 0.039	0.016 ± 0.069	-0.007 ± 0.063	0.004 ± 0.090	-0.038 ± 0.094
Z(4,-2)	0.021 ± 0.043	0.001 ± 0.049	0.014 ± 0.034	-0.015 ± 0.044	-0.050 ± 0.074
Z(4,0)	0.002 ± 0.086	-0.021 ± 0.128	0.020 ± 0.089	-0.039 ± 0.102	-0.054 ± 0.060
Z(4,2)	0.005 ± 0.053	-0.008 ± 0.095	-0.001 ± 0.073	-0.025 ± 0.101	-0.022 ± 0.081
Z(4,-4)	0.033 ± 0.069	-0.007 ± 0.123	0.003 ± 0.086	-0.042 ± 0.099	-0.037 ± 0.094
Z(5,-5)	0.000 ± 0.043	-0.005 ± 0.076	0.000 ± 0.057	0.006 ± 0.051	-0.006 ± 0.075
Z(5,-3)	-0.017 ± 0.067	0.035 ± 0.056	0.031 ± 0.047	0.008 ± 0.034	0.033 ± 0.047
Z(5,-1)	-0.025 ± 0.051	-0.019 ± 0.065	-0.015 ± 0.051	0.024 ± 0.049	0.026 ± 0.038
Z(5,1)	0.033 ± 0.096	-0.012 ± 0.066	0.006 ± 0.044	0.028 ± 0.071	0.026 ± 0.083
Z(5,3)	0.009 ± 0.036	-0.015 ± 0.047	0.008 ± 0.046	0.007 ± 0.059	-0.012 ± 0.073
Z(5,5)	-0.003 ± 0.038	-0.043 ± 0.072	0.013 ± 0.067	0.014 ± 0.039	0.010 ± 0.090

TABLE 4.8 – Measured averaged values corresponding to Zernike Coefficients, up to 5th degree measured at given eccentricities for the Temporal Retina.

4.5 Remarks

The main purpose of the studies presented along this chapter was to measure the peripheral aberrations on the human eye along the horizontal field of view and two additional locations on the superior field.

After analyzing the previously presented data we could affirm that if was feasible to measure the aberrations on the human eye by means of HSWFS as previously reported in Lundstrom et al. [2005b], Lundstrom et al. [2009a] andSheenan et al. [2007] with small differences within equipment and protocol.

We were able to successfully measure the aberrations along the horizontal meridian and two vertical locations on humans (for 10 subjects).

The most important findings are :

- As expected the results show an increased value of aberrations for increased eccentricities either along horizontal meridian or along vertical meridians measured.
- We found a large a intersubject variability, despite the fact all our experimental subjects were young and their refractive error was intentionally low.
- There is present a temporal-nasal asymmetry present along the horizontal meridian. Having the temporal field lower value of aberrations than nasal locations.
- More eyes would be needed for a better statistical description of the variation of ocular aberrations. Despite this fact our results are consistent with the data reported in the literature on wave aberrations at the fovea, as well as on second-order peripheral aberrations.

Chapter 5

Optical quality of the pigeon eye

5.1 Abstract

In this work, we focused on the analysis of retinal image quality in birds, specifically pigeons *(Columba livia)*. Previous studies performed on chickens involved measurements of aberrations using a doublepass system and reported the aberrations in terms of the MTF Coletta et al. [2003]. The presence of a lower field myopia has also been demonstrated in ground foraging birds generally Hodos et al. [1976], Hodos and Erichsen [1990] as well as in chicks and amphibians Schaeffel et al. [1994].For the pigeon there is a study of Fitzke et al. [1985]. General studies of aberrations and myopia have been provided by De la Cera et al. [2006a] and Kisilak et al. [2002]. To our knowledge, there are no previous studies measuring the HOA in the pigeon eye.

In this study, we measured the ocular aberrations in the pigeon eye. Forty eyes of 20 subjects adult pigeons were examined for the evaluation of the off-axis values of aberrations as well as refractive status. Eighteen eyes (8 subjects) were explored along the vertical meridian centered on the fovea). Measurements were carried out on fully anesthetized animals. Eyelids were removed just before measurement were taken, and the birds were killed afterwards while still anesthetized. Wave aberrations were fit to up to 5th order Zernike polynomials (18 terms removing tip and tilt), and were evaluated to a common pupil size of 4mm. A calculation of the refractive state of the pigeon was performed based on the values of the 2nd order Zernike terms. In order to check the validity of our measurements, we cross-correlated those calculated values of refractive state with retinoscopic measurements.

The aim of this chapter is to investigate the following points:

- Analysis of preliminary wavefront measurements of avian eyes, i.e. chicken and pigeon.
- Estimation of values of refractive error in the pigeon eye calculated from HS values and comparison with retinoscopic measurements.
- Exploration of off axis HOA in the pigeon along the horizontal meridian.
- Analysis of the variation of the off axis HOA along vertical axis in the pigeon.

5.2 Overview of Pigeon Vision

To our knowledge, there are no previous studies involving measurements of aberrations on the pigeon eye, so this section will consider properties selected of the pigeon eye and other avian species.

The pigeon(*Columba livia*) is a good candidate for studies of visual behavior and visual optical quality. Indeed, the lateral orientation of their eyes in the head provides a good model for investigating the optical quality of a panoramic field of view. The binocular eld of the pigeon is not as extensive as in other avian species, some of which that have eyes more frontally placed.

The avian globe, in relation to the size of the skull, is generally very large, with almost 50 % of the skull volume being occupied by the eye Gunturkun and Hahmann [1994].

The eyes of the pigeon, with an axial length of about 10.5 mm, but much larger relative to their body size, and are clearly smaller than those of humans (24.5 mm) Hughes [1979]. The shape of the pigeon eye is different to the human. Typical the posterior segment in bird eye is bigger compared to the anterior pole as depicted in Figure 5.1.

While the pigeon and human data concerning MTF cannot be accurately compare, within the error limits of the estimated viewing distance the peak sensitivity for the pigeon lies at a spatial frequency of 0.07 cycles/min arc whereas the corresponding peak sensitivity for the human eye lies in the region of 0.1 cycles/min arc Nye [1968].

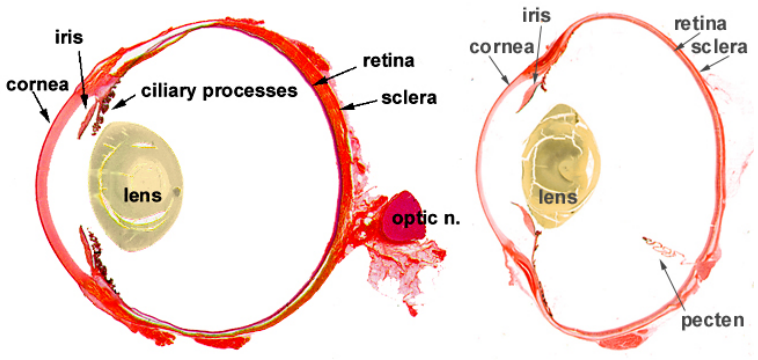

FIGURE 5.1 – Comparison between avian eye and mammal eye,Adapted from: http://www.class.cvm.uiuc.edu/j-eurell/eye14.htm

The binocular depth stereoacuity of the pigeon and its relation to the anatomical resolving power of the eye has been studied by McFadden [1987], who concluded that, despite the lateral position of the eyes of the pigeon, a small binocular field mediates the binocular discrimination of near objects in depth.

Objective measurements of the refractive error (which can be considered as low order aberrations) of the of the pigeon eye suggested that these eyes maintain the image quality off-axis some studies Fitzke et al. [1985], Erichsen [1979] have shown that the refractive state of the avian eye is relatively constant in frontal and lateral vision along the horizon but varies systematically between upper and lower visual fields. Along the horizon and in the upper visual field the eye is emmetropic. But the degree of myopia increases as elevation below the horizon increases especially in the frontal field. This means that birds can simultaneously focus near and distant objects on the ground and above the horizon, without changing the accommodative state of the eye Hahmann and Gunturkun [1993]. It has been reported by Hodos and Erichsen [1990] that lower field myopia is a biological adaptation in many ground foraging birds that is suited to keep the photoreceptors in the upper retina conjugate with the image of the ground. This result was considered in chicken by Schaeffel et al. [1994].

There are some studies regarding the refractive state of avian such as Gaffney and Hodos [2003], where all kestrels included in the study were found to be emmetropic. In that case, the establishment of refractive state was made by finding the trial lens that provided highest acuity. The closest study to ours

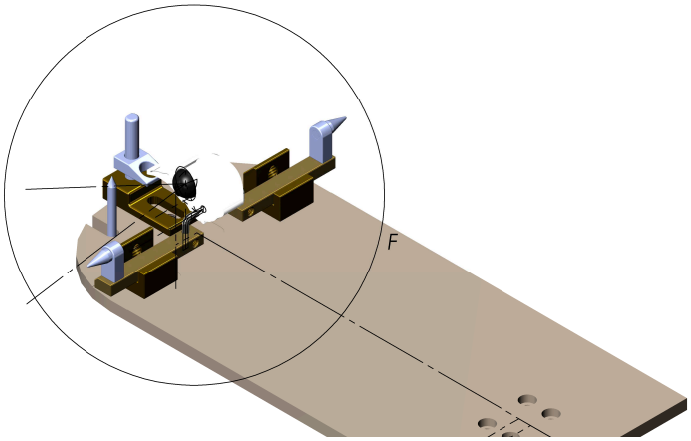

FIGURE 5.2 – Representation of the head-holder specially designed for pigeon aberration measurements

involving measurements of aberrations in avian eyes is that of Harmening et al. [2007] in which the subject was the barn owl and a standard Tscherning-type wavefront aberrometer was used under natural viewing conditions.

5.3 Experimental Design and Procedure

The experimental design is very similar that one used for measurements of human eyes, as previously described in 4.3. Pigeon aberrations were measured by means of the HSWFS previously described as 4.1. Our study subjects were under anaesthesia and the animals were restrained by a head holder specially designed for this purpose, as depicted in Figure 5.2.

The animal body laid on the platform represented in brown color in the figure. The body temperature was controlled by a heating pad placed underneath the animal body. The head holder was then attached to a rotating platform shown on Figure 5.3, this rotation stage provided micrometric control over the eccentricity angle to be measured. One of the components allowed the adjustment in height whereas the other two allowed us to modify the angles of the pigeon's head thus the eye.

The pupil camera provided continuous pupil monitoring to ensure that the Purkinje images remained within the pupil. Additional centration could be

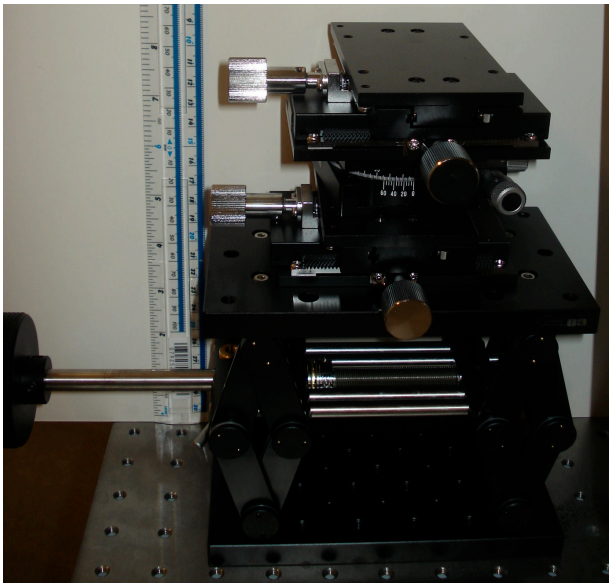

FIGURE 5.3 – Picture of the rotating stage assembled for pigeon measurments

achieved by moving the x-y stage that translates the animal. The measurements comprised 20 frames on each measurement which was repeated three times. The same procedure was repeated for the left and right eyes.

5.3.1 Data processing

The data acquisition software used was the same as previously described Chapter 4, additional MATLAB codes were developed to average and plot the pigeon data since the measured points were slightly different. Data were processed for a common pupil diameter of 4 mm. The optical quality of the eye was assessed in terms of individual Zernike coefficients up to fifth degree and the root-mean-square wavefront error RMS of the different terms or orders as previously described.

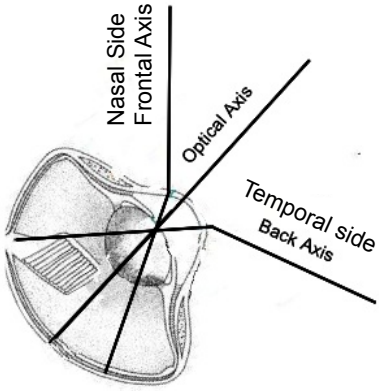

FIGURE 5.4 – Representation of the measurement axis.

5.4 Results

5.4.1 Preliminary Data. Post mortem analysis of WF for pigeon and chicken eyes

As a first approach to measuring wavefronts in birds, we examined the eyes of 3-week old chicken, killed immediately beforehand by overdose of anesthetic. The measurements were performed in a slightly different way because the absence of a stereotaxic head holder meant that eccentricity angles could not be properly determined. This axis configuration is shown in Figure 5.4.

The results of these measurements for three estimated retinal positions are shown in Figures 5.5 and 5.6. The positions are as follows: optical axis (near fovea), back or posterior position (nasal retina) and frontal position (temporal retina).

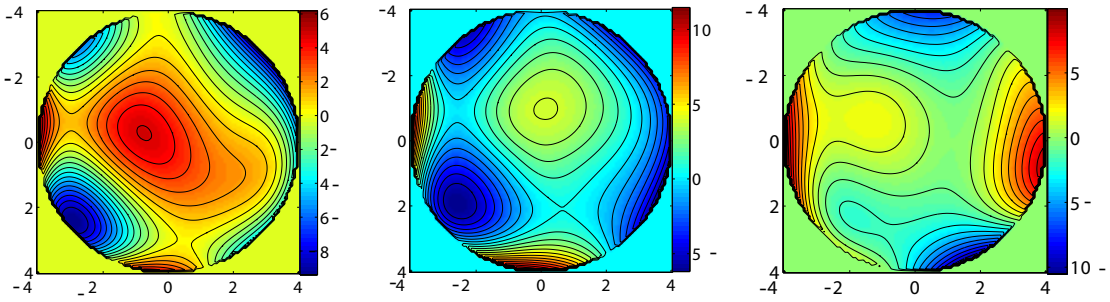

FIGURE 5.5 – Representation of the wavefront aberration for chicken eye OD for three different positions from left to right: back position, frontal position and optical axis.

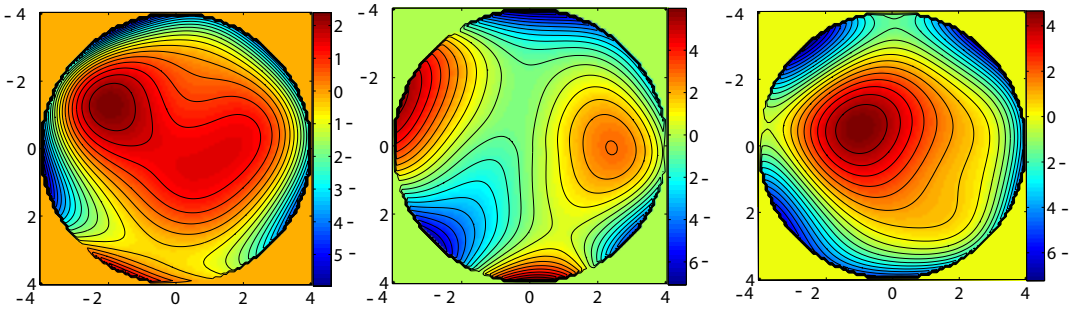

FIGURE 5.6 – Representation of the wavefront aberration for chicken eye OS for three different positions from left to right: back position, frontal position and optical axis.

5.4.2 Refractive measurements by retinoscopy

The subjects were adult homing pigeons *(Columba livia)*, and refractive errors were measured by means of retinoscopy before the measurements of WFS. Refraction was measured along the visual axis in the horizontal meridian using streak retinoscopy with trial lenses. Pigeons were awake and unanesthetized.

The refractive error of the subject was established and then the anesthesia was induced via intramuscular injection. Ketamine in the commercial form of Vetalar an clohidrate of Xylazine in the commercial form of Rompun. The combined use of those two pharmaceutical agents produces a deep surgical level of anaesthesia as well as muscle relaxation, including some dilation of the pupil.

5.4.3 Estimation of refractive error based on WF measurements

The wavefront measurements were done using the system previously described in (4.1), based on a 4-mm pupil and including up to fifth-order Zernike polynomials at 633 nm. This value of pupil size was fixed for all ofthe subjects to allow the comparison between them.

The shape of the wavefront describes the optics of the eye and can be used to evaluate refractive error. It is necessary to define the metric to be used in this case. As previously mentioned, our measurements are pupil based since the wave aberration was measured at the pupil plane. This is consistent with previous works such as Lundstrom et al. [2005b] and Thibos et al. [1997] and Fedtke et al. [2011].

The chosen option was to minimize the value of RMS of wavefront on foveal vision. The refractive correction can in this case simply be calculated from the second order Zernike coefficients Z_2^0, Z_2^2 and Z_2^{-2}, as follows:

$$M = -\frac{4\sqrt{3}}{{r_{pupil}}^2} Z_2^0 \tag{5.1}$$

$$J_0 = -\frac{2\sqrt{6}}{{r_{pupil}}^2} Z_2^2 \tag{5.2}$$

$$J_{45} = -\frac{2\sqrt{6}}{{r_{pupil}}^2} Z_2^{-2} \tag{5.3}$$

Where M represents defocus, and J_0 and J_{45} in diopters, which is known as the astigmatic decomposition with sphere, and Jackson cross-cylinders, one at 0 ° and the other at 45 °. These can be translated into traditional sphere, cylinder, and axis in the following manner:

$$cyl = -2\sqrt{J_0^2 + J_{45}^2} \tag{5.4}$$

$$axis = arctan\left(\frac{cyl + 2J_0}{-2J_{45}}\right) \tag{5.5}$$

If the axis is $< 0°$ we must add $180°$ and the total sphere is:

$$sphere = M - \frac{cyl}{2} \tag{5.6}$$

We measured each subject at angles from $70°$ nasally away from the fovea to $70°$ temporally in steps of $20°$. Figure 5.7 represents the spacing of the measurements performed for the evaluation of the off-axis aberrations along the horizontal meridian.

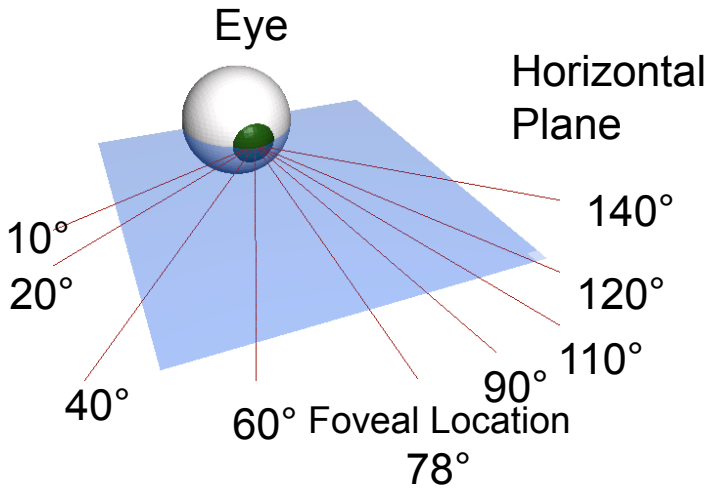

FIGURE 5.7 – Eccentricity angles along the horizontal meridian, measured in the pigeon eye

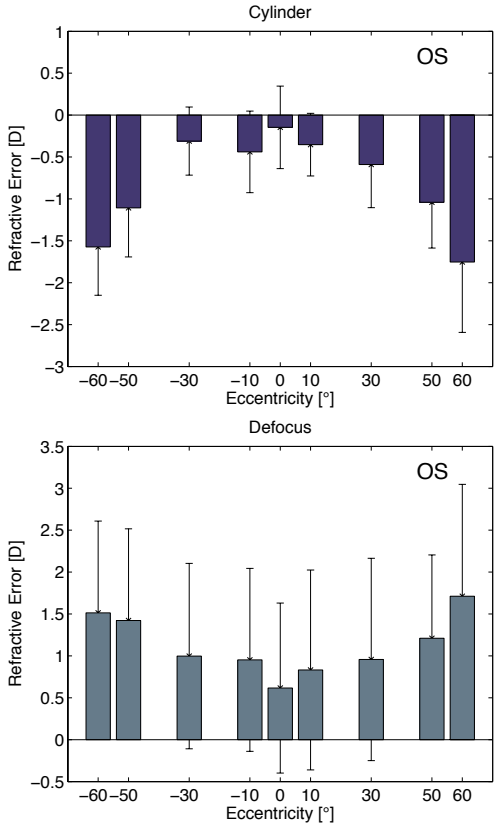

FIGURE 5.8 – Averaged values for astigmatism (left) and defocus (right), measured in the pigeon eye

In Figure 5.8, we present the calculated values for defocus and cylinder according to Equations 5.1 and 5.4, respectively, based on the Zernike coefficients measured with the HSWFS. The averaged values for defocus calculated for the eyes of the 20 subjects measured as well as and cylinders both follow an approximate " U-shape" in which higher values of defocus and astigmatism found at more eccentric are for the more eccentric positions. In Figure 5.9 we present the calculated sphere calculated according to Equation 5.9.

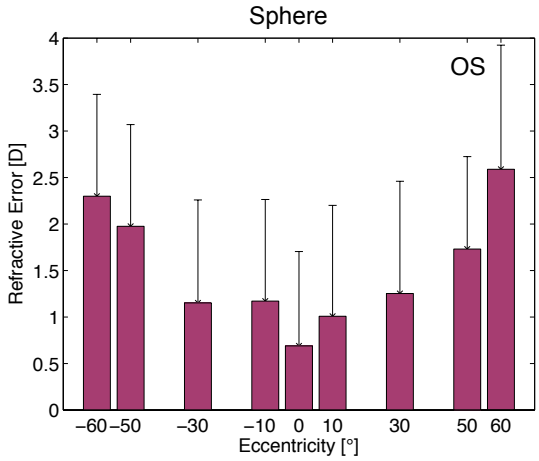

FIGURE 5.9 – Sphere measured on the pigeon eye

5.4.4 Analysis of Retinal Image Quality of Pigeon Eye along horizontal meridian

Our aim is to evaluate the retinal image quality of the pigeon eye. For that purpose, we started analyzing the horizontal meridian following the previously presented schema, see Figure 5.7, but in order to make our results clearer and easier to compare with the previously presented data corresponding to human eyes, the values of the angles have been converted with respect to the fovea being the measured angles 60 °, 50 °, 30 °, 10 ° , fovea, 10 °, 30 °, 50 °, 60 °. In the figures, negative degrees correspond to temporal locations whereas positive degrees correspond to nasal locations. In other words positive angles evaluation of the frontal visual field of the pigeon.

In Figures 5.10 and 5.11, the averaged Zernike coefficients for 20 left eyes are presented. From these data, we can observe that there is an asymmetry between both sides of the visual field, but contrary to what happens in human eyes, the values corresponding to nasal locations are lower than the temporal ones.

In Tables 5.1 and 5.2, the calculated RMS values are presented. We can observe that the overall value of the RMS with eccentricity. If we pay attention to the defocus corrected RMS, we can also affirm that also in this case that defocus plays a big role in the final value, whereas the influence of higher order aberrations is almost negligible.

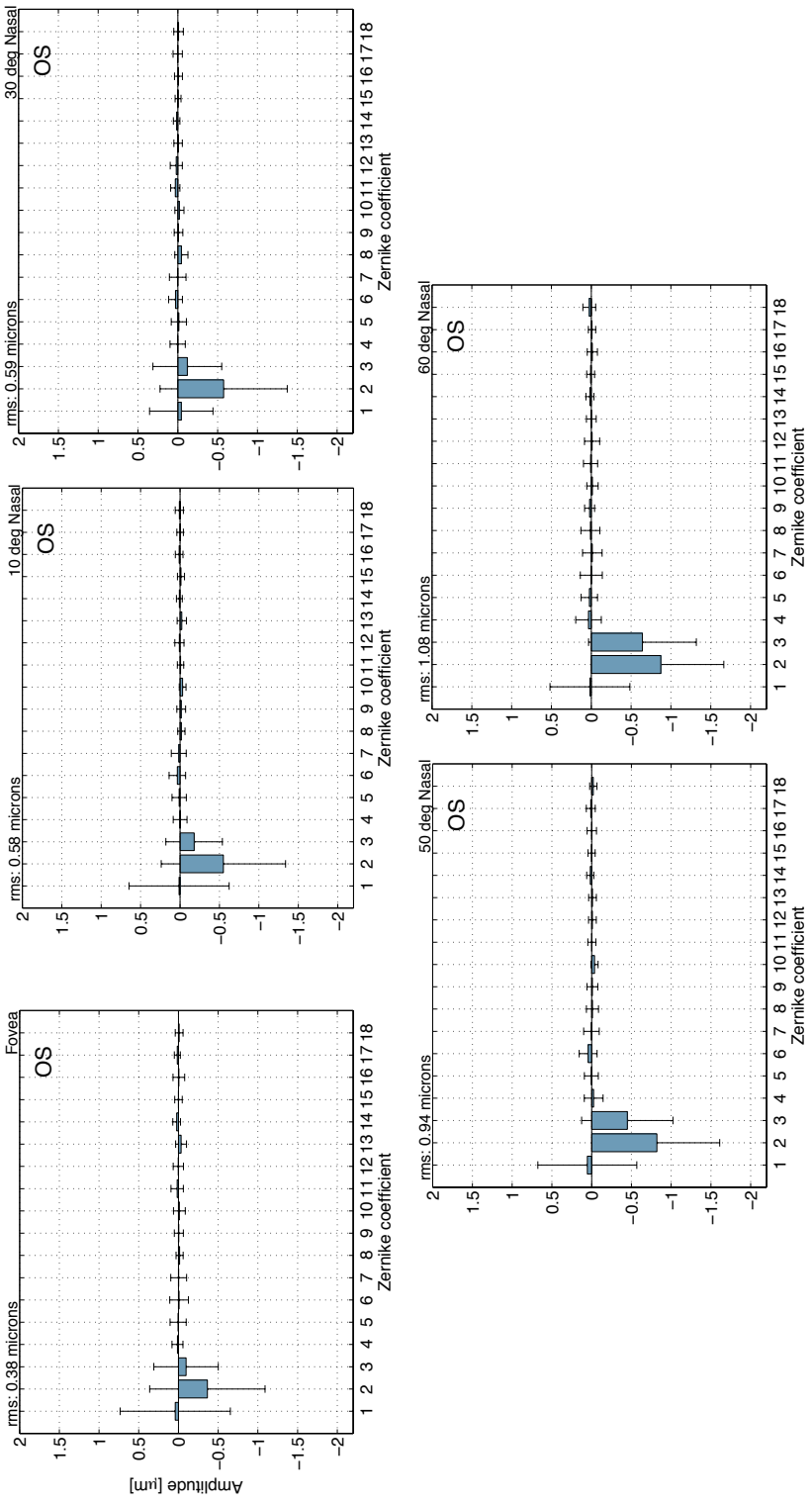

FIGURE 5.10 – Mean values of the Zernike coefficients up to 5th order for 4 mm pupil diameter, increasing eccentricities from left to right, on the nasal side. Averaged results from 20 left eyes. Error bars correspond to standard deviation.

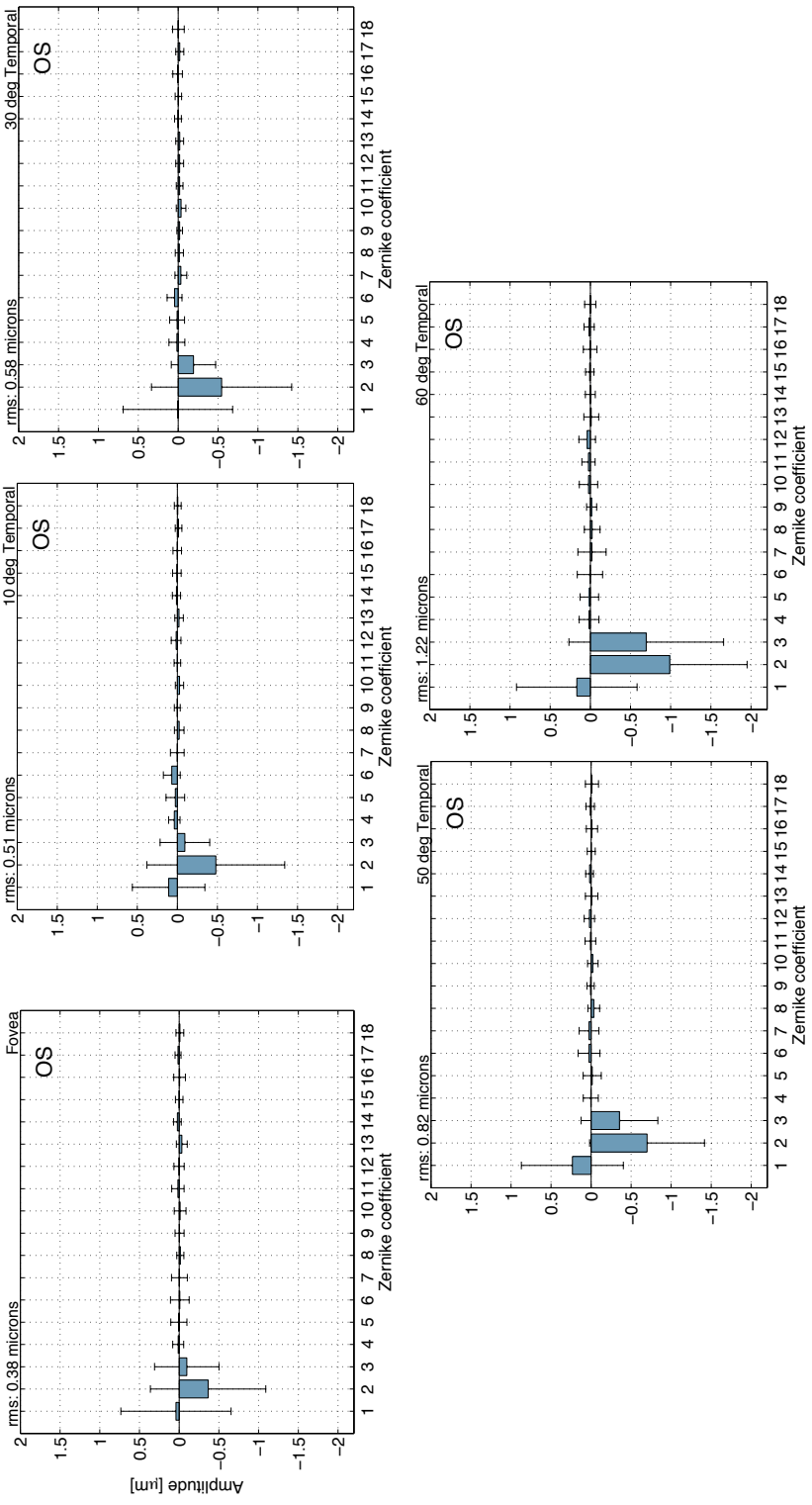

FIGURE 5.11 – Mean values of the Zernike coefficients up to 5th order for 4 mm pupil diameter, increasing eccentricities from left to right, on the temporal side. Averaged results from 20 left eyes. Error bars correspond to standard deviation.

	RMS Values for Nasal Field				
Zernike Coefficient	Fovea	10 deg	15d deg	25 deg	35deg
	Mean ± *SD* [μm]	Mean ± *SD* [μm]	Mean ± *SD* [μm]	Mean ± *SD* [μm]	Mean ± *SD* [μm]
Total RMS	0.382 ± 1.119	0.582 ± 1.102	0.594 ± 1.028	0.940 ± 1.190	1.086 ± 1.211
Z(2,0)=0	0.117 ± 0.851	0.146 ± 0.770	0.190 ± 0.647	0.458 ± 0.891	0.645 ± 0.917
HOA RMS	0.053 ± 0.279	0.064 ± 0.248	0.073 ± 0.272	0.072 ± 0.276	0.065 ± 0.364

TABLE 5.1 – Calculated RMS values for the subjects included in the study. First row total RMS; second row, defocus has been removed; last row corresponds only to HOA.

	RMS Values for Temporal Field				
Zernike Coefficient	Fovea	10 deg	15d deg	25 deg	35deg
	Mean ± *SD* [μm]	Mean ± *SD* [μm]	Mean ± *SD* [μm]	Mean ± *SD* [μm]	Mean ± *SD* [μm]
Total RMS	0.382 ± 1.119	0.510 ± 1.052	0.583 ± 1.175	0.821 ± 1.118	1.222 ± 1.606
Z(2,0)=0	0.117 ± 0.851	0.173 ± 0.605	0.209 ± 0.781	0.430 ± 0.858	0.719 ± 1.285
HOA RMS	0.053 ± 0.279	0.096 ± 0.255	0.084 ± 0.249	0.067 ± 0.318	0.068 ± 0.399

TABLE 5.2 – Calculated RMS values for the subjects included in the study. First row total RMS; second row, defocus has been removed; last row, corresponds only to HOA.

In order to better understand the influence of individual aberrations, a further calculation was made in Figure 5.12, which presents the total value of RMS along horizontal visual field. It can clearly be seen that the total RMS increases as we increase the angle, as expected from the distribution of aberrations. From this representation, we can see the nasal-temporal asymmetry, and it is worth noticing that the 2nd order aberrations mimic the overall value of RMS. As mentioned above, in the case of pigeon eye the HOA have a minor impact.

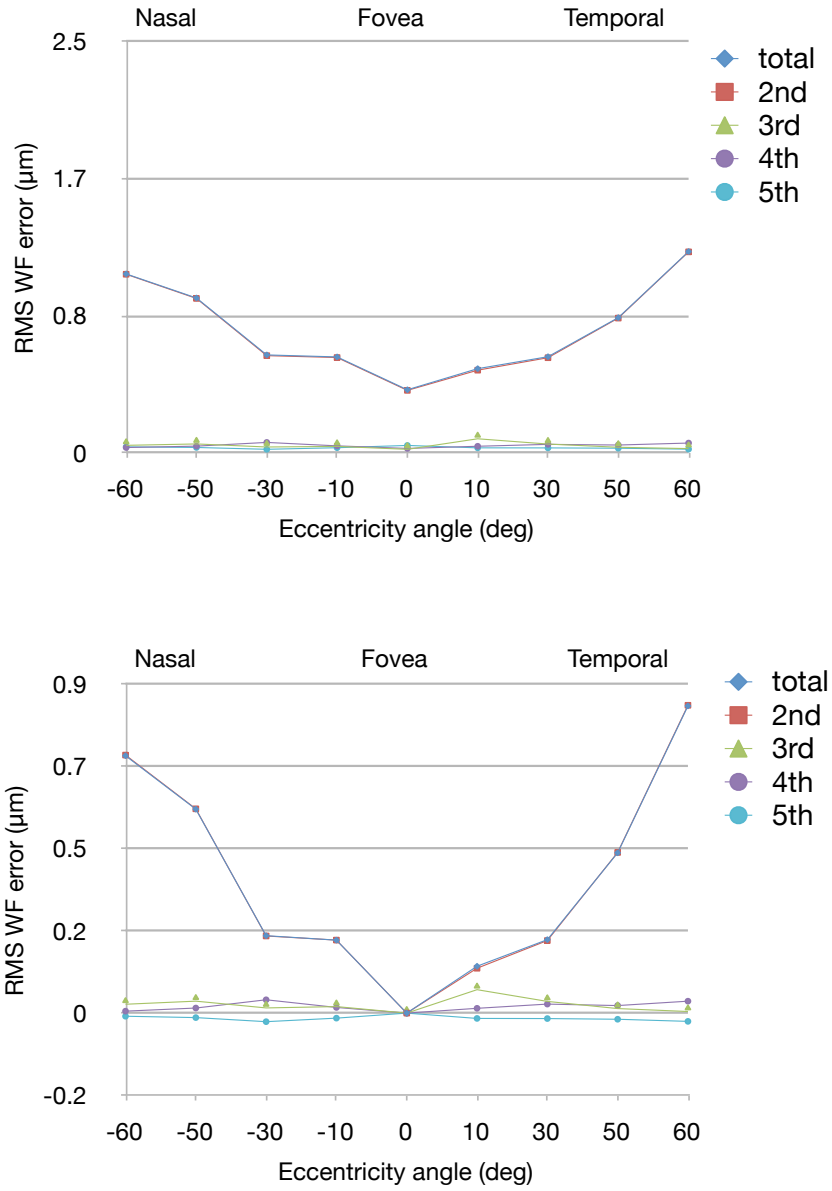

FIGURE 5.12 – RMS values in microns for 20 eyes across for superior field.The aberrations have been grouped according the order (top). The values of the aberrations have been corrected to represent the residual aberrations once the value corresponding to foveal location have been sustracted (bottom). Error bars have been omitted for clarity.

In Figure 5.13, we present the evolution of combinations of aberrations defo-

cus, both components of astigmatism $((Z_2^2)^2+(Z_2^{-2})^2)^{\frac{1}{2}}$, coma $((Z_3^1)^2+(Z_3^{-1})^2)^{\frac{1}{2}}$, trefoil $((Z_3^3)^2+(Z_3^0)^{-3})^{\frac{1}{2}}$, and spherical aberration Z_4^0.

This type of representation offers a better way of visualization. It has been mentioned above that the impact of lower order aberrations is very high, in these representations we can see that defocus and astigmatism follow opposite trends. In both cases, there is an increase in the absolute value of these terms, but the distribution seems to be symmetrical along an horizontal axis. This configuration may be an optimization to minimize the value of sphere. Spherical aberration, should not change by definition, and we can see that it remains mostly constant along the field, following a similar trend to that observed in humans.

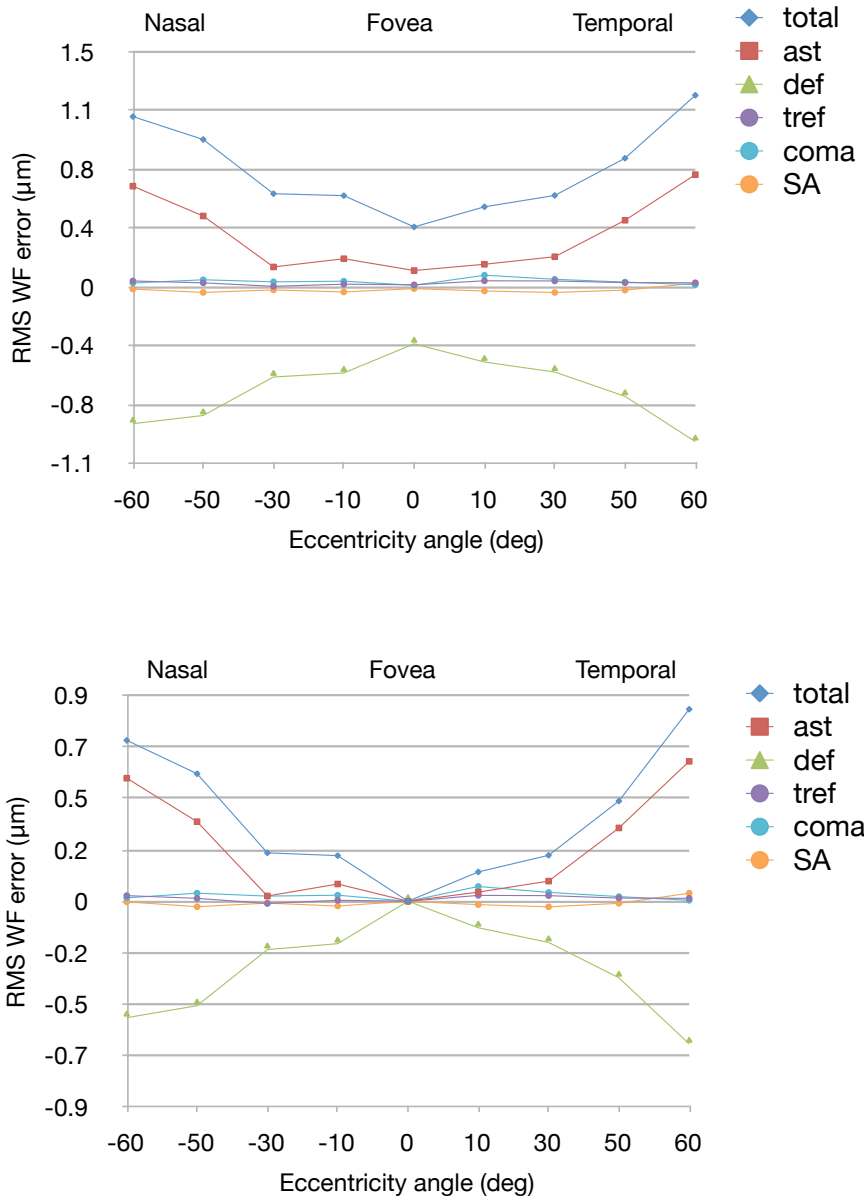

FIGURE 5.13 – RMS evolution for combination of aberrations in microns for 20 eyes for superior field (top). Residual values of RMS for combinations of aberrations once normalized respect to foveal value (bottom). Error bars have been omitted for clarity.

A wavefront plot is presented in Figure 5.14 where the overall shape of the

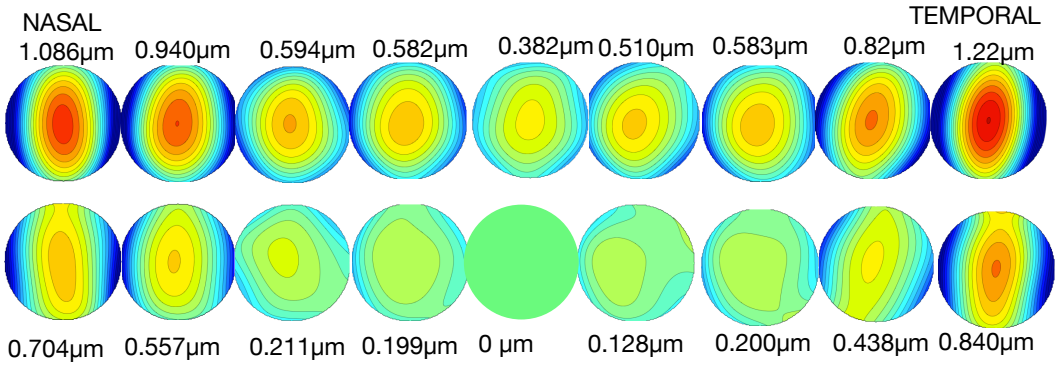

FIGURE 5.14 – Representation of the wavefront aberration for different eccentricities for thepigeon eye for the subjects included in the study, and increasing eccentricities from left to right.

WF is plotted in combination with the RMS calculated values. In the second row, the residual WF are depicted. This approach has been used before Nowakowski [2010] and in previous chapters of this work. We can see that the total WF is clearly degrading as we increase eccentricity.

For completeness, the averaged values of Zernike Coefficients for left eyes of 20 experimental subjects *(Columba Livia)* are presented in Tables 5.3 and 5.4.

	Nasal Retina				
Zernike Coefficient	Fovea	10 deg	30 deg	50 deg	60 deg
	Mean ± *SD* [μm]	Mean ± *SD* [μm]	Mean ± *SD* [μm]	Mean ± *SD* [μm]	Mean ± *SD* [μm]
Z(2,-2)	0.040 0.694	0.012 ± 0.635	-0.043 ± 0.398	0.055 ± 0.622	0.017 ± 0.501
Z(2,0)	-0.364 ± 0.727	-0.550 ± 0.788	-0.576 ± 0.798	-0.821 ± 0.789	-0.874 ± 0.790
Z(2,2)	-0.096 ± 0.405	-0.179 ± 0.359	-0.119 ± 0.432	-0.448 ± 0.574	-0.642 ± 0.677
Z(3,-3)	0.012 ± 0.070	-0.001 ± 0.088	0.002 ± 0.096	-0.025 ± 0.118	0.035 ± 0.161
Z(3,-1)	0.004 ± 0.101	0.011 ± 0.091	-0.013 ± 0.095	0.004 ± 0.088	0.024 ± 0.103
Z(3,1)	-0.008 ± 0.118	0.034 ± 0.105	0.029 ± 0.087	0.045 ± 0.113	0.000 ± 0.138
Z(3,3)	-0.003 ± 0.099	0.017 ± 0.095	0.002 ± 0.104	0.003 ± 0.098	-0.013 ± 0.123
Z(4,-4)	-0.015 ± 0.045	-0.017 ± 0.046	-0.044 ± 0.082	-0.010 ± 0.076	0.011 ± 0.119
Z(4,-2)	-0.005 ± 0.057	-0.015 ± 0.056	-0.008 ± 0.055	-0.010 ± 0.068	0.021 ± 0.063
Z(4,0)	-0.012 ± 0.074	-0.033 ± 0.043	-0.020 ± 0.057	-0.036 ± 0.045	-0.015 ± 0.071
Z(4,2)	0.017 ± 0.078	-0.006 ± 0.041	0.032 ± 0.058	-0.002 ± 0.050	0.009 ± 0.089
Z(4,-4)	0.002 ± 0.064	0.008 ± 0.058	0.019 ± 0.076	-0.009 ± 0.048	-0.010 ± 0.095
Z(5,-5)	-0.033 ± 0.068	-0.022 ± 0.058	-0.004 ± 0.053	-0.011 ± 0.049	0.000 ± 0.061
Z(5,-3)	0.023 ± 0.049	0.008 ± 0.037	0.015 ± 0.041	0.018 ± 0.045	0.017 ± 0.051
Z(5,-1)	-0.001 ± 0.047	-0.011 ± 0.045	-0.003 ± 0.037	0.001 ± 0.045	0.008 ± 0.049
Z(5,1)	-0.005 ± 0.073	0.011 ± 0.048	-0.008 ± 0.050	-0.001 ± 0.058	-0.013 ± 0.064
Z(5,3)	0.015 ± 0.038	-0.001 ± 0.042	0.002 ± 0.058	0.011 ± 0.056	-0.009 ± 0.046
Z(5,5)	-0.009 ± 0.049	0.009 ± 0.051	-0.010 ± 0.060	-0.021 ± 0.046	0.025 ± 0.081

TABLE 5.3 – Measured averaged values corresponding to Zernike Coefficients, up to 5th degree measured at given eccentricities for the Nasal Retina.

	Temporal Retina				
Zernike Coefficient	Fovea	10 deg	30 deg	50 deg	60 deg
	Mean ± *SD* [μm]	Mean ± *SD* [μm]	Mean ± *SD* [μm]	Mean ± *SD* [μm]	Mean ± *SD* [μm] height
Z(2,-2)	0.040 ± 0.694	0.109 ± 0.453	0.004 ± 0.686	0.234 ± 0.637	0.169 ± 0.751
Z(2,0)	-0.364 ± 0.727	-0.480 ± 0.861	-0.544 ± 0.878	-0.699 ± 0.718	-0.988 ± 0.963
Z(2,2)	-0.096 ± 0.405	-0.094 ± 0.310	-0.192 ± 0.278	-0.354 ± 0.479	-0.696 ± 0.963
Z(3,-3)	0.012 ± 0.070	0.038 ± 0.071	0.016 ± 0.100	0.004 ± 0.094	0.016 ± 0.123
Z(3,-1)	0.004 ± 0.101	0.025 ± 0.116	0.014 ± 0.093	-0.014 ± 0.113	0.012 ± 0.115
Z(3,1)	-0.008 ± 0.118	0.070 ± 0.106	0.046 ± 0.093	0.026 ± 0.136	0.005 ± 0.158
Z(3,3)	-0.003 ± 0.099	0.001 ± 0.086	-0.034 ± 0.074	0.026 ± 0.123	-0.020 ± 0.176
Z(4,-4)	-0.015 ± 0.045	-0.023 ± 0.060	-0.014 ± 0.051	-0.033 ± 0.073	-0.023 ± 0.098
Z(4,-2)	-0.005 ± 0.057	0.001 ± 0.038	-0.019 ± 0.035	0.007 ± 0.045	-0.015 ± 0.062
Z(4,0)	-0.012 ± 0.074	-0.027 ± 0.052	-0.036 ± 0.060	-0.021 ± 0.066	0.023 ± 0.114
Z(4,2)	0.017 ± 0.078	0.000 ± 0.041	-0.018 ± 0.042	0.008 ± 0.067	0.024 ± 0.082
Z(4,-4)	0.002 ± 0.064	0.015 ± 0.061	-0.019 ± 0.050	0.022 ± 0.065	0.039 ± 0.104
Z(5,-5)	-0.033 ± 0.068	-0.021 ± 0.053	-0.019 ± 0.049	-0.007 ± 0.078	-0.011 ± 0.092
Z(5,-3)	0.023 ± 0.049	0.011 ± 0.051	0.003 ± 0.043	0.019 ± 0.048	0.000 ± 0.062
Z(5,-1)	-0.001 ± 0.047	0.006 ± 0.054	-0.002 ± 0.040	-0.002 ± 0.050	0.008 ± 0.052
Z(5,1)	-0.005 ± 0.073	0.001 ± 0.053	0.007 ± 0.061	-0.010 ± 0.070	0.003 ± 0.085
Z(5,3)	0.015 ± 0.038	-0.015 ± 0.042	-0.020 ± 0.050	0.011 ± 0.052	0.016 ± 0.064
Z(5,5)”	-0.009 ± 0.049	-0.005 ± 0.043	-0.003 ± 0.073	-0.010 ± 0.082	0.002 ± 0.070

TABLE 5.4 – Measured averaged values corresponding to Zernike Coefficients, up to 5th degree measured at given eccentricities for the Nasal Retina.

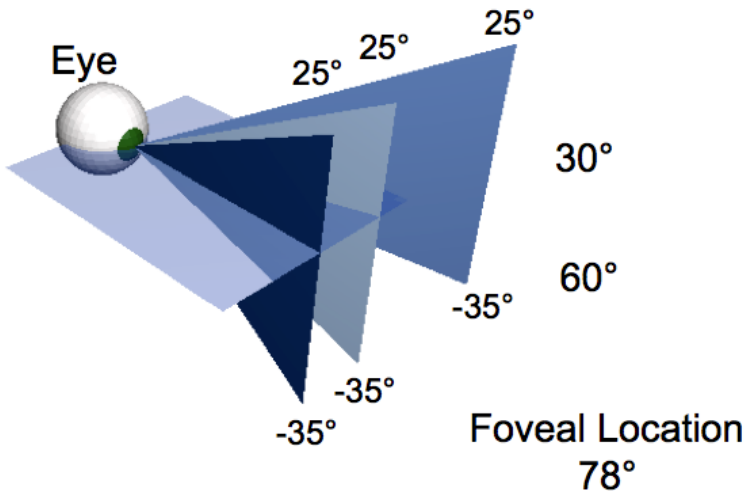

FIGURE 5.15 – Eccentricity angles along three different vertical meridians, measured on the pigeon eye

5.4.5 Analysis of Retinal Image Quality of Pigeon Eye along vertical meridians

The optical quality of the vertical meridians was investigated extensively, and the measurements were performed in three different planes, as depicted in Figure 5.15. In this case, we decided to measure three different meridians one as close as possible to the foveal position and two additional ones in the frontal visual field. Our aim was to measure along another meridian in the temporal field of view, but the quality of the images was not good enough to interpret them.

Exploration of refractive state at vertical meridians(87°, 60°, 30°) One set of measurements was performed at an azimuth of 87° we chose this position because it is the closest position to that of the fovea. The spatial and geometrical limitations of the head-holder made the measurements at the vertical meridian at 78°, which contains the fovea, impossible.

In Figure 5.16, the mean values for the 8 subjects measured are presented. For the measurements at 87° there is a decrease in the value of the defocus. As expected and previously presented in the literature, there is a "lower field myopia" of about 1D but our case the total values are not myopic but rather less hyperopic, when compared to foveal values. The values of defocus around the

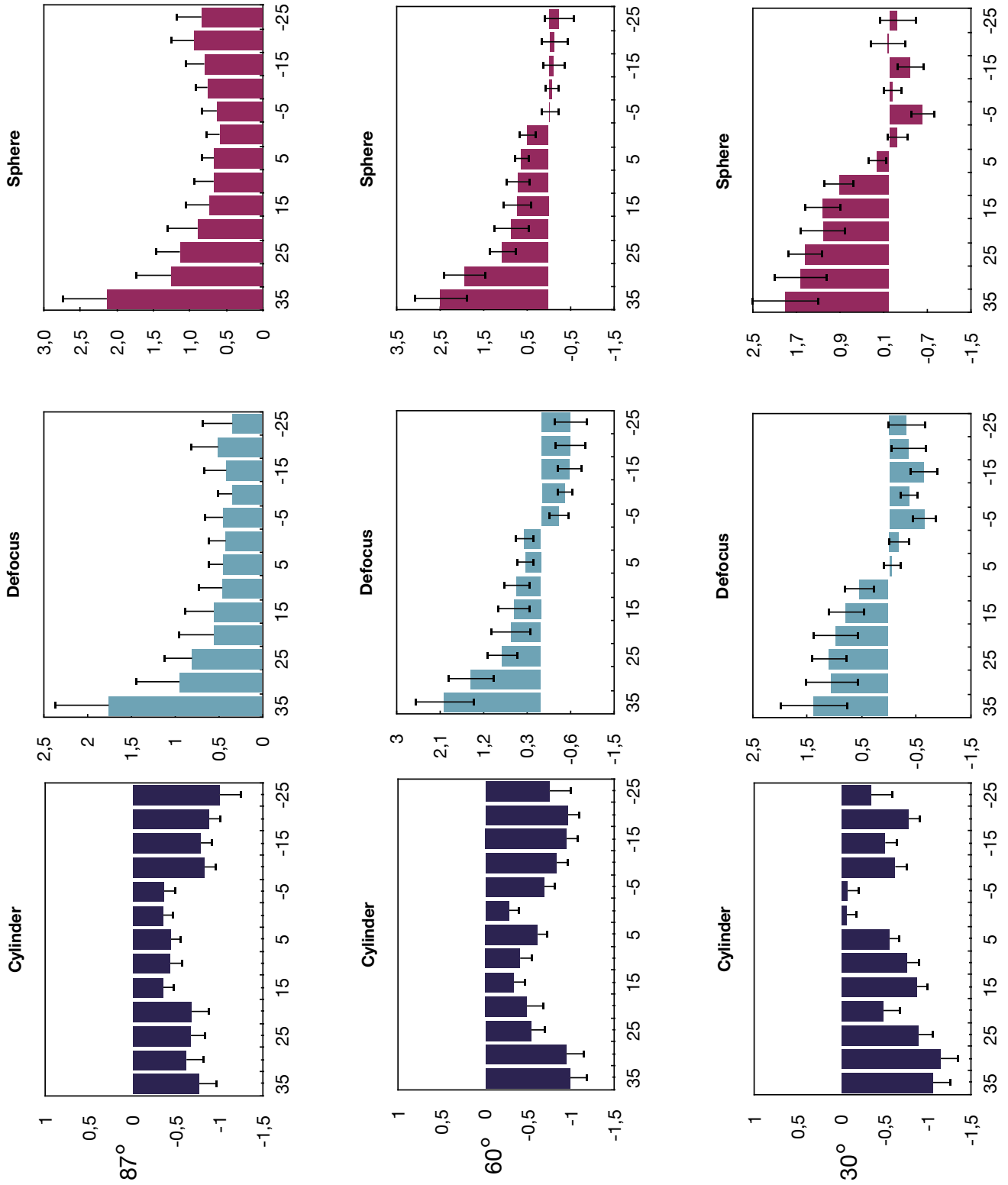

FIGURE 5.16 – Representation of the measured values of Defocus, Astigmatism and Sphere measured for 8 subjects, three different meridians 87 (top row), 60 (middle) and 30 (bottom) .

fovea, in this case for 0°, are very close to emmetropia. It is also noticeable that for the upper part of the visual field the refractive error turns out to be hyperopic. This trend is also noticeable in the sphere, whereas the values for astigmatism are very low on average and rather constant along the measured meridian it is possible to discern the an "L shape" being the refractive error very high on the lower field of view and becoming progressively less myopic and remaining constant as previously mentioned since the astigmatism reaches minimum values around the fovea and increases slightly when moving peripheral.

For the measurements performed along the meridian at 60°, in the frontal visual field, away from the fovea. In Figure 5.16 (middle), it is noticeable the so-called "lower field myopia" where the values of defocus of the eye are hyperopic for the upper field, progressively more myopic whilst moving towards the fovea, and then becoming even more myopic for the lower visual field. Values of defocus are close to emmetropia in the foveal region. By observing Figure 5.16, we can understand that as a general trend, the measured values of astigmatism it also follow an "inverted U shape" and the values for the upper visual field are generally higher than fo the 90° meridian. The total amount is around 1D, and in this meridian for the upper part of the visual field, the values of astigmatism are higher than in frontal positions, corresponding to the lower visual field.

If we pay attention to bottom row from the plot 5.16 corresponding to the measurements along the meridian at 30°, we still observe the "inverted U shape" for astigmatism values, being it more acute in this case, which reaches a minimum at the fovea. In this case, the values corresponding to the lower field are lower than these correspondent to superior field. If analyze defocus values, we see that, for the superior field, the pigeon eye is hyperopic but there is a progression to emmetropia around the fovea while becoming myopic for the lower field.

Further calculations To better understand the influence of individual aberrations on the retinal image quality of the pigeon eye further calculations were made. In Figure 5.17 (top row) the total value of RMS along the vertical meridians are depicted. It can be clearly seen that the total RMS increases dramatically for the superior field in all cases. The minimum value is reached at 0 °, for all

cases. From this representation we can see the superior-inferior asymmetry, and is worth noting that both values of second order aberrations almost replicate the trend of the overall value of RMS in every meridian. In this case, as mentioned above, the HOA have only a minor impact on the overall RMS value. For the values measured along the meridian placed at 87 ° the amount of aberrations is higher for the superior field but then the value of RMS is more stable and the overall retinal quality is very constant. Along the meridian placed at 60 ° the asymmetry is still present but there is present a clear minimum around 0 ° and this trend is even more noticeable at 30 ° where is possible to see a clear minimum implying that the best retinal image s around the fovea in this case.

In Figure 5.17, (bottom row) we present the evolution of combinations of aberrations defocus, both components of astigmatism $((Z_2^2)^2 + (Z_2^{-2})^2)^{\frac{1}{2}}$, coma $((Z_3^1)^2 + (Z_3^{-1})^2)^{\frac{1}{2}}$, trefoil $((Z_3^3)^2 + (Z_3^0)^{-3})^{\frac{1}{2}}$, and spherical aberration Z_4^0. This type of representation offers a better way of visualizing optical quality. As mentioned above, the impact of the lower order aberrations is very high. In these representation we can see that defocus and astigmatism follow opposite trends. In both cases, there is an increase in the absolute value of these terms, but the distribution seems to be symmetrical along the horizontal axis. This configuration could be an optimization to minimize the value of sphere. Regarding spherical aberration, which should not change by definition, we can see that it remains mostly constant along the field following a trend similar to what has been observed in the human eye.

The following Figure 5.18 represents in a slightly different way the above mentioned data, the values have been normalized respect to the foveal value in order to better visualize the previously explained trends.

Wavefront plots and Zernike coefficients In Figures 5.19, 5.20 and 5.21 the values of the measured Zernike coefficients are depicted for the three measured vertical meridians. It is clear that the higher values are corresponding to the second order aberrations.

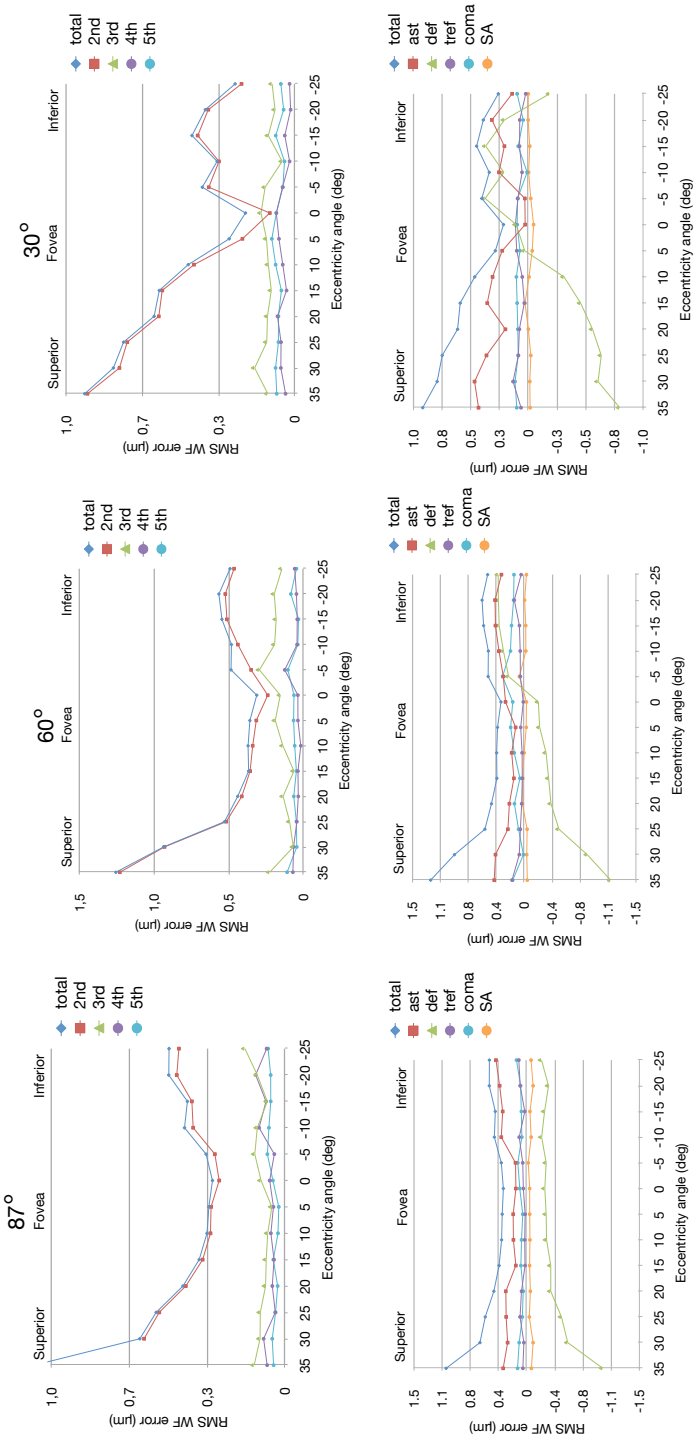

FIGURE 5.17 – RMS values in microns for 8 eyes across vertical meridians placed at 87°, 60° and 30° .The aberrations have been grouped according the order (top). Values of RMS for combinations of aberrations (bottom). Error bars have been omitted for clarity

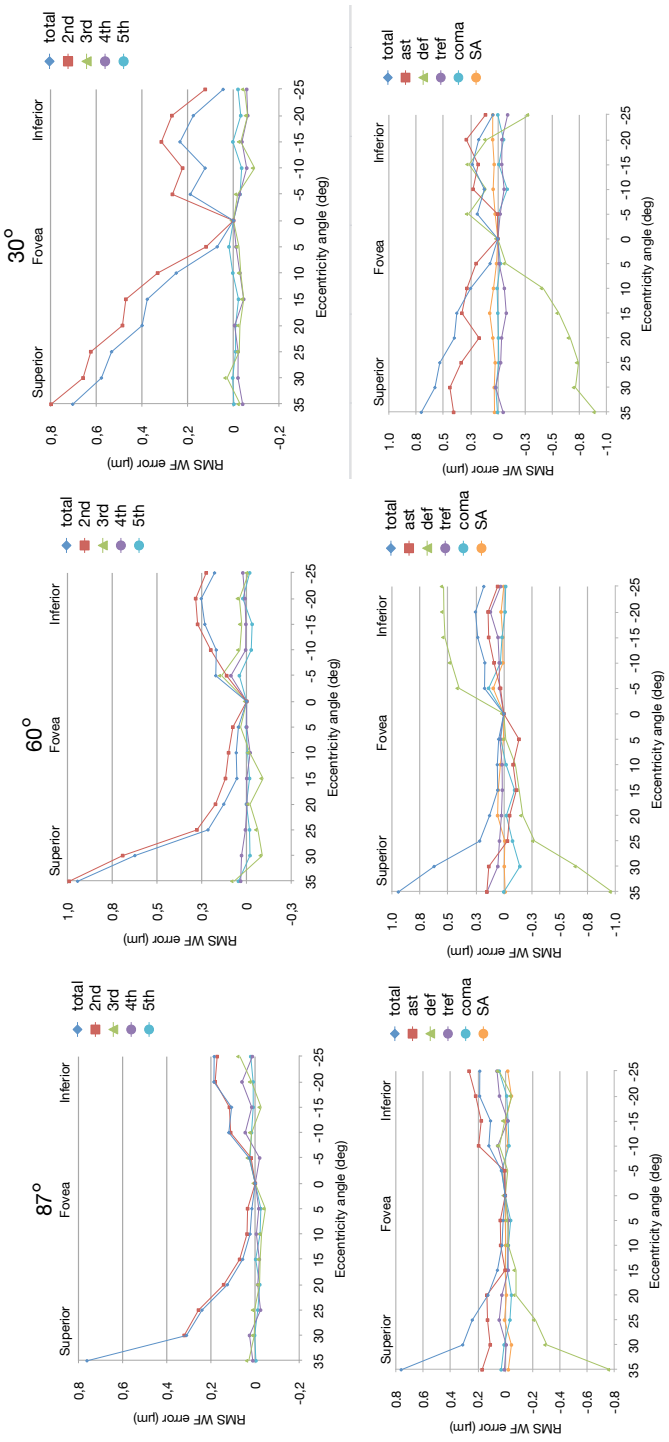

FIGURE 5.18 – RMS residual values across vertical meridians at 87°, 60° and 30° in microns for 8 eyes (top). Residual values of RMS for combinations of aberrations once normalized respect to the foveal value (bottom). Error bars have been omitted for clarity.

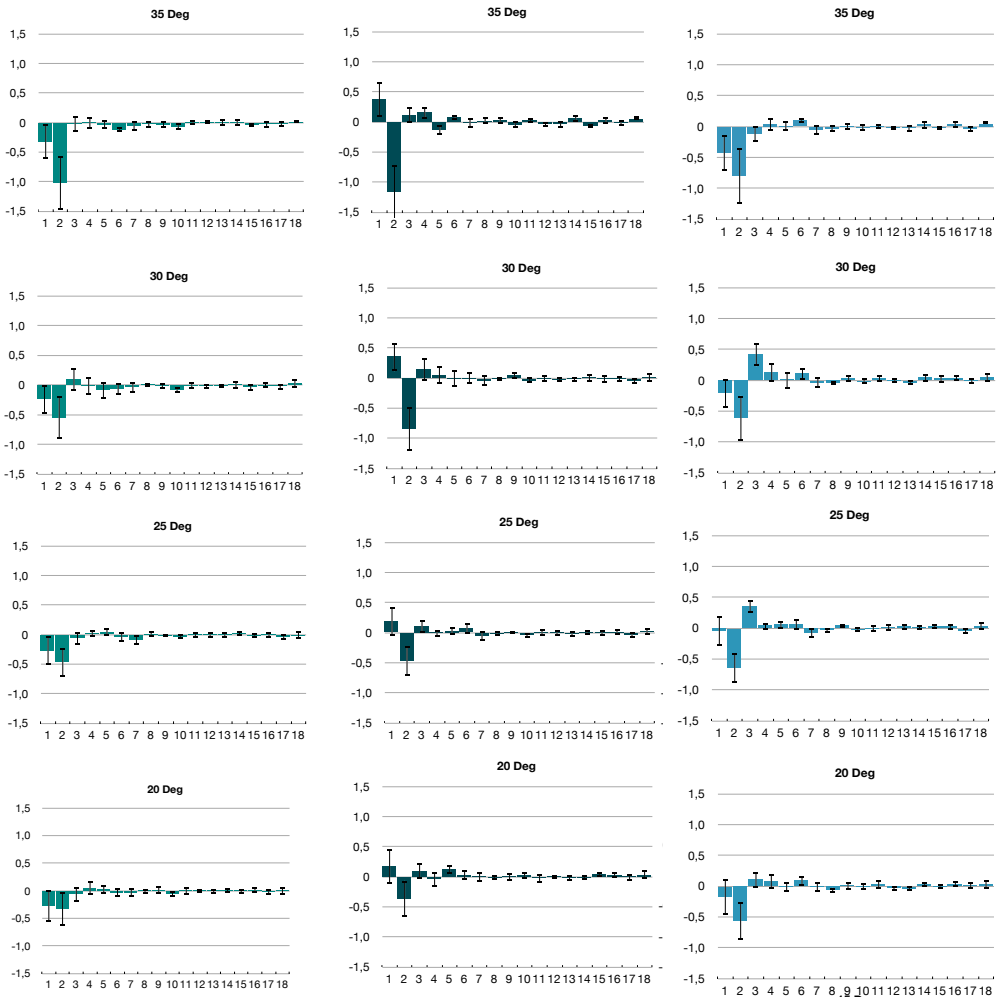

FIGURE 5.19 – Zernike coefficients along vertical meridians at 87° (left), 60° (middle) and 30° (right) for decreasing eccentricities from top to bottom for superior field

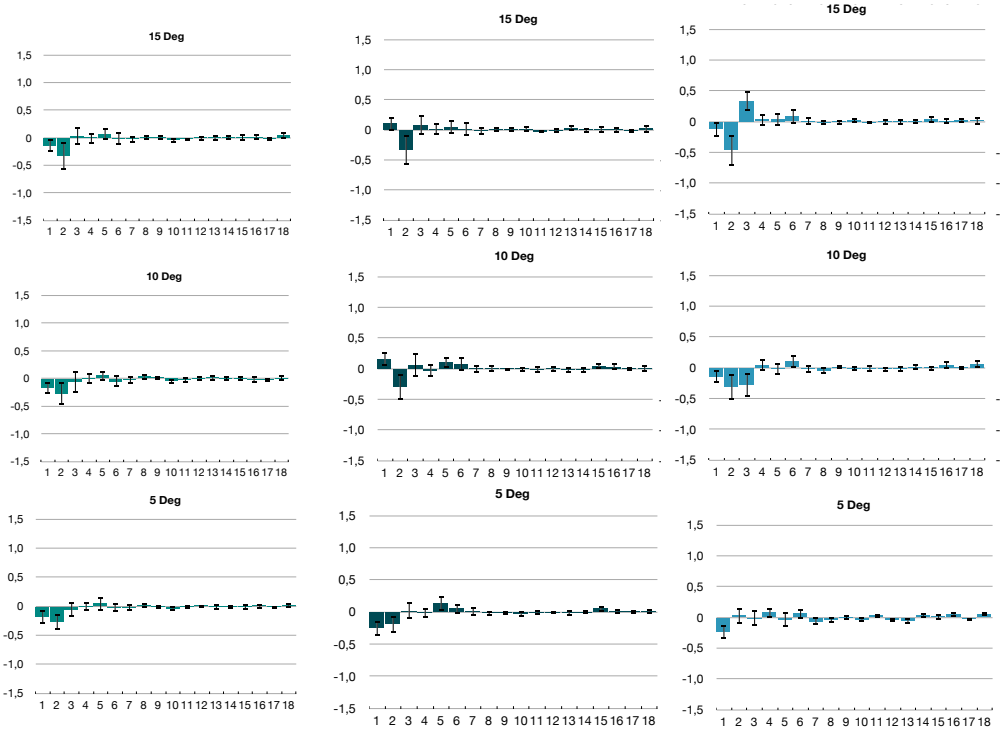

FIGURE 5.20 – Zernike coefficients along vertical meridians at 87° (left), 60° (middle) and 30° (right) for decreasing eccentricities from top to bottom for superior field

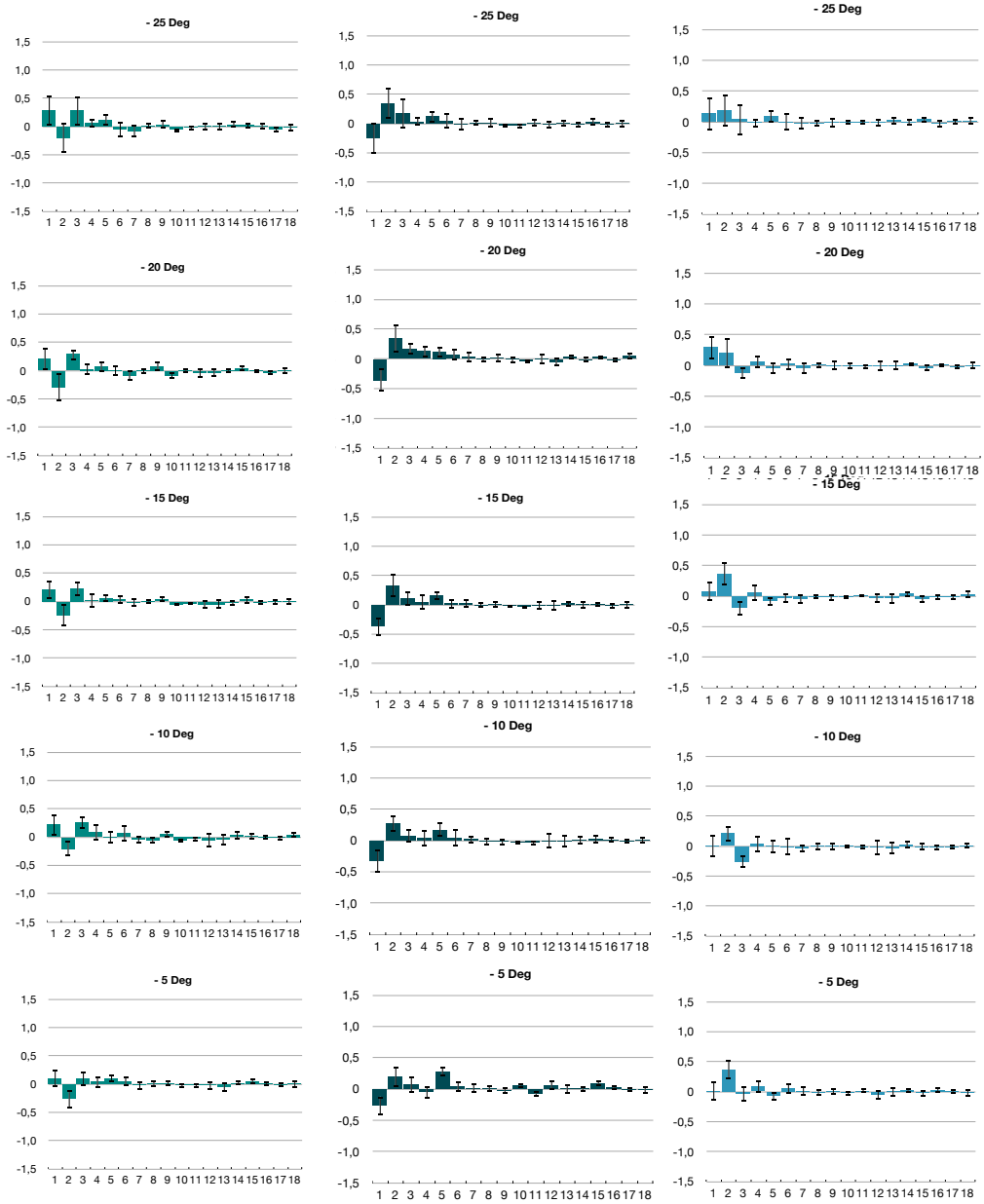

FIGURE 5.21 – Zernike coefficients along vertical meridians at 87° (left), 60° (middle) and 30° (right) for decreasing eccentricities from top to bottom for inferior field

Figures 5.22, and 5.23 presents the overall shape of the WF for the three different eccentricities, the calculated values of RMS are also present. This approach has been used before in the previous chapters of this work. There we can see that the total WF is degrading as we increase eccentricity especially in the superior field.

For the meridian at 30° and lower field, the values of the residual WF are surprisingly higher than the original ones. This could mean that there is present an evolutionary mechanism an the absolute minimum is not around the fovea so the calculation of residual WF is not so informative in this case.

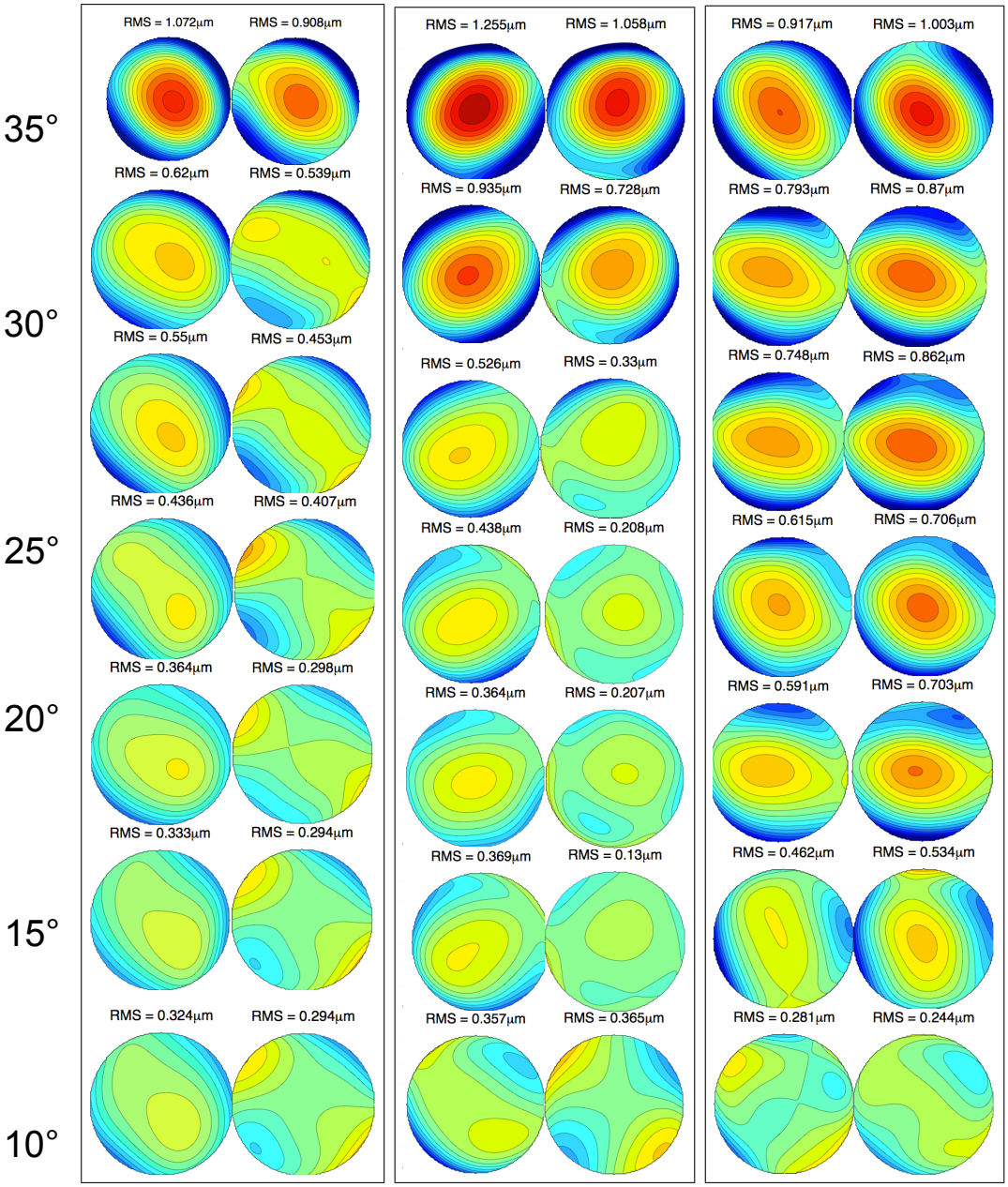

FIGURE 5.22 – Original and residual WF maps at 87° (left), 60° (middle) and 30° (right) for superior field

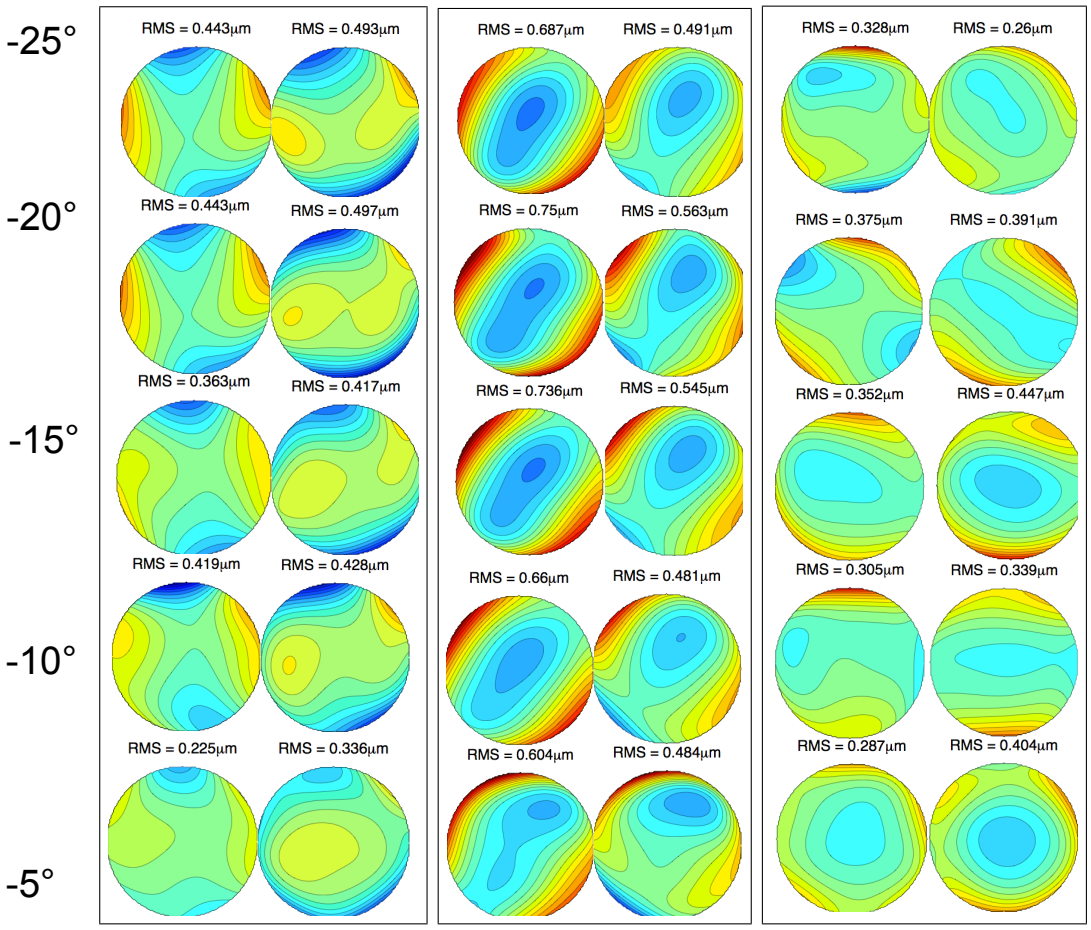

FIGURE 5.23 – Original and residual WF maps at 87° (left), 60° (middle) and 30° (right), for inferior field

5.5 Elliptical Pupils

In previous studies, such as the work by Lundstrom [2007] , theory and methods have been developed to handle the optical effects of the elliptical pupil that is present when we measure aberrations in very eccentric locations. We neglected the effect of the elliptical pupil in our study when off-axis measurements were reported for several reasons:

- To date, there is no commonly accepted format for reporting off-axis ocular aberrations.
- The evaluation over a stretched elliptical pupil is more complicated mathematically and requires stretching of both real and reference image positions. In this case, the spherical power correction does not involve only defocus but also has astigmatic coefficients. Therefore, more complicated equations are needed to determine the refraction equivalents.
- Comparing coefficients for different angles may not be valid because the stretching of the pupil changes their values differently. This fact was crucial in our study since our main aim was to provide a complete description of the retinal image quality in the pigeon eyes rather than a theoretical analysis of the effect of pupil shape on aberrations.

  only reasonable means for providing a consistent comparison between eyes is one based on the use of circular pupils.

In order to calculate Zernike coefficients for eccentric locations, the pupil can either be entirely enclosed within the elliptical pupil or it can have up to the same diameter as the major axis of the elliptical pupil. In the latter case, wavefront ts generate meaningless data outside the dimensions of the true pupil

We opted for the circle enclosed within the elliptical pupil, although this will lead to some loss of information in the evaluation of the optical aberrations in the periphery. We used the same pupil size across the entire range of visual eld positions whose diameter did not exceed the minimum minor axis of the ellipse at any of these positions.

5.6 Remarks

The main purpose of the studies presented in this chapter was to gain a better understanding of the distribution of aberrations in the pigeon eye.

After analyzing the previously presented data, we can affirm that it was feasible to measure the aberrations in the pigeon eye after small modifications of the already available equipment and methodology.

We were able to successfully measure the aberrations along the horizontal meridian (20 subjects) and three vertical meridians (8 subjects) in the pigeon eye.

The most important findings are :

- As expected, the results show an increased value of aberrations for increased eccentricities either along the horizontal meridian or along the vertical meridians measured. However, these increases were consistently much smaller than those found in the human eye.
- We found a large intersubject variability, comparable to the variability found in human eyes or even larger.
- A temporal-nasal asymmetry is present along the horizontal meridian in both human and pigeon eyes, but in human eyes the temporal eld has a lower value of aberrations whereas, in the case of pigeons, the lower values (on average) of the RMS are present for frontal rather than posterior positions.
- In the case of vertical meridians, we were able to measure the presence of the previously reported lower field myopia, our findings thus being in agreement with previous published studies.
- The refractive error corresponding to lower field locations is more myopic as we move towards the axis of the beak

Chapter 6

Discussion

The principal aim for this thesis is to achieve a comprehensive understanding of the image formation in the pigeon eye for peripheral locations using the well known technique as Hartmann-Shack Wavefront sensing, which widely used for the evaluation of overall retinal image quality of human eye.

The main noticeable feature of the peripheral retinal image is a progressive increased degradation as well as larger of higher order aberrations compared to foveal locations.

One of the objectives of this study was to establish the distribution of higher order aberrations along the field of view of the pigeon. A better description of these aberrations might lead us to a better understanding of the optical design of the pigeon eye and the evolutionary importance of panoramic vision.

The experimental data corresponding to the exploration of the horizontal meridian of the retina in the pigeon eye confirm that the overall retinal image quality remains fairly constant throughout the field, even for high eccentricities. By contrast, as already reported in the literature, in the human eye the quality on the retinal image is greatly reduced. The defocus and astigmatism measured experimentally across the central visual field although relatively low, change more than other aberration terms.

This characterization of the distribution of lower aberrations provides useful information that may be transferable to the optical design of artificial instruments.

The experimental data obtained from the human eye are consistent with the

absolute importance of the lower order aberrations, previously reported in the literature, on the final retinal image quality. Experimentally measured defocus and astigmatism along the chosen meridians again show a larger increase compared with the changes in other aberration terms.

6.1 Human Data

Following the analysis made in Chapter 4, we found remarkable the following observations regarding the off-axis distribution of ocular aberrations. As mentioned previously, the aberrations are affected by a high intersubject variability, the average value of RMS for foveal fixation is 0.609μm, which is consistent with the previous findings of Navarro et al. [1998] but slightly higher than those of Nowakowski [2010].

We found a naso-temporal asymmetry as previously reported, in the which the RMS values are lower for temporal locations than for nasal ones in the human eye. The RMS values increase slowly, in a roughly linear fashion, with eccentricity, such that, at 35° on the nasal side, the value has been increased by a factor of 2.23 and 1.88 on the temporal side. These results are consistent with previous findings concerning the off-axis optical quality of the eye, (Atchison and Scott [2002] and Gustafsson et al. [2001]) The sampling along the vertical axis, comprised only three locations (fovea, 5° and 10°), showed that the RMS value is increased by a factor of 1.67.

6.2 Pigeon Data

The visual system of the pigeon has been extensively studied using variety of neuroscientic approaches. In particular, these have included measures of behavioral visual acuity and sensitivity, both of which generally constituting the very limits of spatial vision in an animal.

The scientific interest devoted to the pigeon eye and visual system has been at leas in part driven by desire to know how do world looks through the

pigeon eye which has also ultimately inspired this work Erichsen [1979]. There are some anatomical studies about the pigeon eye such as that of Marshall et al. [1973] and electrophysiological studies such as that of Porciatti et al. [1991], in addition, and of brain areas that are largely devoted to vision, including topographical organization, have been identified. In this thesis, the author undertook some quantitative analysis the of visual imaging capabilities of the pigeon eye. Optical quality of the pigeon eye was assessed with objective measurements of wavefront aberrations.

We have determined that the retinal image of the pigeon eye is aberrated to some extent not only by lower order Zernike terms (e.g.astigmatism and defocus), but also by the higher-order terms, but the latter are less important in the overall degradation of retinal quality. In our study of the ocular aberrations of the pigeon eye off axis, we measured 20 eyes along the horizontal meridian of healthy subjects (*Columba livia*) which were about three years old. The measurements were performed under anesthesia. Additionally, we measured aberrations along three vertical meridians up to $+35\,^\circ$ in the superior field and $-25\,^\circ$ in the inferior field, by means of a purpose designed and built Hartmann Shack wavefront sensor. We were successful in describing the aberrations of the pigeon eye along both horizontal meridian and in the upper and lower visual fields. This knowledge yields important information about the overall image quality and could lead us to a better understanding of the optical structures of the pigeon eye.

We found a naso-temporal asymmetry, but in this case, and the RMS values are lower for nasal locations than for temporal ones contrary to what happens in the human eye. The RMS values increase slowly, in a roughly linear fashion with eccentricity, such that at $60\,^\circ$ the value has been increased by a factor of 2.84 on the nasal side and 3.19 on the temporal side. The naso-temporal asymmetry is not noticeable at $30\,^\circ$ since the average values are very similar; the factors are 1.55 on the nasal side and 1.52 on the temporal one.

The sampling along the vertical axis comprised only three locations, such as fovea, $5\,^\circ$ and $10\,^\circ$, the RMS value is increased by a factor of 1.67.

This fact provides supporting evidence for the hypothesis that the off-axis vision of avian eyes is corrected for the aberrations one might normally expect in the periphery of an optical system, reflecting an adaptation to their environment that allows for higher acuity in their peripheral vision.

6.3 Closing remarks

- We have developed technology to measure optical properties in animal models. In particular, we have developed a Hartmann-Shack wavefront sensor for measuring ocular aberrations in the pigeon eye. We have provided the first comprehensive results in the literature concerning the optical aberrations (in vivo, with anaesthesia) in this species.
- We have measured ocular aberrations for both the human and pigeon eye for identical locations and under similar experimental conditions. We found that optical quality in pigeons for identical peripheral locations is higher than in the human eye (i.e. total value of RMS is lower), as shown in Figure 6.1

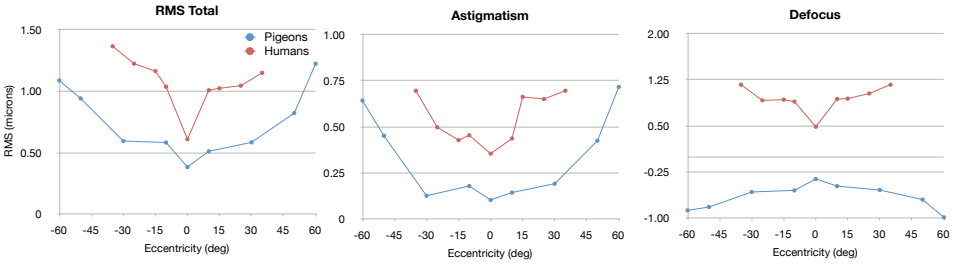

FIGURE 6.1 – Comparison between humans and pigeons of total RMS values Defocus and Astigmatism along the horizontal meridian. Error bars have been omitted for clarity.

- The hyperopic errors in the upper field for central vision found using Hartmann-Shack aberrometry in the pigeon eye are consistent with previous refractive errors in the literature.
- Lower order aberrations are the major sources of optical quality degradation, for peripheral vision in the pigeon eye as well as in the human

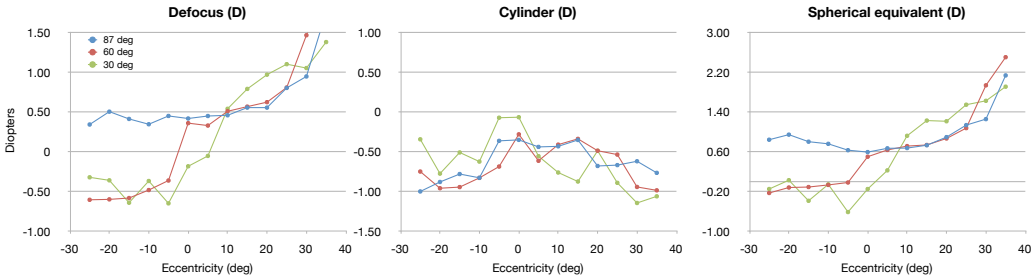

FIGURE 6.2 – Comparison of Defocus, Astigmatism and Sphere for the three vertical meridians measured in the pigeon eye. Error bars have been omitted for clarity.

eye.

– In pigeons, defocus along the horizontal meridian does not change dramatically whereas, along the vertical meridian, the presence of a lower field myopia is confirmed. Astigmatism of the eye for increasing eccentricity (horizontally and vertically) is consistently lower then expected theoretically and when compared with humans. This demonstrates that the visual optics of the pigeon are more fully corrected for peripheral vision than in humans. (Figures 6.2 and 6.3).

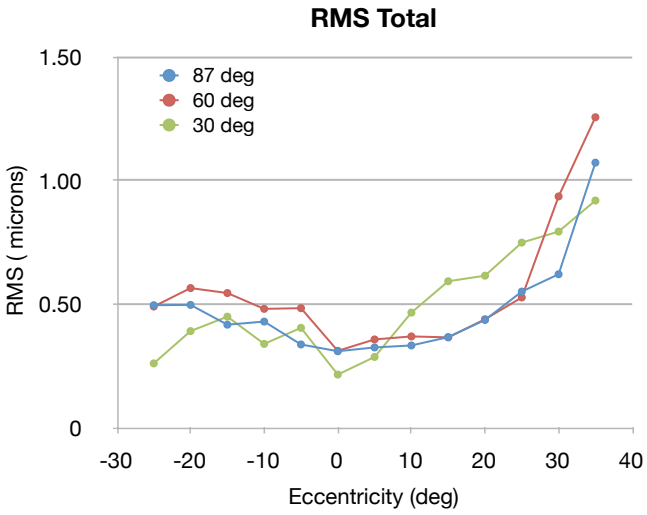

FIGURE 6.3 – Total RMS values for three vertical meridians in the pigeon eye. Error bars have been omitted for clarity.

6.4 Future Work

Our results from an analysis of 20 eyes for the horizontal meridian and 8 of the vertical meridian indicate a large inter-subject variability in aberrations distribution for the pigeon eye. Despite the fact that the pigeons were coming from the same source, i.e. normal healthy adult homing pigeons without any optical abnormality and a small age range, there remains considerable intersubject variability in both the horizontal and vertical meridians, but overall certain patterns do emerge in average.

In the case of the human eye, where since the sample size was smaller, but involved young eyes without any additional ocular disease and low refractive error, we can observe a high inter-subject variability. So we can affirm that the description of ocular aberrations over the field needs a more comprehensive way to describe it rather than the use of RMS, possibly involving a more in detail analysis of the evolution of Zernike terms in individual eyes.

Future work in this area should next include building a model eye for the pigeon:

- Ray tracing using schematic eye models could be carried out using known biometrical data to predict the measured refractive error and spherical aberration in the pigeon eye.
- Based on the aberration measurements already performed, it would be of interest to evaluate the influence of elliptical pupils for extreme eccentric locations. We neglected the effect of the elliptical pupil when conducting off-axis measurements. For our experiment, measured wavefront errors were evaluated using a common circular pupil of with the analysis software.
- Our experimental data on pigeon eyes may be incorporated into a model eye, including the analysis of the actual geometry of the cornea and lens. A better description of the lens structure including a gradient index description could lead us to an explanation of how the partial correction of aberrations is achieved.
- Other future work might involve the use the measured aberrations of the pigeon eyes to identify the isoplanatic patch size for this species.

Appendix

Appendix A

.1 Laser Classification

All lasers are divided into different classes depending on the wavelength and power of the laser. If the laser is designed to emit more than one wavelength the classification is based on the most hazardous wavelength. A difference is made between continuous laser light and pulsed laser light. For continuous light or repetitively pulsed lasers the average power output and limiting exposure time are considered. For pulsed lasers the total energy per pulse, the pulse duration, the pulse repetition frequency and emergent beam radiant exposure are considered. The different classes of lasers are :

Class 1 Class 1 lasers have a low output power (approximately 0.39 W or less) and are not hazardous for continuous viewing or are designed to prevent human access to the laser radiation.

Class 2a Class 2a lasers emit visible light not intended for viewing. The laser light is harmless if viewed directly for less than 1000 seconds (i.e. bar code scanners).

Class 2 Class 2 lasers emit visible light (400 to 700 nm), with an approximate power of 1 mW, which do not normally present a hazard to the eye, because the reflex to blink is fast enough to avoid damage. But it is hazardous to view directly into the laser light for a longer time (like it is with many other light sources, for example the sun).

Class 3a Class 3a lasers have an output power of approximately 5 mW or less. The light can cause eye injury, especially when the eye views it directly by optical (focusing) means.

Class 3b Class 3b lasers have an output power (approximately 500 mW or less) that can cause eye or skin injury from direct exposure, but they do not cause eye injury if the eye is exposed to a diffuse reflected beam.

Class 4 Class 4 lasers have an output power of more than 500 mW. Even a diffuse reflected beam can cause eye injury and it may also burn skin and clothing.

Bibliography

R.A. Applegate, Marsack J.D., and L.N Thibos. Metrics of retinal image quality predict visual performance in eyes with 20/17 or better visual acuity. *Optometry and Vision Science*, 83(9):635–40, 2006. 58

V. Arni, D. P. Sicam, et al. Spherical aberration of the anterior and posterior surfaces of the human cornea. *Journal of Optical Society of America A*, 23(3):544–548, 2006. 8

P. Artal and A. Guirao. Contributions of the cornea and the lens to the aberrations of the human eye. *Optics Letters*, 23(21):1713–1715, 1998. 12, 77

P. Artal, S. Marcos, R. Navarro, and D. Williams. Odd aberrations and double-pass measurements of retinal image quality. *Journal of Optical Society of America A*, 12(2):195–201, 1995. 76

P. Artal, E. Berrio, A. Guirao, and D. Williams. Compensation of corneal aberrations by the internal optics in the human eye. *Journal of Vision*, 1(1):1–8, 2001. 8, 12

P. Artal, E. Berrio, and A. Guirao. Contribution of the cornea and internal surfaces to the change of ocular aberrations with age. *Journal of Optical Society of America A*, 19(1):137–143, 2002. 8

P. Artal, A. Benito, et al. The human eye is an example of robust optical design. *Journal of Vision*, 6(1):1–7, 2006. 75

D. Atchison. Comparison of peripheral refractions determined by different instruments. *Optometry and Vision Science*, 80(9):355–359, 2003. 2

D. Atchison. Anterior corneal and internal contributions to peripheral aberrations of human eyes. *Journal of Optical Society of America A*, 21(2): 355–359, 2004. 77

D. Atchison. Recent advances in measurement of monochromatic aberrations of human eyes. *Clinical and Experimental Optometry*, 88(1):5–27, 2005. 76

D. Atchison and A. M. Charman. Hartmann-shack technique and refraction across the horizontal visual field. *Journal of Optical Society of America A*, 20(6):965–973, 2003. 2

D. Atchison and Markwell E.L. Aberrations of emmetropic subjects at different ages. *Vision Research*, 33(8):863–865, 2008. 74

D. Atchison and D.H. Scott. Monochromatic aberrations of human eyes in the horizontal visual field. *Journal of Optical Society of America A*, 19 (11):2180–2184, 2002. 76, 145

D. Atchison and D.H. Scott. Measuring ocular aberrations in the peripheral visual field using hartmann-shack aberrometry. *Journal of Optical Society of America A*, 24(9):2963–2973, 2007. 2

D. Atchison, M.J. Collins, C. Wildsoet, et al. Measurement of monochromatic ocular aberrations of human eyes as a function of accommodation by the howland aberroscope technique. *Vision Research*, 35(3):313 – 323, 1995. 74

A. Bayon, R.M. Almela, and J. Talvera. Avian opthalmology. *EJCAP*. 21

Bennett and Rabbett. *Clinical Visual Optics*. Butterworth-Heinemann, 4th edition, July 2007. 7

E. Berrio, J. Tabernero, and P. Artal. Optical aberrations and alignment of the eye with age. *Journal of Vision*, 10(14), December 2010. 74, 75

D.S. Blough. Spectral sensitivity in the pigeon. *Journal of Optical Society of America A*, 47:827–833, 1957. 26

M. Born and E. Wolf. *Principles of Optics*. Cambridge University Press, 6th edition, November 1997. 35, 39, 55

J.K. Bowmaker. The visual pigments, oil droplets and spectral sensitivity of the pigeon. *Vision Research*, 17(10):1129 – 1138, 1977. 25

T. Buehren and M.J. Collins. Near work induced wavefront aberrations in myopia. *Vision Research*, 45(10):1297–1312, 2005. 75

S. Burn and S. Marcos. *Measurement of the image quality of the eye with the spatially resolved refractometer*. Slack Publishing, 2001. 69

J Castejon-Mochon, N Lopez-Gil, et al. Ocular wave-front aberration statistics in a normal young population. *Vision Research*, 42(13):1611–1617, 2002. 74

W.N Charman. Aberrations and myopia. *Ophtalmic Physiological Optics*, (25):4, 285-231 2005a. 75

W.N Charman. Wavefront technology: Past, present and future. *Contact Lens and Anterior Eye*, 28(2):75–92, 2005b. 62

W.N Charman and J. Jennings. Longitudinal changes in peripheral refraction with age. *Ophtalmic Physiological Optics*, 26:447–455, 2005. 76

D.M. Chen, J.S. Collins, and T.H. Goldsmith. The ultraviolet receptor of bird retinas. *Science*, 225(4659):337–340, 1984. 27

S. S. Chin, K. M. Hampson, and E. A. H. Mallen. Binocular correlation of ocular aberration dynamics. *Opt. Express*, 16(19):14731–14745, Sep 2008. 75

N.J. Coletta, S. Marcos, et al. Double pass measurement of retinal image quality in the chicken eye. *Optometry and Vision Science*, 80(1):50–57, 2003. 3, 110

C.A. Curcio, K.R. Sloan, Kalina A., and E. Hendrickson. Human photoreceptor topography. *Journal of Comparative Neurology*, 292(4):497–523, 1990. 24

E.M. Daly and C. Dainty. Opthalmic wavefront measurements using a versatile pyramid sensor. *Applied Optics*, 49(3):67–77, 2010. 68

E.G. De la Cera, R. Rodriguez, et al. Longitudinal changes of optical aberration in normal and form-deprived myopic chick chickens. *Vision Research*, 46:579–589, 2006a. 110

E.G. De la Cera, R. Rodriguez, et al. Optical aberrations in the mouse eye. *Vision Research*, 46(16):2546–2553, 2006b. 3

W.J. Donnelly, K. Pseudovs, J.D. Marsack, E.J. Sarver, and R.A. Applegate. Quantifying scatter in shack-hartmann images to evaluate nuclear cataract. *Journal of Refractive Surgery*, 20:515–522, 2004. 72

A. Dubra, C. Paterson, and C. Dainty. Study of the tear topography dynamics using a lateral shearing interferometer. *Opt. Express*, 12:6278–6288, 2004. 9

J.T. Erichsen. *How birds look at things*. PhD thesis, Oxford University, 1979. xi, 3, 33, 34, 58, 112, 146

C. Fedtke, K. Ehrman, A. Ho, and B.A. Holden. Lateral pupil alignment tolerance in peripheral refractometry. *Optometry and Vision Science*, 88 (5):570–579, 2011. 117

E.J. Fernandez and P. Artal. Study of the effects of monochromatic aberrations in the accomodation response by using adaptive optics. *Optics Letters*, 26(10):746–748, 2001. 74

C.E. Ferre. Refraction for the peripheral field of vision. *Archives of Opthalmology*, 1931. 76

C.E. Ferre, G. Rand, and C. Hardy. Refractive asymmetry in the temporal and nasal halves of the visual field. *American Journal Opthalmology*, 15: 513–522, 1932. 76

H Fitzke, B.P. Hayes, et al. Refractive sectors in the visual field of he pigeon eye. *Journal of Physiology*, 369:33–34, 1985. 110, 112

L Frisen and A Glansholm. Optical and neural resolution in peripheral vision. *Investigative Ophthalmology*, 14(7):528–536, 1975. 44

Matthew F. Gaffney and William Hodos. The visual acuity and refractive state of the american kestrel (falco sparverius). *Vision Research*, 43(19): 2053 – 2059, 2003. 112

A. Glasser. Accommodation. In Darlene A. Dartt, editor, *Encyclopedia of the Eye*, pages 8 – 17. Academic Press, Oxford, 2010. 10

A. Glasser and H.C. Howland. A history of studies of visual accomodation in birds. *Q.Rev. Biol*, 72(2), 1997. 22

T.H. Goldsmith, J.S. Collins, and S. Licht. The cone oil droplets of avian retinas. *Vision Research*, 24(11):1661 – 1671, 1984. 27

J.W Goodman. *Introduction to Fourier Optics*. Ed.MAcGraw-Hill, 1968. 35, 55

S. Grupetta, F. Lacombe, and P. Puget. Study of the dynamic aberrations of the human tear film. *Journal of Optical Society of America A*, 13(19): 7631–7635, 2005. 9

A. Guirao and P. Artal. Off-axis monochromatic aberrations estimated from double pass measurements in the human eye. *Vision Research*, 39: 207–217, 1999. 76

A. Guirao and D. R. Williams. A method to predict refractive errors from wave aberration data. *Optometry and Vision Science*, 80(1):36–42, 2003. 60

O Gunturkun and U Hahmann. Visual acuity and hemispheric asymmetries in pigeons. *Behavioural Brain Research*, 60:171–175, 1994. 111

J. Gustafsson, E. Terenius, et al. Peripheral astigmatism in emmetropic eyes. *Ophtalmic Physiological Optics*, 21(5):393–400, 2001. 44, 76, 145

S. Hage el and F. Berny. Contribution of the crystalline lens to the spherical aberration of the eye. *Journal of Optical Society of America A*, 63(2): 205–211, 1973. 11

U. Hahmann and O Gunturkun. The visual acuity for the lateral visual field of the pigeon (columba livia). *Vision Research*, 33(12):1659 – 1664, 1993. 31, 112

M.I. Hall and C.F. Ross. Eye shape and activity pattern in birds. *Journal of Zoology*, 2006. 20

Karen M. Hampson and Edward A. H. Mallen. Multifractal nature of ocular aberration dynamics of the human eye. *Biomed. Opt. Express*, 2(3):464–470, Mar 2011. 75

W.M. Harmening, M.A. Vobig, P. Walter, and H. Wagner. Ocular aberrations in barn owl eyes. *Ocular aberrations in barn owl eyes*, 47(23):2934 – 2942, 2007. 3, 113

S. Hieda, O. Kinoshita. Measuring of ocular wavefront aberration in largue pupils using opd's scan. *Semin. Opthalmology*, 18:35–40, 2003. 66

W. Hodos and J.T. Erichsen. Lower field myopia in birds the adaptation that keeps the ground in focus. *Vision Research*, 30(5):653–657, 1990. 3, 33, 110, 112

W. Hodos, R.W. Leibowitz, and J.C. Bonbright. Near visual acuity of pigeons. effects of head location and stimulus luminance. *Journal of experimental and analytical Behaviour*, 25:129–141, 1976. 31, 110

W. Hodos, R.F. Miller, and K.V. Fite. Age-dependent changes in visual acuity and retinal morphology in pigeons. *Vision Research*, 31(4):669 – 677, 1991. 24

B.B. Howland and H.C. Howland. Subjective measurement of high-order aberrations of the eye. *Science*, 193:580–592, 1976. 64, 74

H.C. Howland. High order wave aberration of eyes. *Ophtalmic Physiological Optics*, 22:434–439, 2002. 74

H.C. Howland and Howland B. A subjective method for the measurement of monochromatic aberrations of the eye. *Journal of Optical Society of America A*, 67(11):1508–1518, 1977. 64, 74

A. Hughes. A useful table of reduced schematic eyes for vertebrates which includes computed longitudinal chromatic aberrations. *Vision Research*, 19(11):1273 – 1275, 1979. 111

S. Husband and T. Shimizu. *Evolution of the avian visual system. Avian visual cognition*. Online-Book, 2001. 22, 23

A.N. Iwaniuk, P. Hessy, M.I. Hall, and R.W. Douglas. Relative wulst volume is correlated with orbit orientation and binocular visual field in birds. *Journal of Comparative Physiology A*, 194:267–282, 2008. 27, 28

J. Jennings and W.N. Charman. Analytic approximation of the off-axis modulation transfer function of the eye. *Vision Research*, 37(6):697–704, 1997. 3

J. Jennings, A. M. Charman, et al. Off-axis image quality in the human eye. *Vision Research*, 21:445–455, 1980. 2, 76

T. Kern. *Exotic and laboratory animal Opthalmology, special issue of veterinary opthalmology*. Wiley, 2002. 23

M.L. Kisilak, M.C. Campbell, et al. Hartmann-shack measurement of the monochromatic image quality in the chick eye during emmetropization. *Investigative Ophthalmology and Vis.Sci*, 43, 2002. 110

J. Liang and D. Williams. Aberrations and retinal image quality of the normal human eye. *Journal of Optical Society of America A*, 14(11): 2873–2993, November 1997. 2, 72, 74

J. Liang, S. Goelz, and J.F. Bille. Objective measurements of wave aberrations of the human eye with the use of the hartmann shack wavefront sensor. *Journal of Optical Society of America A*, 11:1949–1957, 1994. 2, 71, 74

W. Lotmar and T. Lotmar. Peripheral astigmatism in the human eye: Experimental data and theoretical predictions. *Journal of Optical Society of America A*, 64(4):510–513, 1974. 2

L. Lundstrom. *Wavefront aberrations and Peripheral Vision*. PhD thesis, KTH University ,Stockholm Sweeden, 2007. 76, 142

L. Lundstrom, J. Gustafsson, et al. Assessment of objective and subjective eccentric refraction. *Optometry and Vision Science*, 82(4):298–306, 2005a. 76

L. Lundstrom, P. Unsbo, and J. Gustafsson. Off-axis wave front measurements for optical correction in eccentric viewing. *Journal of Biomedical Optics*, 10(3), May-June 2005b. 109, 117

L. Lundstrom, S. Manzanera, P. Prieto, et al. Effect on optical correction and remaining aberrations on peripheral resolution acuity in the human eye. *Optics Express*, 15(20):12654–12661, 2007. 76

L. Lundstrom, J. Gustafsson, and P. Unsbo. Population distribution of wavefront aberrations in the peripheral human eye. *Journal of Optical Society of America A*, 26(1):2192–2198, November 2009a. 76, 101, 109

L. Lundstrom, A. Mira-Agudelo, and P. Artal. Peripheral optical errors and their change with accomodation differ between emmetropic and myopic eyes. *Journal of Vision*, 9(6):1–11, 2009b. 77

L. Lundstrom, R Rosen, and P. Unsbo. Influence of optical defocus on peripheral vision. *Visual Psychophysics and Physiological Optics*, 52(1), 2011. 77

S Marcos, S.A. Burns, et al. A new approach to the study of ocular chromatic aberrations. *Vision Research*, 39(26):4309–4323, 1999. 51

J Marshall, J Mellero, et al. A schematic eye for the pigeon. *Vision Research*, 1973. 20, 21, 146

Graham R. Martin and Stephen R. Young. The retinal binocular field of the pigeon (columba livia: English racing homer). *Vision Research*, 23 (9):911 – 915, 1983. 31

A. Mathur, D. Atchison, and D.H. Scott. Ocular aberrations in the peripheral visual field. *Optics Letters*, 33(8):863–865, April 2008. 2, 76

A. Mathur, D. Atchison, and W.N. Charman. Effect of accommodation on peripheral ocular aberrations. *Journal of Vision*, 9(12):1–11, 2009. 77

A. Mathur, D. Atchison, and W.N Charman. Effects of age on peripheral ocular aberrations. *Optics Express*, 18(6):5840–5853, 2010. 76

S.A. McFadden. The binocular depth stereoacuity of the pigeon and its relation to the anatomical resolving power of the eye. *Vision Research*, 27(11):1967 – 1980, 1987. 31, 112

J.S. McLellan, S. Marcos, P. M. Prieto, and S. A. Burns. Imperfect optics may be the eye's defence against chromatic blur. *Nature*, 417(6885):174–176, 05 2002. 51

S.M. McRae, , R.R. Krueger, and R.A. Applegate. *Customized Corneal Ablation: The quest of supervision.* Slack Publishing, 2001. 63, 66

S.M. McRae, , R.R. Krueger, and R.A. Applegate. *Customized Corneal Ablation: The quest of supervision II.* Slack Publishing, 2004. 66

P. Mierdel, M. Kaemmerer, M Mrochen, H.E. Krinke, and T. Seiler. Ocular optical aberrometer for clinical use. *J. Biomed. Opt.*, 6(2):200–104, 2001. 65

M. Millodot and Lamont. A. Refraction of the periphery of the eye. *Journal of Optical Society of America A*, 64(1):110–111, 1974. 75

M. Millodot and J.G. Sivak. Contribution of the cornea and lens to the spherical aberration of the eye. *Vision Research*, 19(6):685 – 687, 1979. 12

H.O. Nalbach, F. Wolf-Oberhollenzer, and M. Kirschfeld. The pigeon's eye viewed through an ophthalmoscopic microscope: Orientation of retinal landmarks and significance of eye movements. *Vision Research*, 30(4): 529 – 540, 1990. 23

R. Navarro and M. A. Losada. Aberrations and relative efficiency of light pencils in the living human eye. *Optometry and Vision Science*, 74:540–547, 1997. 63

R. Navarro, P. Artal, and D. R. Williams. Modulation transfer of the human eye as a function of the retinal eccentricity. *Journal of Optical Society of America A*, 10(2):201–212, 1993. 76

R. Navarro, E. Moreno, and C. Dorronsoro. Monochromatic aberrations and point-spread- functions of the human eye across the visual field. *Journal of Optical Society of America A*, 15(9):2522–2529, 1998. 3, 76, 101, 145

R. Navarro, L. Gonzalez, et al. On the prediction of optical aberrations by personalized eye models. *Optometry and Vision Science*, 83(6):371–81, 2006. 8

R. Navarro, F. Palos, and L. Gonzalez. Adaptive model of the gradient index of the human lens. ii. optics of the accommodating aging lens. *Journal of Optical Society of America A*, 24(9):2911–2920, September 2007. 11

M. Nowakowski. *Study of Ocular Aberrations Within a 10 deg Central Visual Field.* PhD thesis, School of Physics, Science Faculty, National University of Ireland, Galway, March 2010. 94, 103, 127, 145

A. Nussbaum. Geometrical optics, aberrations. In B.D. Guenther, editor, *Encyclopedia of Modern Optics*, pages 11 – 19. Elsevier, Oxford, 2005. 35

Patrick W. Nye. The binocular acuity of the pigeon measured in terms of the modulation transfer function. *Vision Research*, 8(8):1041 – 1053, 1968. 30, 111

G. Osterberg. Topography of the layer of rods and cones in the human retina. *Acta Ophthalmologica*, 13(6):1–102, 1935. 14

L.A. Ostrin, Li. Yue, V. Choh, and C.F. Wildsoet. The role of the iris in chick accommodation. *Investigative Ophthalmology Visual Science*, 52 (7):4710–4716, 2011. 22

S. Plainis and I.G. Pallikaris. Ocular monochromatic aberration statistics in a large emmetropic population. *Journal of Modern Optics*, 55(4,5): 759–772, 2008. 74

Platt and Shack. History and principles of shack hartman wavefront sensing. *Journal of Refractive Surgery*, 17:5573–5577, 2001. 70

V. Porciatti, W. Hodos, G. Signorini, and F. Bramanti. Electroretinographic changes in aged pigeons. *Vision Research*, 31(4):661 – 668, 1991. 146

J Porter, A Guirao, et al. Monochromatic aberrations of the human eye in a large population. *Journal of Optical Society of America A*, 18(8): 1793–1802, 2001. 2, 74

P. Prieto and F. Vargas-Martin. Analysis of the performance of the hartmann-shack sensor in the human eye. *Journal of Optical Society of America A*, 17(8):1388, 1389 2000. 78

H. Radhakrishnan and W.N Charman. Age-related changes in ocular aberrations with accommodation. *Journal of Vision*, 7(7), 2007. 74, 75

R. Ragazzoni. Pupil plane wavefront sensing with an oscullating prism. *Journal of Modern Optics*, 43(2):289–293, 1996. 67

F. Rempt, H. Hoogerheide, and W.P.H. Hoogenboom. Peripheral retinoscopy and the skiagram. *Ophthalmologica*, 162:1–10, 1971. 33, 75

F. Roddier. Curvature sensing and compensation: a new concept in adaptive optics. *Applied Optics*, 27(1223-1225), 1988. 69

A. Roorda and A. Glasser. Wave aberrations of the isolated crystalline lens. *Journal of Vision*, 4:250–261, 2001. 11

E.A. Rossi, P Weiser, et al. Visual performance in emmetropia and low myopia after correction of high-order aberrations. *Journal of Vision*, 7 (8):14, 2007. 75

D.F. Russel. Eyes: Variety, development and evolution. *Brain Behaviour Evolution*, 64:141–147, 2004. 20

F. Schaeffel and H.C. Howland. Corneal accomodation in chick and pigeon. *J.Comp. Physiol A*, 160(3):374–384, 1987. 22

F. Schaeffel, G. Hagel, et al. Lower-field myopia and astigmatism in anphibians and chickens. *Journal of Optical Society of America A*, 11(2): 487–495, 1994. 3, 33, 110, 112

A. Seidelmann, F. Schaeffel, et al. Peripheral refractive errors in myopic, emmetropic,and hyperopic young subjects. *Journal of Optical Society of America A*, 19(12):2362–2373, 2002. 77

M.T. Sheenan, A.V. Goncharov, et al. Population study of the variation in monochromatic aberrations of the normal human eye over the central visual field. *Optics Express*, 15(12):7367–7380, 2007. 2, 76, 109

G. Smith, D. Atchison, et al. Designing lenses to correct peripheral refractive errors of the eye. *Journal of Optical Society of America A*, 19(1): 10–18, January 2002. 2

Sturkie. *Sensory physiology: vision, Avian Physiology.* Academic Press, 5th edition edition, 2000. 24

J Tabernero, A Benito, et al. Mechanism of compensation of aberrations in the human eye. *Journal of Optical Society of America A*, 24(10):3274–3283, 2007. 75

L.N Thibos, D.J. Walsh, and Cheney. Vision beyond the resolution limit: aliasing in the periphery. *Vision Research*, 27:2193–2197, 1987. 74

L.N Thibos, A Bradley, et al. Theory and measurement of ocular chromatic aberration. *Vision Research*, 30(1):33–49, 1990. 51

L.N Thibos, Still D.L., and A Bradley. Characterization of spacial aliasing and contrast sensitivity in peripheral vision. *Vision Research*, 36(2):249–258, 1996. 75

L.N Thibos, W. Wheeler, and Horner. D. Power vectors: an application of fourier analysis to the description and statistical analysis of refractive error. *Optometry and Vision Science*, 74:367–75, 1997. 117

L.N Thibos, R.A. Applegate, and R. Schweigrling, J.T. amd Webb. Standards for reporting the optical aberrations of eyes. *OSA trends in Optics and Photonics*, 35:232–244, 2000. 53

L.N Thibos, X. Hong, and A Bradley. Statistical variation of aberration structure and image quality in a normal population of healthy eyes. *Journal of Optical Society of America A*, 19(12):2329–2348, 2002. 74

L.N Thibos, X. Hong, A Bradley, and R.A. Applegate. Accuracy and precision of objective refraction from wavefront aberrations. *Journal of Vision*, 4(9):329–351, 2004. 60

A. Tomlinson, R.P. Hemenger, and R. Garriot. Method for estimating the spheric aberrationof the human crystalline lens in vivo. *Investigative Ophthalmology and Vis.Sci*, 34(3):612–629, 1993. 11

Daniel J. Uhlrich, Patricia M. Blough, and Donald S. Blough. The pigeon's distant visual acuity as a function of viewing angle. *Vision Research*, 22 (4):429 – 431, 1982. 31

E. Villegas, R.L. Carretero, et al. Le grand eye for the study of ocular chromatic aberration. *Ophtalmic Physiological Optics*, 16(6):528–531, 1996. 51

Walls. *The Vertebrate Eye and its Adaptive Radiation.* Hafner, 1942. 25

G. Walsh, A M Charman, and H.C. Howland. Objective technique for the determination of monochromatic aberrations of the human eye. *Journal of Optical Society of America A*, 1(9):987–992, 1984. 74

L Wang and D. Koch. Ocular higher-order aberrations in individuals screened for refractive surgery. *Journal of Cataract and Refractive Surgery*, 29:1896–1903, 2003. 2

L. Wang and R.M. Santaella. Higher-order aberrations from the internal optics of the eye. *Journal of Cataract and refractive Surgery*, Opthalmic and Physiological Optics(16):6, 528-531 2005. 11

YZ. Wang, L.N Thibos, N. Lopez-Gil, and T.O. Salmon. Subjective refraction of the peripheral field using contrast detection acuity. *Journal of the America Optometry Association*, 67(10):584–589, 1996. 75

R. H. Webb, C.M. Penney, and K.P. Thompson. Measurement of ocular local wavefront distortion with a spacial resolved refractometer. *Applied Optics*, 31:3678–3868, 1992. 68

B. William. *Borish's Clinical Refraction.* Butterworth Heinemann, 2006. 58

D. Williams. *Opthalmology (Avian Medicine: Principles and Application).* Wingers, Publishing, 1994. 22

D. R. Williams, P. Artal, et al. Off-axis optical quality and retinal sampling in the human eye. *Vision Research*, 36(8):1103–1114, 1996. 76

H. Wolburg, S. Liebner, A. Reichenbach, and H. Gerhardt. The pecten oculi of the chicken: A model system for vascular differentiation and barrier maturation. In Kwang W. Jeon, editor, *A Survey of Cell Biology*, volume 187 of *International Review of Cytology*, pages 111 – 134, 134a, 134b, 134c, 135–159. Academic Press, 1999. 25

J.F. Wortel, R.J. Wubbels, and J.F.W. Nuboer. Photopic spectral sensitivities of the red and the yellow field of the pigeon retina. *Vision Research*, 24(9):1107 – 1113, 1984. 25

Y.Z Zang, L.N Thibos, and A Bradley. Effects on refractive error on detection acuity in peripheral vision. *Investigative Ophthalmology and Vis.Sci*, 38(10):2134–2143, 1997. 74